Università degli Studi di Padova

Centro di Ateneo di Studi e Attività Spaziali
“Giuseppe Colombo” — CISAS

PhD Course in “Scienze Tecnologie e Misure Spaziali”
Curriculum in Scienze e Tecnologie per Applicazioni
Satellitari e Aeronautiche - STASA — Series XXXVI

In-flight calibration and performance verification for space instruments

Coordinator
Prof. Francesco Picano

Supervisor
Dr. Paola Zuppella

Co-supervisor
Dr. Vania Da Deppo

PhD Candidate
Chiara Casini

To the one who makes my world brighter and fills my life.

Your love and support lift me ”On Top Of The World” and your presence shines as bright as ”Thunder” in my life, making me a true ”Believer”.

You are the ”light in my shadow”.

Abstract

In-flight calibrations play a crucial role in ensuring the reliability of scientific data obtained by space optical instruments, such as telescopes or cameras. One effective method for assessing the optical performance of these instruments consists of analyzing the images acquired during the commissioning phase: flat-field, dark, and star images, by comparing them to on-ground measurements.

Throughout this PhD work, the activity has focused on devising methods and realizing appropriate codes to study the performance and calibration of space instruments.

This work presents a comprehensive overview of the concept, input requirements, and simulations conducted to: predict the stars visible in the field of view (FoV) of specific space instruments, and the behavior of sources in front of their apertures. In particular, this work applies to two specific space instruments: the Metis coronagraph on board Solar Orbiter and the STC stereo camera on board the BepiColombo mission.

For both instruments, I simulated stars within their respective FoV, compared the analysis with in-flight star images, and extracted information related to the Point Spread Function (PSF). Real images of the stars are also compared with those simulated with point sources. This permitted to validate the effectiveness of our calibration methodologies, and to gain valuable insights into the instrument's expected performance.

For Metis, the behavior of sunlight reflected by the aperture door is studied, confirming that the signal intensity follows the $1/r^2$ law for door illumination and is proportional to exposure time, but infirming the idea that the door's retro-reflection could not serve as a suitable homogeneous illumination source. The passage of a star through Metis' field of view is also studied and has a dual purpose: assessing the evolution of the vignetting function during the mission, and evaluating its potential for detecting optical element degradation. The results demonstrated good agreement between on-ground, in-flight, and simulated vignetting functions, as expected for a recent mission.

For STC, emphasis was put on the analysis of dark images acquired during the commissioning phase. The detection of bad pixels for different integration times was made, leading to the discovery of patterns in the Pan L and Pan H filters. Their evolution was studied in detail, and further research to understand their origin is proposed.

For both instruments, these analysis enabled us to set the basis for the monitoring of variations in instrument performance and sensitivity, primarily attributed to degradation or misalignment of optical components. Indeed, the instruments under consideration operate in a challenging environment, they are working close to the Sun and in orbit around Mercury, which subjects them to experience high temperatures and significant temperature variations.

Contents

List of Figures

List of Tables

List of Acronyms

ADC	Analog to Digital Converter
ADU	Analog to Digital Unit
APS	Active Pixel Sensor
AOI	Angle Of Incidence
ASW	Application SoftWare
BSW	Boot SoftWare
CAD	Computer-Aided Design
CM	Color Mapping
CME	Coronal Mass Ejections
CMOS	Complementary metal-oxide semiconductor
CNR	Consiglio Nazionale delle Ricerche (National Research Council)
CPC	Camera Power Converter
CPCU	Command and Process Control Unit
CR	Cosmic Ray
CU	Compression Unit
DC	Dark Current
DEC	Declination
DIT	Detector Integration Time
DPU	Data Processing Units
DTM	Digital Terrain Model
EE	Ensquared Energy

ESA	European Space Agency
FITS	Flexible Image Transport System
FoV	Field of View
FPA	Focal Plane Assembly
FPN	Fixed Pattern Noise
FPGA	Field Programmable Gate Array
FSA	Filter Strip Assembly
FS	Field Stop
FWHM	Full Width at Half Maximum
HRIC	High spatial Resolution Imaging Channel
HVU	High Voltage Unit
HW	Hardware
IC	In-flight Calibration
IAPS	Intensified Active Pixel Sensor
ICO	Instrument Check Out
IEO	Inverted External Occulter
IF	Interference Filter
IFA	Interference Filter Assembly
IO	Internal Occulter
IOM	Internal Occulter Mechanism
INAF	Istituto Nazionale di AstroFisica (National Institute for Astrophysics)
IT	Integration Time
LCVR	Liquid Crystal Variable Retarder
LOS	Line Of Sight

LS	Lyot Stop
LT	Long Term
LTP	Long Term Planning
M0	Sun-disk rejection mirror of the coronagraph
M1	Primary mirror of the coronagraph
M2	Secondary mirror of the coronagraph
MCP	Micro Channel Plate
ME	Main Electronics
MMU	Mass Memory Unit
MOU	Metis Optical Unit
MPPU	Metis Processing and Power Unit
MPS	Max Planck Institute for Solar System Research
NASA	National Aeronautics and Space Administration
OBT	Observation Time Span
PB	Polaried Brightness
PCU	Photon Counting Unit
PE	Pedestal Effect
PI	Principal Investigator
PMP	Polarization Modulation Package
PO	Peak Offset
PSF	Point Spread Function
PU	Power Unit
PSP	Parker Solar Probe
QE	Quantum Efficiency

QTH	Quartz Tungsten Halogen
RA	Right Ascension
RMS	Root Mean Squared
RT	Repetition Time
S/C	Spacecraft
SEP	Solar Energetic Particles
SIMBIO-SYS	Spectrometers and Imagers for MPO BepiColombo Integrated Observatory SYStem
SM	Stereo Mapping
SNR	Signal to Noise Ratio
SO	Solar Orbiter
SOHO	Solar and Heliospheric Observatory
SPICE	Spacecraft Planet Instrument Camera pointing and Events
SPOCC	SPace Optics Calibration Chamber
STC	STereo Camera
STP	Short Term Planning
TB	Total Brightness
TC	Telemetry
TM	Telecommand
UTC	Universal Coordinated Time
UV	Ultra Violet
UVDA	Ultraviolet Detector Assembly
VIHI	VIsible and Hyper-spectral Imaging channel
VL	Visible Light
VLDA	Visible-light Detector Assembly

1

Introduction

Space missions opened new frontiers in the observation and in the study of astronomical objects like planets, comets, asteroids, and so on. In particular, missions dedicated to the study of the Sun and its effects on the solar system provided important information on our closest star, its surrounding environment and interactions with our planet Earth.

In the last decades, several space missions have been launched to explore the Sun and the planets of the Solar System, also the closest one: Mercury. Such missions have employed, each time, more sophisticated instruments, among which coronagraphs and stereo cameras, to acquire high-quality data. To convert such high-quality data into accurate measurements and detailed images, it is fundamental to perform appropriate and rigorous in-flight calibrations. These calibrations allow the compensation of the variation of the instrument response, the correction of the defects and the increase of the measurement accuracy.

The work of this PhD thesis will focus on the importance of the in-flight calibration applied to two instruments: a coronagraph, Metis, on board Solar Orbiter (SO); and a stereo camera, STC, one of the three channels of the SIMBIO-SYS suite on board Bepicolombo, aimed to study, respectively, the solar corona and the Mercury surface. It is important to highlight the critical parameters and the techniques used to guarantee the quality and reliability of the acquired data.

One of the objectives of this thesis is to give a panoramic overview of the calibration to be done for space instrumentation and the key parameters to be taken into account, and then apply these to Metis and STC.

The aim is to underline the benefits of the in-flight calibration and to highlight the advantage with respect to the on-ground calibration for a coronagraph and a stereo camera. Such calibrations are crucial to ensure quality data in space missions.

Indeed, it is essential for a space mission to address simultaneously the following key-points:

- identify the parameters that have to be calibrated to obtain accurate measurements and images;
- know the radiometric response of the instrument and verify it during the entire lifetime of the space mission;
- mapping the bad pixels and address the correction to avoid the problem of images with artifacts;
- characterize the Point Spread Function (PSF) i.e. the response of an imaging system to a point source or point object.

It is also important to evaluate the impact of the in-flight calibration on the scientific data and their interpretation for all the missions. This is why I review in the following sections the methodologies and techniques used to perform in-flight calibrations, including calibration experiments and data processing procedures. This can be summarized in the following question: what techniques are used to obtain accurate measurements?

This question is particularly acute in the context of the BepiColombo and Solar Orbiter missions, since it is the first time that a coronagraph and a stereo camera reach a position so close to the Sun and Mercury.

Answering this question regarding the in-flight calibration allows, also, standardizing the data to match the previous data obtained with other instruments or space missions, creating a continuity between space observations. This facilitates the study of long-term solar and planetary phenomena and allows a more complete and coherent view of the evolution of the Sun and Mercury over time.

Therefore, to explain the evolution of space observation/instrumentation, a brief presentation of the Sun and Mercury and a focus on the space missions aiming at the Sun and Mercury will follow.

1.1 The Sun, the history and the scientific objectives

This section starts with a brief introduction on the Sun, followed by the evolution of the space missions aiming at studying the corona.

1.1.1 the Sun

The Sun is the star at the center of the Solar System. It is a G-type main-sequence star, which formed approximately 4.6 billion years ago. The Sun can be divided into two parts: the internal part and the atmosphere. The internal part is composed by: the core; the radiative zone; the convective zone; and the photosphere as shown in figure 1.1. On the basis of the temperature, the solar atmosphere is divided in the following regions: the chromosphere (4000 K - 8000 K) the inner layer, the transition region (8000 K - 500000 K) and the corona (over 1 million of Kelvin), which is the outer layer.

The visible radiation coming from the corona is 7 orders of magnitude weaker than the one from the photosphere, for this reason an ad-hoc telescope, the coronagraph, has been conceived to study the outer layer of the solar atmosphere. The Sun is not static; there are features on the surface like sunspots and granulation, then there are prominences: structures with a loop shape that stretch outward from the photosphere and extend outwards into the solar corona as shown in figure 1.1. If a prominence is eruptive it becomes a Coronal Mass Ejection (CME): a significant ejection of magnetic field and accompanying plasma mass from the Sun's corona into the heliosphere. Another dynamical phenomenon is the solar flare: an intense localized eruption of electromagnetic radiation in the Sun's atmosphere. CMEs can also be created from flares. In both cases, this explosion can have a direct impact on Earth. If the CME is directed towards Earth, when it collides with our magnetosphere, it creates an amazing aurora or induces satellite and communication disturbance, destruction of the satellites and so on. Knowing these phenomena better can help to predict the CMEs and limit the damage.

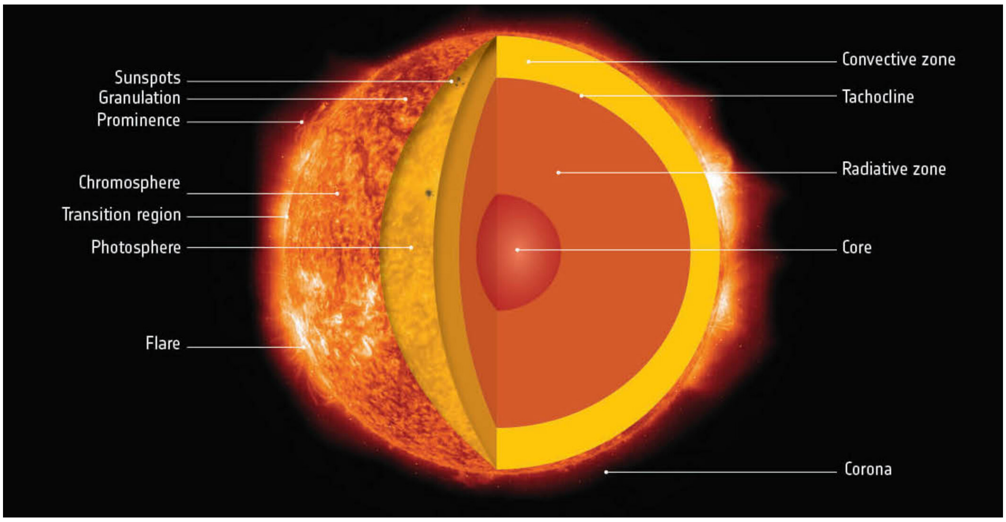

Figure 1.1: Layers inside of the Sun: the core, the radiative zone, the convective zone, the photosphere. The atmosphere of the Sun: chromosphere, transition region and the corona. It presents some phenomena that appear on the Sun: Sunspots, Granulation, Prominence and Flare [1].

Despite many space missions have been launched to study the corona and its phenomena, there is still much study to be done, a lot of questions are without an answer, for example the solar wind, which is a stream of charged particles released from the corona: where does it originate from, and where do the heliospheric structures come form? To answer such questions, Solar Orbiter has been built.

In the next subsection, a brief history of the space missions dedicated to the Sun exploration is presented.

1.1.2 Space mission for studying the Sun

The first studies of the solar corona, in white light, were performed during total solar eclipses. These were time-limited as total solar eclipses are short in duration (7 minutes at most). On average, an eclipse occurs every 18 months, but most are only visible from the oceans and are therefore not easily documented. Scientifically exploitable eclipses occur every two to three years.
In 1930 the French astronomer Bernard Lyot, positioning on the focal plane of the primary objective of a telescope an opaque disc, called the occulter, created the first coronagraph, an instrument capable of simulating solar eclipses [2]. The occulter blocks the photospheric radiation of the Sun, like the Moon during eclipses, so the solar corona can be observed continuously and, from space, in all wavelengths. Lyot's instrument undoubtedly represents a breakthrough in coronal physics, but unfortunately Earth-based observations are limited by the Sunlight scattered by the atmosphere, observations from space allow us to avoid that issue.
There are two categories of coronagraphs, distinguished according to the position of the occulter: the internally occultated ones, i.e the occulter is placed downstream of the primary objective, and the externaly occultated, i.e the occulter is directly invested by the light of the disk solar.
The first space observation in the ultraviolet was carried out on 10-10-1946 by means of a sounding rocket launched by the USA. The rocket reached an altitude of 175 km (outside the Earth atmosphere). These launches had a limit: they allowed observations lasting no more than a few minutes.
The first space coronagraph was mounted on an aerostatic balloon created in the early 1960s by Newkirk and Eddy, it was an externally occulted coronagraph, it reached a height of about 25 km [3]. Unfortunately, the instrument was not optimized for the reduction of the scattered light from the edges of the optical elements, and therefore the observation failed. Only in 1963 the first image of the extended corona was acquired without a natural eclipse. To do that, a small externally occulted coronagraph was mounted on board a rocket.
The first coronagraph capable of monitoring the corona for a long period flew aboard the **OSO-7** satellite (Orbiting Solar Observatory): it orbited Earth from

October 1971 to June 1974, resulting in the first observation of a *CME*.

On board the first **Skylab** space station, launched on 14/05/1973 and crashed on 11/07/1979, there was an externally occulted coronagraph. The various crews took about 35,000 film photos of the corona, acquiring a lot of activity of the Sun, including 8 solar flares and confirming the existence of coronal holes[1].

The **Solar Maximum Mission** probe, SMM or SolarMax, was launched on 14/02/1980 and crashed on 02/12/1989. The major goal was to discover that during the maximum of the solar cycle the number of sunspots reaches its maximum. The optical design of the coronagraph was based on Skylab, with some improvements, including the use of a Vidicon[2] instead of the photographic plate [4]. Thanks to a mission on 1984, necessary to repair the instrument, the SMM remained active until 1989, collecting a large amount of data.

In 1993, the coronagraph on board the spacecraft **Spartan-201** was the first to use a charged coupled device (CCD) detector. The duration of the mission was only 40 hours, but sufficient to acquire coronal images in white light thanks to the implementation of an external occulter. The Spartan missions were launched 4 times: in April 1993 (Spartan 201-1), in September 1994 (Spartan 201-2), in September 1995 (Spartan 201-3), and in November 1997 (Spartan 201-4). Each time the *Shuttle* (*Discovery, Endeavour, Columbia*) travelled, it released the Spartan payloads into space, and, after the observations were carried out, brought them back to Earth.

The space observatory **SOHO** was launched in 1995 and is still partially operational [5, 6]. It is stationary in gravitational equilibrium at the Lagrangian point L1, allowing uninterrupted observation of the Sun, and is very important to understand the Sun.

The set of coronagraphs that make up SOHO's LASCO have made it possible to continuously observe the corona and record its activity without interruption since 1996.

The major achievement obtained with the LASCO suite is a better understanding of the propagation and the evolution of coronal ejection. The high sensitivity of the instruments and the continuity of observation have made it possible to systematically record also the weak solar eruptions. Indeed, such weak solar eruptions emit more in the ultraviolet than in the visible spectral range. This justifies the integration of UV-detector and spectrometers in general on board of space missions, so as to retrieve such complementary information.

On board SOHO there is also the UVCS coronagraph spectrometer. It allows to perform ultraviolet spectroscopy measurements in the two channels Ly α and OVI,

---

[1] A coronal hole is a temporary region where the plasma is less dense respect to that in the solar corona

[2] The Vidicon tube is a type of vacuum tube and is used for the production of digital images.

between 114.5 and 128.7 nm and between 98.4 and 108 nm, respectively.
With the SOHO mission, it was possible to do observations which allowed the development of helioseismology. This matter uses measurements of the speed where each point on the surface of the Sun approaches or moves away from the Earth. Both solar oscillations and helioquakes (earthquakes on the Sun) have been observed.
At the beginning of this century, a huge step forward in the technology used for the space missions has been accomplished with the SECCHI coronagraphs of the Solar TErrestrial RElations Observatory, **STEREO**, a mission launched on 26/10/2006, and still ongoing. STEREO consisted of two twin probes: STEREO-A (Ahead) and STEREO-B (Behind); at present only STEREO-A is still in operation. The two spacecraft were moving along two different orbits around the Sun, thus being able to observe the corona from different perspectives, allowing the reconstruction in polarized visible light of the three-dimensional structure of the corona and its eruptions.
In 2009, a sounding rocket carrying the **HERSCHEL** (HElium Resonant Scattering in the Corona and HELiosphere) mission was successfully launched. The scientific payload included a coronagraph dedicated to the observation of the corona in the HeII 30.4 nm line (HeCor), and a prototype of the Solar Orbiter/Metis coronagraph, SCORE (Sounding COROnagraph Experiment), capable of making multiband images of the external corona in the following wavelength bands: visible, HI Lyα 121.6 nm and HeII 30.4 nm. The mission delivered the first global map of the solar corona in the HeII band [7].
Parker Solar Probe was launched in August 2018. Its primary goals are to track the flow of energy, to understand coronal heating, and to explore what accelerates the solar wind. The observations of this spacecraft are coordinated with those of Solar Orbiter (described later on) in order to have a global understanding of our star. Parker Solar Probe is on the ecliptic plane with an eccentric orbit that will make it pass through the corona, less than 6 million km from the solar surface (about one-tenth of the distance between the Sun and Mercury).

Each of these missions had a specific goal and improved the understanding we have of our closest star. However, none of them has been able to fully explore the region where the solar wind originates and where heliospheric structures form. This is the reason-to-be and the goal of the Solar Orbiter mission, one of the two missions at the core of my PhD work. The other mission being BepiColombo, aimed to the study of Mercury.

In the next section, Mercury is briefly introduced alongside the history of its related space missions.

1.2 History and scientific objectives of Mercury exploration

In the following sub-sections Mercury and then a brief history of the related space missions are described.

1.2.1 Mercury

Mercury is the planet closest to the Sun and the smallest planet of the solar system with a diameter of 4878 km, of which 40% is occupied by the iron core. Mercury is rich in magnesium and is poor in calcium, aluminum and iron. Mercury's axis of rotation is tilted just 2° with respect to the plane of its orbit around the Sun; the orbit is highly elliptical: the distance between Mercury and the Sun ranges from 0.3 AU to 0.47 AU. It is the only planet having a resonance with the Sun of 3:2: it has two revolutions around the Sun every three rotations around its spin axis (59 days for one rotation and 88 for one revolution). The scientist Giuseppe Colombo studied the rotation period of Mercury assessing the planet was already in a stable 3:2 resonance condition and it was not going to decrease its rotation speed to reach a 1:1 resonance as previously thought. This resonance has implications for the planet's environmental conditions and temperature.
The temperature on the surface of Mercury ranges from 75K to 700K at the equator: the difference in temperature between dark and bright surfaces is 600 K.
The major structures visible on Mercury surface are [8]:

- *Intercrater Plains*: gently rolling terrains between two large craters with a high abundance of craters with a diameter in the range from 5 to 10 km. They are the results of resurfacing: the surface of Mercury was covered by magma due to volcanic activity.
- *Smooth Plains*: sparsely cratered deposits. In these areas there is evidence of contractional deformation.
- *Basin*: region with impact basin as shown in figure 1.3.

The radar observation of the polar areas noted bright features in which the presence of water was possible, due to the inclination of the orbital axis, so that there are areas always in shadow. The water may have been brought in by cometary impacts and kept in cold traps.
As for the composition, most of the information came not from orbital measurements but from spectral analyses performed from Earth at various times.

In the next subsection, an overview of the space missions around Mercury is presented.

1.2.2 Space missions around Mercury

Reaching Mercury is difficult due to its harsh environmental conditions and the need for the spacecraft to decelerate. This explains why only two missions, Mariner 10 and MESSENGER, have been undertaken to reach Mercury.
Mariner 10 mission was launched by NASA in November 1973. It is the first mission to explore two planets, Mercury and Venus, during a single mission.
Thanks to the orbital mechanics calculations of Giuseppe Colombo, the spacecraft repeatedly used a gravity assist to change its flight path. The spacecraft made three flybys of Mercury in March and September 1974 and in March 1975.
Mariner 10 was the first spacecraft to return to its target after an initial flyby; the first one to use the solar wind as a major means of spacecraft orientation during flight; the first one to use solar pressure on its solar panels and high-gain antenna for attitude control.
From the first images of the surface, Mercury presents a Moon-like surface with craters, ridges and chaotic terrain, and from the magnetometers a weak magnetic field was revealed. During the closest encounter, Mariner 10 crossed behind the nightside of the planet, indicating a very tenuous atmosphere or ionosphere.
The temperature information was retrieved by the radiometer: the minimum during the night was 90 K and the maximum daytime was 460 K.
During its three Mercury flybys, Mariner 10 returned more than 2700 pictures that covered nearly 45% of Mercury's surface and provided the first detailed images of the planet (as shown in figure 1.2). The most impressive surface feature was the Caloris basin, is one of the largest impact basin in the solar system, and the largest feature on Mercury (1300 kilometers in diameter). Only half of the basin was imaged by Mariner 10, and the picture was completed by the MESSENGER mission (which will be introduced soon).
The resolution of the image was between 1 and 4 km/pixel, it depends on the orbit. The information retrieved from the data was that the cratered terrains were not cratered like on the Moon, the crater density is lower than on the Moon but higher than on Mars.
Other information provided by Mariner 10 was that the entire surface of Mercury was affected by asymmetric scarps which are interpreted as reverse faults, of compressive origin. Since they were distributed over the entire surface of Mercury, their origin was quite constrained, i.e. the planet was shrinking.
Mariner 10 was therefore of major importance for our current understanding of the surface of Mercury. The internal structure, the elements and the mineralogy composition were then studied by the MESSENGER mission.
The **MESSENGER** (Mercury Surface, Space ENvironment, GEochemistry, and Ranging) mission was a NASA mission launched on August 2004; the spacecraft took more than seven years to reach Mercury, performing several gravity-assisted

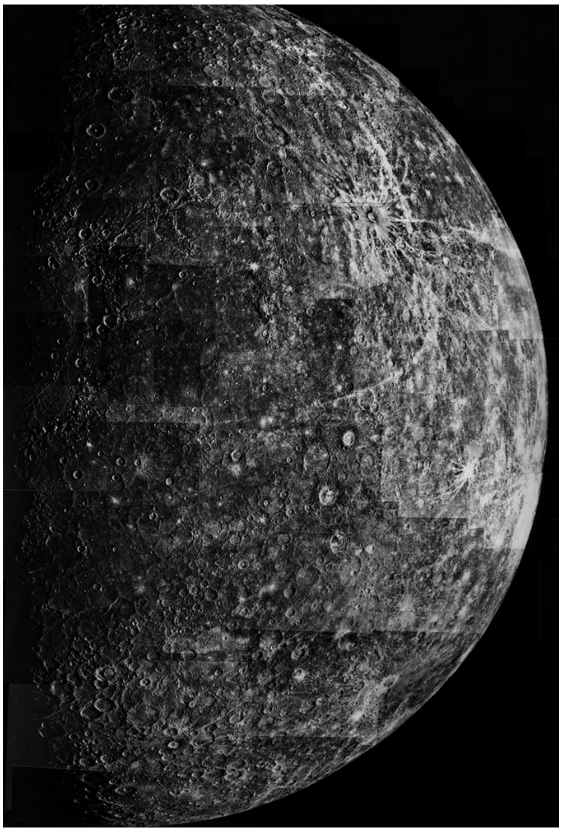

Figure 1.2: Mosaic of Mercury surface made by Mariner 10. The mosaic was made up of 18 pictures, taken about 6 hours after closest approach [9].

flybys of Venus, and three close flybys of Mercury.
MESSENGER entered in orbit around Mercury in March 2011, and made detailed observations of the planet for over four years as shown in figure 1.3.

The mission has contributed to a better understanding of Mercury's geological history, its composition, its magnetosphere and many other aspects. It measured the concentrations of magnesium and calcium on Mercury's night side, found large amounts of water in the exosphere (last layer of the atmosphere); water ice on the poles. Particularly dark deposits have been noticed in the areas of the craters, which could be organic material that accompany water ices of cometary origin. MESSENGER also revealed evidence of past volcanic activity on the surface.
The mission acquired more than 200000 images, enabling almost the entire surface of the planet to be mapped both in high-resolution monochrome and in color, as shown in figure 1.3 [10].
On April 30^{th} 2015 MESSENGER slammed into the surface of Mercury, creating a new crater on Mercury. The simulation of the impact on the planet is presented

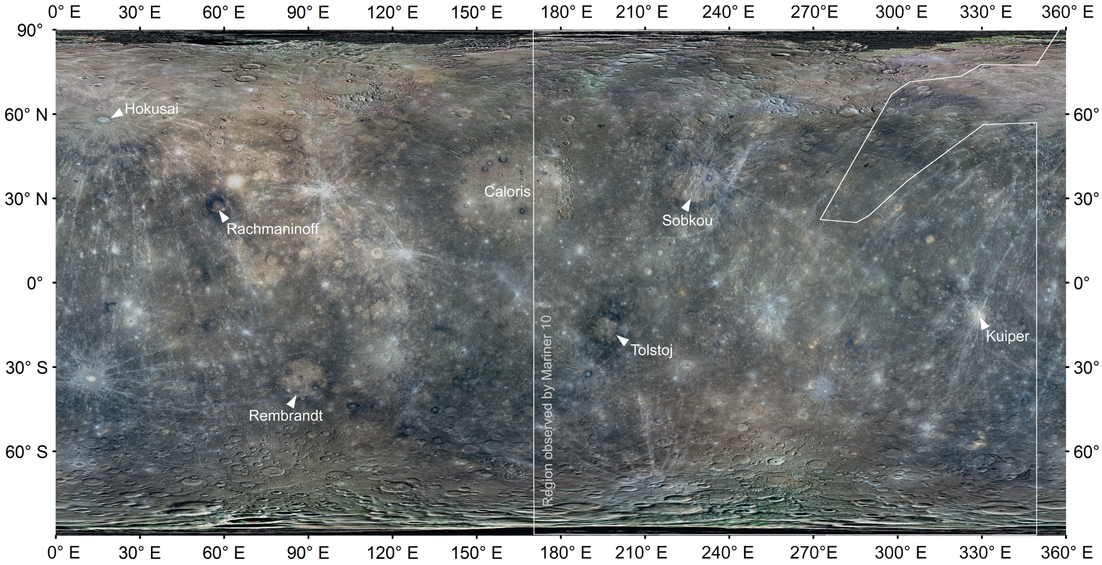

Figure 1.3: Global map of Mercury made by MESSENGER. In the outlined in white the region viewed by Mariner 10 [8], in the center the Caloris Basin, the name near the arrows are the impact craters/smaller basin.

in the article of E.Martellato [11].
On board of Messenger there were the two framing cameras, the Mercury Dual Imaging System (MDIS), composed of a wide-angle refractive optic imager with a FoV of 10.5° and a reflective optic imager with a field of view of 1.5°. The primary objectives of the mission were to perform high resolution targeted coverage, and global stereo imaging for high resolution topography. MDIS acquired more than 270000 images, for calibration and to create a monochrome global map, the Digital Terrain Model (DTM), multispectral global and regional maps, and a regional target mosaic [12, 13].

1.3 Solar Orbiter and BepiColombo missions

The space missions **Solar Orbiter** and **Bepicolombo** are projects of the European Space Agency, **ESA**[3]. They belong to the program ”ESA Cosmic Vision”, created in 2005 and concerning long-term plans for space science missions.
The program was created to answer big questions about the Solar System and the universe. The questions to answer are: How does the Solar System work? What are the conditions for planet formation and the emergence of life? [14] In this con-

---

[3] the European Space Agency, founded in 1975, is the international agency in charge of coordinating European space projects.

text, Solar Orbiter, launched in February 2020, is providing unprecedented views of the Sun and its phenomena, whereas BepiColombo, launched in October 2018, aims to understand the innermost planet of the Solar System. Both missions are presented in the following sections.

1.3.1 Solar Orbiter

Solar Orbiter was created thanks to the collaboration of ESA and NASA[4] and is the first mission of ESA's Cosmic Vision 2015-2025 program [14].

In paragraph 1.1.2 the great success of the SOHO solar mission is described. Following its results, it has been decided that the exploration of the Sun required, as a further step, a spacecraft to study continuously the Sun, covering all latitudes (including the solar poles), from the innermost areas under the surface up to the corona. Solar Orbiter is the first S/C to do that, it is approaching the Sun and will reach 0.28 AU; in February 2025 it will go out of the ecliptic plane.

The scientific goal of the Solar Orbiter mission, as presented above, relies on the following question: how does the solar system work? More precisely, the spacecraft is acquiring data to address this central question: how does the Sun create and control the heliosphere? Answering this fundamental question implies addressing the four interconnected scientific questions, all highly relevant to the topic of cosmic vision [15].

1. How and where does the plasma and magnetic field of the solar wind originate in the corona?
2. How do transient solar phenomena drive heliospheric variability?
3. How do solar flares produce energetic particle radiation found in the heliosphere?
4. How does the solar dynamo work and how does it relate the Sun to the heliosphere?

To answer the first question, the Solar Orbiter will pass both North and South of the solar equatorial plane in each orbit, making it possible to follow the evolution of the solar wind and the interplanetary magnetic field and both the photosphere and the corona (in remote sensing) [15]. It will allow for a correlation between the solar wind properties (velocity, mass flow, composition, charge states and wave

---

[4] The National Aeronautics and Space Administration is the US government agency responsible for aerospace programs and research, established on July 20^{th}, 1958 and operational on October 1^{st} of the same year.

amplitudes), measured in-situ, and those measured in corona.

To answer the second question, ”How do transient solar phenomena drive heliospheric variability?”, Solar Orbiter will provide the necessary data to determine how coronal magnetic energy is converted into kinetic energy by *CMEs* through the combined observations with the magnetometer, the imaging spectrograph and the soft X-ray imager. It will perform in-situ measurements of the fields and plasmas (in particular the composition) of the CMEs during the early stages of their propagation through the heliosphere.

For the third question: ”How do solar flares produce energetic particle radiation found in the heliosphere?” Solar Orbiter will improve information on the origins of Solar Energetic Particles (SEP) through images of loop and CMEs: in the visible, in the UV and in the X-rays. The combination of this information with that of the local electron density and the coronal ion velocity provided critical constraints on the shock evolution models in regions too close to the Sun.

To answer the last question, ”How does the solar dynamo work and how does it relate the Sun and the heliosphere?”, one has to distinguish a global and a local dynamo, and to do that one needs to study the distribution of small elements of emerging magnetic flux at all heliographic latitude. Observations made above the ecliptic will be able to measure weak magnetic features at both low and high latitudes. If the number and size (i.e. magnetic flux) of such features are significantly different at high latitudes, then the weak features are likely due to the global dynamo. If, however, they are evenly distributed, the evidence of a significant role for a local dynamo will be greatly strengthened [16].

Adressing all these problematics leads to a specific instrumental conception that is presented hereafter.

As far as the Solar Orbiter spacecraft is concerned, it is, for most of the time pointing at the Sun center, is three-axis stabilized and has a heat shield. The single-sided solar arrays provide the required power throughout the mission over a wide range of distances from the Sun, and can be rotated about their longitudinal axis to manage their temperature, especially as they approach the Sun. A high-gain antenna provides nominal communication with the ground station, while a medium-gain antenna and two low-gain antennas are used as backup [15]. The table 1.1 sums up the Solar Orbiter features.

One of the strengths of the Solar Orbiter mission is the synergy between the 4 in-situ and the 6 remote-sensing instruments observations. The position of the instruments is presented in figure 1.4; each scientific objective requires coordinated observations between several in-situ and remote-sensing instruments. Another unique aspect of Solar Orbiter is that the S/C will perform observations with the remote-sensing instruments, which are organized into three 10-day intervals centered around perihelion and maximum latitude or maximum co-rotation passages.

Dimensions	2.5m x 3.0m x 2.5 m
Pointing stability	3 arcsec/15min
Total mass	1800 kg
Maximum power	∼ 1100 W
Payload mass	∼190 kg
Payload power consumption	∼ 180-250 W
S/C orientation	pointing the Sun
Telemetry band	Dual X-band
Download data time	150 kbit/s (at 1 UA)
Perihelium	0.28 UA
Maximum heliographic latitude	25°(nominal mission) 34°-36° (extended mission)
Nominal mission duration	7 years (include the cruise phase)
Extended mission duration	3 years
Post-operation & storage	2 years
Earth station	Malargue (Argentina), antenna of 35 m operative from 4 to 8 hours/day

Table 1.1: Solar Orbiter parameters

The in-situ tools will run continuously during normal operations [15]. The in-situ equipments are the:

- *Energetic Particle Detector* (EPD): measures the properties of superthermal ions and energetic particles in the energy range of a few KeV for relativistic electrons and high energy ions (100 MeV protons, 200 MeV heavy ions).
- *Magnetometer* (MAG): provides detailed measurements of the heliospheric magnetic field.
- *Radio and Plasma Wave analyser* (RPW): measures both magnetic and electric fields at high time resolution, and determines the characteristics of electromagnetic and electrostatic waves in the solar wind up to 20 MHz.
- *Solar Wind Analyzer* (SWA): characterizes the main constituents of the solar wind plasma (protons, α particles, electrons, heavy ions) between 0.28 and 1.2 AU.

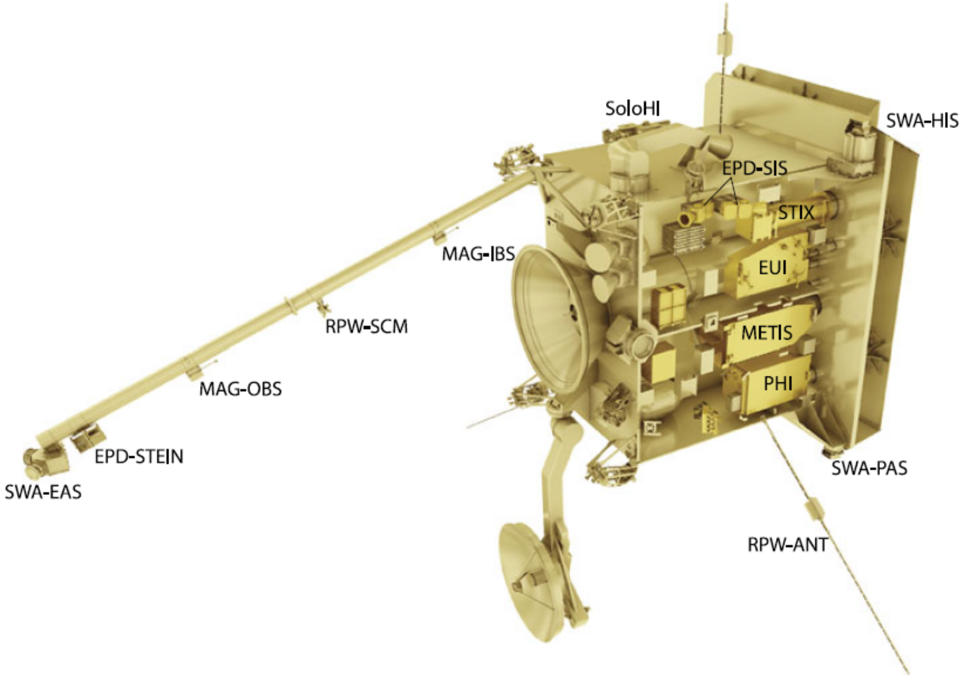

Figure 1.4: Solar Orbiter's instruments protected by the heat shield facing the Sun and the high-gain antenna.

The remote-sensing instruments are the:

- *Extreme Ultraviolet Imager* (EUI): composed of three EUV telescopes that will observe the Sun in four different wavelength bands. The telescopes are equipped with a high-resolution single-band and dual-band imager, which observe the Sun at high spatial resolution and cadence; together with a dual-band Full Sun Imager, it is continuously monitoring the Sun. It provides sequences of images of the solar atmospheric layers from the photosphere to the corona.

- *Metis coronagraph*: performing broadband and polarized corona K imaging and narrowband corona imaging in the HI Ly-α band.

- *Polarimetric and Helioseismic Imager* (PHI): providing high-resolution disk-wide measurements of the photospheric magnetic field and velocity along the Line of Sight (LOS) of the solar photosphere.

- *Solar Orbiter Heliospheric Imager* (SoloHI): a visible light telescope, copy of the SECCHI/Heliospheric Imager (HI) currently flying on the STEREO mission. It is tracking the density fluctuations in the inner heliosphere by looking at visible Sunlight scattered by electrons in the solar wind.

- *Spectral Imaging of the Coronal Environment* (SPICE): characterizing the plasma properties of regions close to the Sun.
- *Spectrometer/Telescope for Imaging X-rays* (STIX): providing spectroscopic images of solar thermal and nonthermal X-ray emission from ∼4 to 150 keV.

Since one of the core work of this PhD thesis consists in the study of the data acquired by the Metis coronagraph, one can easily understand that addressing the four previous questions is nothing but straightforward. It requires the collaboration of several teams from all over the world, where communication is as important as data processing.
The following section describes the payload and the science behind the BepiColombo mission, the second core work of this PhD dissertation.

1.3.2 BepiColombo

BepiColombo was created to acquire both complementary observations and new observations with respect to MESSENGER [17]. BepiColombo tries to answer the milestone question ”How do Earth-like planets form and evolve in the Universe?”. The main scientific objectives of the BepiColombo mission are to address the following topics, which are not isolated, but strongly coupled one to each other:

1. What is the origin and evolution of a planet close to its parent star?
2. What is the figure, interior structure, and composition of Mercury?
3. What is the interior dynamics and origin of its magnetic field?
4. What are exogenic and endogenic surface modifications such as cratering, tectonics, and volcanism?
5. What are the composition, origin, and dynamics of Mercury’s exosphere and polar deposits?
6. What is the structure and dynamics of the magnetosphere of Mercury?
7. Testing Einstein’s theory of general relativity

To answer these questions, Bepicolombo will measure the southern hemisphere to complete the observations started by MESSENGER that predominantly mapped the northern part, this is due to the MESSENGER’s highly eccentric orbit and high northern periapsis [18]. Higher-resolution images will improve the knowledge

of the cooling and tectonic history as described in the section 1.2.1.
From MESSENGER and radar measurements, deposits of water ice in shadowed craters at the poles have been discovered. BepiColombo, thanks to its polar orbit, can confirm such observations through observation of the Mercury poles.
BepiColombo is meant to determine the chemical composition of some structure present on Mercury. This is of major importance since MESSENGER made the first observations from the orbit of Mercury: finding that species such as sodium, potassium, calcium and magnesium, all exhibit different spatial distributions that do not fit with standard models. BepiColombo is also meant to provide information on the nature and abundance of carbon to help pinpoint its origin.
As for the Solar Orbiter mission, an approach to all these problematics leads to a specific instrumental conception that is presented hereafter. BepiColombo is a joint mission of the ESA and the JAXA[5], which aims to address the problematics on Mercury previously exposed. The two space agencies have organized the construction of the spacecraft as follows: the *Mercury Planetary Orbiter* module (MPO), under the responsibility of ESA; and the *Mercury Magnetospheric Orbiter* module (MMO), under the responsibility of JAXA. The MPO has a circular orbit inside the magnetosphere, and with its 11 instruments it will study: the surface

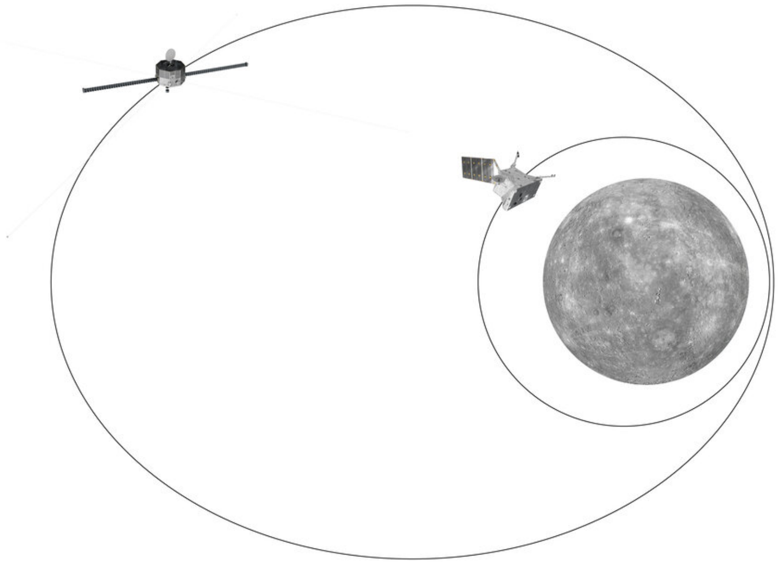

Figure 1.5: BepiColombo Orbits [19].

---

[5] The Japan Aerospace Exploration Agency (JAXA), created on October 2003, merges three aerospace organizations: the Institute of Space and Astronautical Science, the National Aerospace Laboratory, and the National Space Development Agency of Japan.

of Mercury; the internal structure; the magnetosphere and the exosphere. MMO has an external and elliptical orbit, and five instruments will study inside and outside the magnetosphere. Both modules are carried into the *Mercury Transfer Module* (MTM), developed to reach the Mercury orbit, providing the acceleration and braking required during cruise, to reach the eventual capture by Mercury and the large amount of power required by the solar electric propulsion system. The MTM with its 2 solar array wings provides power for the *Solar Electric Propulsion System* (SEPS) during the cruise. The *Magnetospheric Orbiter Sunshield and Interface Structure* (MOSIF), with its conical shape, provides the interface structure between the MPO and the MMO. It is also a Sunshield, protecting the MMO from the full intensity of the Sun until it reaches its operational orbit. The two different orbits of MPO and MMO are shown in figure 1.5. They give the opportunity to acquire information at different locations at the same time to fully understand the process of the formation and evolution of Mercury[20]. The table 1.2 summarizes the features of BepiColombo. The payloads of both MPO and MMO are presented hereafter.

	MPO	MMO
Dimensions	39.m x 2.2m x 1.7 m	diameter 1.8m height 1.1 m
Stabilisation	3-axis stabilised	15-rpm spin-stabilised
Orientation	Nadir pointing	Spin axis at 90° to Sun
Spacecraft Mass	∼1150 kg	∼275 kg
Payload mass	∼80 kg	∼45 kg
Payload power	100-150 W	∼90 W
Telemetry band	X/Ka-band	X-band
Download data time	50 kbits/s	5 kbits/s
Altitude	400x1508 km	400x11824 km
Period	2.3 h	9.3 h
Inclination	90°	90°
Argument of periherm	16°N–16°S	2°S
Nominal mission	1 year	1 year
Extended mission	1 year	1 year
Mission operation	Darmstadt, Germany	Sagamihara,Japan

Table 1.2: BepiColombo parameters in Mercury orbit [20, 21].

The MPO has a box-like shape with a size of 3.9mx2.2mx1.7m, has a three-axis stabilized configuration, and is designed to take scientific measurements along all the orbit so that the apertures of the remote sensing instruments are continuously nadir pointing. The scientific payload, shown in figure 1.6 and 1.7, is formed by:

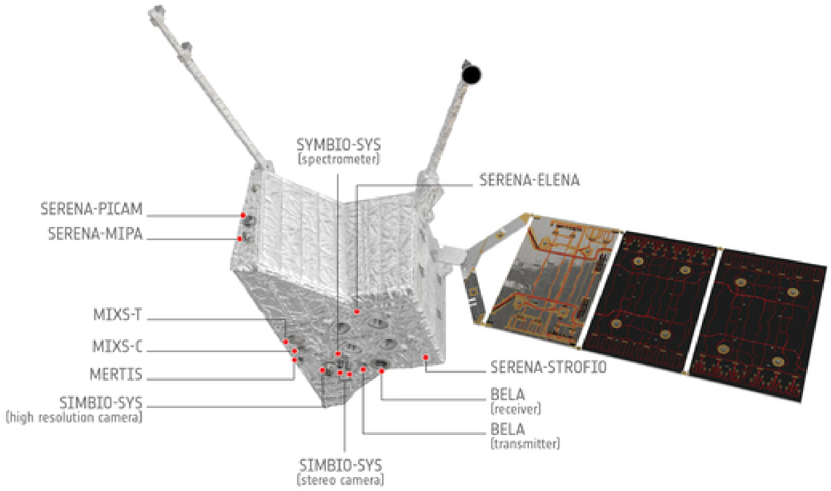

Figure 1.6: MPO instruments positions of BELA, MERTIS, MIXS, SERENA, SIMBIO-SYS (ISA, MGNS and MORE are inside the spacecraft)[22].

- *BepiColombo Laser Altimeter* (BELA), that will characterize and measure the form, topography, and surface morphology of Mercury.
- *Italian Spring Accelerometer* (ISA), the three-axis accelerometer, will characterize the geodesy and geophysics of the planet Mercury. It will also be used to test the Einstein theory of general relativity.
- *MPO Magnetometer* (MPO-MAG), which will collect magnetic field measurements to understand the origin, the evolution and the current state of the planetary interior.
- *Mercury Radiometer and Thermal Infrared Spectrometer* (MERTIS), which will provide detailed information on the mineralogical composition of Mercury's surface, by globally mapping spectral emittance with a high spectral resolution.

- *Mercury Gamma-Ray and Neutron Spectrometer* (MGNS), which will use a gamma-ray spectrometer and a neutron spectrometer to determine the elemental compositions of distinguishable regions throughout the surface of Mercury.

- *Mercury Imaging X-ray Spectrometer* (MIXS), which performs X-ray fluorescence (XRF) acquisitions (i.e. between 0.5 keV and 7.5 keV) and will produce global elemental abundance maps of key rock-forming elements.

- *Mercury Orbiter Radio-science Experiment* (MORE), which takes advantage of the microwave radio links to and from the spacecraft and will determine the gravity field of Mercury, as well as the size and physical state of its core.

- *Probing of Hermean Exosphere by Ultraviolet Spectroscopy* (PHEBUS), which will work in the ultraviolet (UV) spectral range from 55 nm (Extreme Ultra Violet, EUV) to 330 nm (Far Ultra Violet, FUV), and thus characterize the composition and dynamics of the Mercury exosphere.

- *Search for Exospheric Refilling and Emitted Natural Abundances* (SERENA), which is composed of four sensors that can be operated individually. It will provide information on the whole surface-exosphere-magnetosphere coupled system; the processes involved; plus the interactions between energetic particles, the solar wind, micrometeorites, and the interplanetary medium.

- *Spectrometer and Imagers for MPO BepiColombo Integrated Observatory System* (SIMBIO-SYS), which will be described in details in the next chapter, is an integrated suite for the imaging and spectroscopic investigation of the surface of Mercury. It is composed of a stereo camera (STC); a High spatial Resolution Imaging Channel (HRIC); and a Visible Infrared Hyperspectral Imager Channel (VIHI).

- *The Solar Intensity X-ray and particle Spectrometer* (SIXS), which is capable of broadband measurements of X-ray, proton, and electron spectra with high time resolution and a very wide FoV. It will measure X-rays and particles of solar origin at the position of BepiColombo.

MMO is a cylindrical shaped spacecraft with a diameter of 1.8 m and a height of 1.1 m. It is spin-stabilized with a nominal spin rate of 15 rpm. Since it was created for in-situ plasma and electromagnetic field measurements in the Mercury orbit, the spin axis is pointed nearly perpendicular to the Mercury orbital plane. This spacecraft is composed of the following 5 instruments, the:

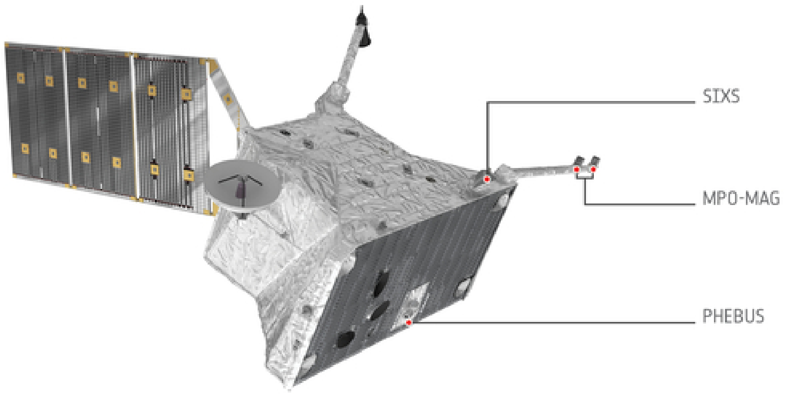

Figure 1.7: MPO instruments positions of SIXSM, MPO-MAG, PHEBEUS [22].

- *Mercury Dust Monitor* (MDM, which aims to explore the dust environment at Mercury's region of the solar system between 0.31 AU and 0.47 AU. It will measure impact momentum, crude direction, and the flux of the dust around Mercury.
- *Magnetic Field Investigations* (MGF), which is a set of magnetometers and will perform magnetic field measurements.
- *Mercury Plasma Particle Experiment* (MPPE), which is a comprehensive instrument package for plasma, high energy particle, and energetic neutral atom measurements.
- *Mercury Sodium Atmospheric Spectral Imager,* (MSASI), aiming to detect the narrow sodium D2 emission line (589 nm ± 0.028 nm), against the bright surface of Mercury.
- *Plasma Wave Investigation* (PWI), which will observe both waveforms and frequency spectra in the frequency range from DC to 10 MHz for the electric field, and from 0.1 Hz to 640 kHz for the magnetic field.

This introductory chapter describes the knowledge of the Sun and Mercury and the evolutionary history of space missions up to the two ESA missions: Solar Orbiter and BepiColombo.

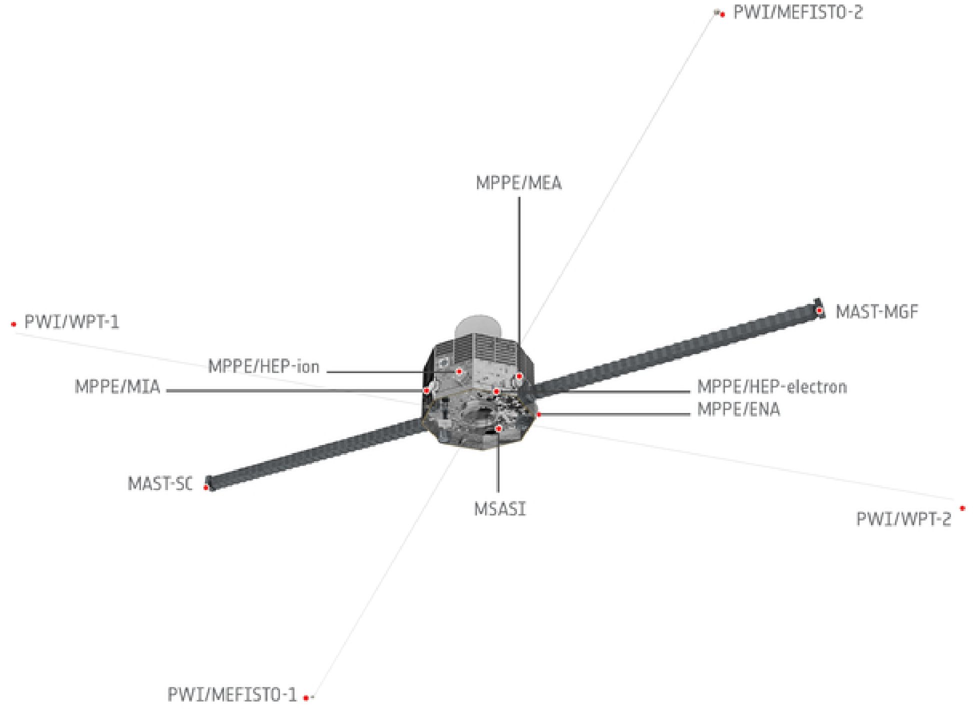

Figure 1.8: MMO instruments positions of MDM, MGF,MPPE, MSASI and PWI [23].

In the next chapter, the Metis coronagraph and the stereo camera STC will be described in detail. It elucidates the design choices concerning the necessary optical performance, the optical design, the on-board spacecraft data processing chain, and the operations executed by the instruments during observation.

Chapter 3 aims to emphasize the importance of calibrating space instruments and their integrated detectors, specifically in the context of the Metis coronagraph and STC. It begins by explaining the calibration activities, also through their crucial parameters, their significance, and their impact on the overall mission. The two primary calibration steps, i.e. on-ground calibration and simulations, are detailed in dedicated sections. The chapter wraps up by elucidating the process of in-flight image acquisition.

Chapter 4 follows a chronological sequence, focusing on the methodology used for star analysis, irrespective of its application to Metis or STC. This chapter commences with the results obtained from simulations involving stars visible to STC. Following that, the discourse transitions to the PSF analysis of stars within the observational range of Metis.

Calibration of astronomical images is indispensable for ensuring accurate scientific data, and is the topic of Chapter 5. Two critical elements in this calibration process involve flat-field correction and dark subtraction. The aim of this chapter is to delineate the flat field analysis on images captured by Metis and the dark analysis conducted on STC images.
In the concluding chapter, the primary scientific findings of both research projects are summarized and reviewed. The chapter also provides an updated status of the mission and outlines the subsequent steps in my work.

References

[1] *Science & Exploration*. URL: `https://www.esa.int/ESA_Multimedia/Images/2019/10/Anatomy_of_our_Sun`.

[2] B. Lyot. "The Study of the Solar Corona and Prominences without Eclipses (George Darwin Lecture, 1939)". In: 99 (June 1939), p. 580. DOI: `10.1093/mnras/99.8.580`.

[3] G. J. Newkirk and J. A. Eddy. "A Coronograph above the Atmosphere". In: 24 (Aug. 1962), p. 77. URL: `https://ui.adsabs.harvard.edu/abs/1962S%26T....24...77N/abstract`.

[4] R. M. MacQueen et al. "Initial Results from the High Altitude Observatory White Light Coronagraph on Skylab - A Progress Report". In: *Philosophical Transactions of the Royal Society of London Series A* 281.1304 (May 1976), pp. 405–414. DOI: `10.1098/rsta.1976.0038`.

[5] V. Domingo, B. Fleck, and A. I. Poland. "The SOHO Mission: An Overview". In: 162.1-2 (Dec. 1995), pp. 1–37. DOI: `10.1007/BF00733425`.

[6] J. L. Kohl et al. "First Results from the SOHO Ultraviolet Coronagraph Spectrometer". In: 175.2 (Oct. 1997), pp. 613–644. DOI: `10.1023/A:1004903206467`.

[7] M. Romoli et al. "The HERSCHEL/SCORE Visible and UV Coronagraph". In: *Second Solar Orbiter Workshop*. Vol. 641. ESA Special Publication. Jan. 2007, 79, p. 79. URL: `https://adsabs.harvard.edu/full/2007ESASP.641E..79R`.

[8] B. W. Denevi et al. "The Geologic History of Mercury". In: *Mercury*. Ed. by S. C. Solomon, L. R. Nittler, and B. J. Anderson. First. Cambridge University Press, Dec. 2018, pp. 144–175. DOI: `10.1017/9781316650684.007`.

[9] *Solar Syste Explaration*. URL: `https://nssdc.gsfc.nasa.gov/imgcat/html/object_page/m10_aom_19.html` (visited on 03/30/1974).

[10] *Solar Syste Explaration*. URL: `https://solarsystem.nasa.gov/missions/MESSENGER/in-depth/`.

[11] E. Martellato et al. *NASA MESSENGER Mission: A Tool to Study Mercury beyond Its Operative Life*. Other. oral, Sept. 2022. DOI: `10.5194/epsc2022-1261`.

[12] S. E. Hawkins Iii et al. "In-flight performance of MESSENGER's Mercury Dual Imaging System". In: Aug. 20, 2009, 74410Z. DOI: `10.1117/12.826370`.

[13] B. W. Denevi et al. "Calibration, Projection, and Final Image Products of MESSENGER's Mercury Dual Imaging System". In: *Space Science Reviews* 214.1 (Feb. 2018), p. 2. DOI: 10.1007/s11214-017-0440-y.

[14] *ESA Vision*. URL: https://www.esa.int/Science_Exploration/Space_Science/ESA_s_Cosmic_Vision.

[15] D. Müller et al. "Solar Orbiter . Exploring the Sun-Heliosphere Connection". In: 285.1-2 (July 2013), pp. 25–70. DOI: 10.1007/s11207-012-0085-7.

[16] M. Dikpati and P. Gilman. "Global solar dynamo models: Simulations and predictions". In: 642 (Oct. 2008), pp. 29–39. URL: https://link.springer.com/article/10.1007/s12036-008-0004-3.

[17] *BepiColombo, investigating Mercury's misteries*. URL: https://sci.esa.int/documents/34795/36289/1567260321185-ESA_BR-335_BepiColombo.pdf.

[18] R. J. Phillips et al. *3 Mercury's Crust and Lithosphere: Structure and Mechanics*. Cambridge University Press, 2018. DOI: https://doi.org/10.1017/9781316650684.004.

[19] *Solar Syste Explaration*. URL: https://www.esa.int/Science_Exploration/Space_Science/BepiColombo/From_MESSENGER_to_BepiColombo.

[20] J. Benkhoff et al. "BepiColombo—Comprehensive Exploration of Mercury: Mission Overview and Science Goals". In: *Planetary and Space Science* 58.1-2 (Jan. 2010), pp. 2–20. DOI: 10.1016/j.pss.2009.09.020.

[21] *Enabling & Support*. URL: https://www.esa.int/Enabling_Support/Operations/BepiColombo_operations.

[22] *BepiColombo MPO's Science Instruments*. URL: https://sci.esa.int/web/bepicolombo/-/59286-bepicolombo-mpo-science-instruments.

[23] *BepiColombo MMO's Science Instruments*. URL: https://sci.esa.int/web/bepicolombo/-/59284-bepicolombo-mmo-science-instruments.

2

Metis Telescope and STereo Camera (STC)

This chapter describes the two space instruments to which the in-flight calibration is applied: Metis, the coronagraph on board Solar Orbiter, and STereo Camera of SIMBIO-SYS, on board BepiColombo.
For both instruments: the design choices in terms of required optical performance, the optical design, the data processing chain on board the spacecraft, and the operations that the instruments perform during observation are explained.

2.1 Metis

The most important solar mission of the last decade is Solar Orbiter, embedding the Metis coronagraph. It is designed to study the solar corona by providing an artificial solar eclipse, by combining and extending the imaging capabilities of previous SECCHI and LASCO coronagraphs with new information with the wavelength: UV Lyman alpha. Metis features two channels: the ultraviolet H I (121.6 nm) and the visible light (580-640 nm). The next subsection presents its scientific requirements.

2.1.1 Metis Scientific Requirements

Metis was designed to provide a unique and indispensable contribution to the achievement of the scientific objectives of Solar Orbiter, which have been presented in the previous chapter (1).
All Metis contributions are summarized in table 2.1, and from the Metis coronal images the above information can be extrapolated, providing global maps for the

Table 2.1: Metis contribution to Solar Orbiter science [2].

Solar Orbiter scientific goals	Unique contribution of Metis
What is driving the solar wind and where does the coronal magnetic field originate?	Investigation of the region from which the solar wind is accelerated up to approximately its asymptotic value
How do solar transient phenomena drive the heliospheric variability ?	Investigation of the region where the first and more dramatic phase of the propagation of CMEs occurs.
How do solar eruptions produce the energetic particle radiation found in the heliosphere ?	Identification of the path of shock fronts which accelerates particles in the solar corona
How does the solar dynamo work and drive connection between the Sun and the heliosphere?	Study of the global magnetic configuration by identifying the closed and open magnetic field regions in the corona.

visible light (VL) emission: total brightness (tB) and polarized brightness (pB) (a pB sequence consists in 4 VL images, acquired at different polarization angles, i.e. 35°, 60°, 105° and 145°; the polarimeter itself is characterized with a prepolarizer, which corresponding transmission axes induce effective angles of 49.1°, 84.3°, 133.2° and 181.8°) and one for the ultraviolet (UV): HI Ly-α emission [1].

Metis is composed of four units, physically separated: the MOU (Metis Optical Unit), the MPPU (Metis Processing and Power Unit), the CPC (Camera Power Converter) and the HVU (High Voltage Unit) as shown in figure 2.1. The MOU contains all the opto-mechanical elements and detectors that gather signal coming from the solar corona in visible and ultraviolet channels.
The MPPU is mounted behind the telescope and contains the electronics that manage instrumental operations: acquiring and processing the data produced by the detectors. Moreover, the MPPU converts and distributes the power received from the spacecraft and provides the data interface with Solar Orbiter.
Above these units, is positioned the CPC which supplies the low voltage power supply to the various subsystems of the MOU including the High Voltage Unit HVU and the 2 detectors - the Visible Light Detector Assembly (VLDA), the UV Light Detector Assembly (UVDA). The first generates the high voltages to feed the intensifier of the UV channel. The harness provides all the electrical connections

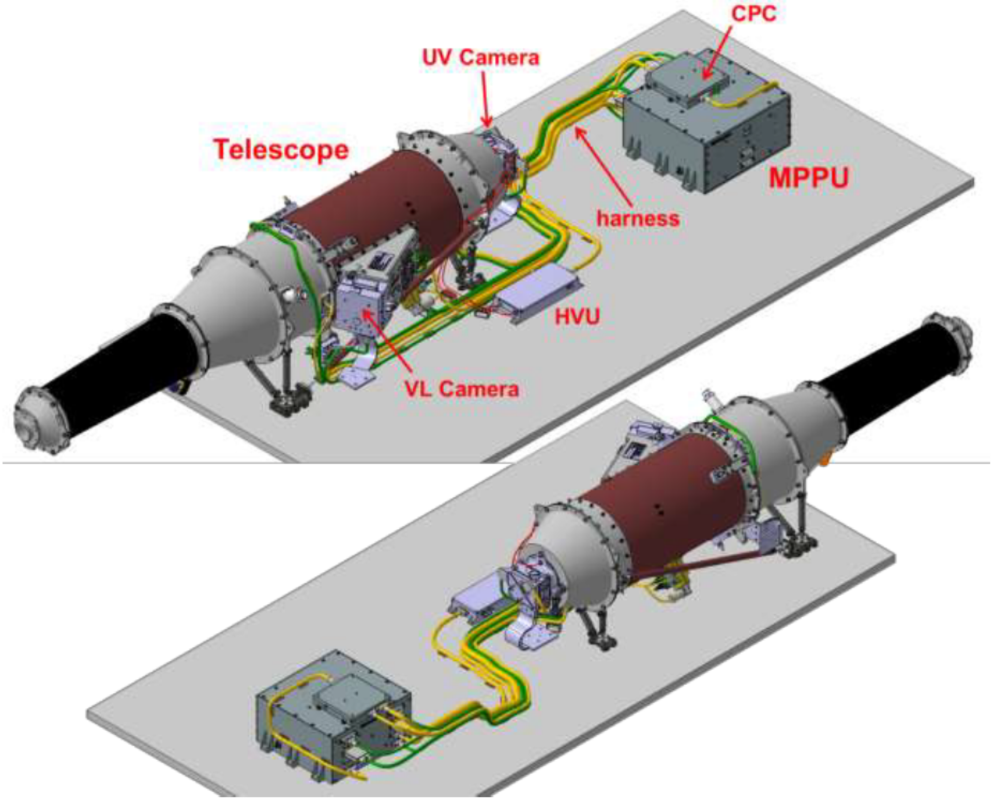

Figure 2.1: Metis Optical Unit Configuration.

between the physical units of Metis [3]. The following subsections will present: the telescope optical design; the detectors and electronics and how Metis operates.

2.1.2 Telescope Optical Design

The Metis coronagraph is an inverted externally occulted coronagraph, consisting of an on-axis Gregorian telescope, as shown in figure 2.2, coupled with a system of diaphragms to remove light from the solar disk: the external occulter. The optical design of Metis is innovative. Indeed, in the classic scheme of external occulted coronagraphs, the occulter is the outermost element, downstream of which we find the entrance opening and the telescope optics. In the inverted diagram of Metis, the most external device is the IEO (Inverted External Occulter, with a circular aperture of 40 mm) downstream of which is the actual occulter: the mirror M_0. The inverted occultation is due to the need to reduce the thermal load in the instrument during operations close to perihelion [4, 5].
The spherical mirror M_0, with a diameter of 71 mm, simulates the eclipse of the

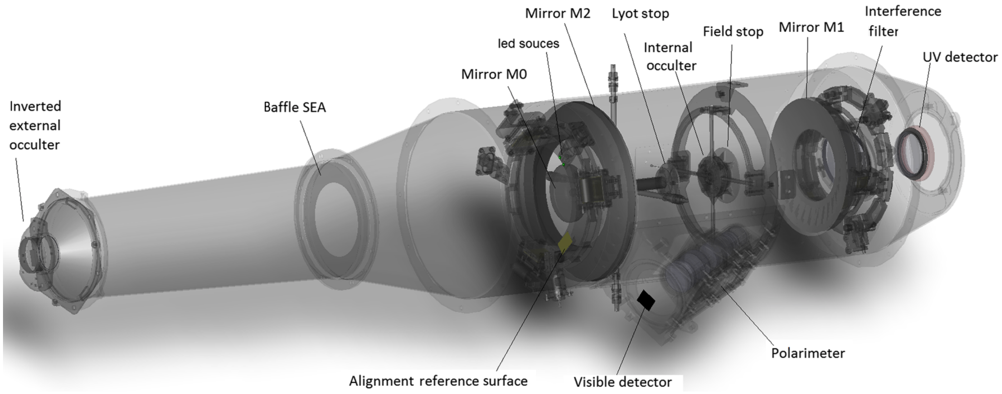

Figure 2.2: Opto-mechanical subsystem of the Metis telescope.

Sun rejecting the radiation coming from the photosphere. M_0 has a focal length equal to its distance from the IEO, so as to focus the image of the solar disk in the entrance opening, and therefore to let out the unwanted light from the instrument. Consequently, for the purposes of the main optical path, the boom simply consists of the two diaphragms IEO and M_0, which selects the coronal light, ”rejecting” the one of the disk. Mechanically, the boom is a black tube delimited at its ends by IEO and M_0 and contains the Shield Entrance Aperture diaphragm (SEA), which has the purpose of reducing the amount of light scattered inside the pipe. For this reason, the IEO shape is an inverted truncated cone [6]. The choice of the Gregorian telescope, made up of two concave mirrors, the primary mirror M_1 and the secondary mirror M_2, makes the primary focus accessible for positioning the internal occulter, IO.

The telescope contains optical elements to reduce the diffuse light produced by the edges of the external occulter IEO and by the mirror M_0. Such elements are the IO and the Lyot stop (LS).

M_1 creates real images of the edges of IEO and M_0 which are the main stray light sources. The edge image of IEO is blocked by the IO, with an outer diameter of 46.0 mm and an inner of 5.20 mm; instead the image of the edges of the mirror M_0 generated by M_1 is eliminated by the LS, which is found immediately behind the IO, as shown in Figure 2.3. In Metis the mirror M_0, the IEO, IO, LS and the IO and LS mounts are black coated with Acktar magic black^{TM}[1]. M_0, M_1 and M_2 are manufactured in Zerodur, is a lithium-aluminosilicate glass-ceramic product by Schott [4]. M_0 is coated with SiO_2. The M_1 and M_2 mirrors are made with an aluminum reflective coating and covered with a thin film (around 25 nm) of MgF_2, which has a dual purpose: it prevents oxidation of the aluminum, which

---

[1] https://acktar.com/acktar-magic-black-coating/

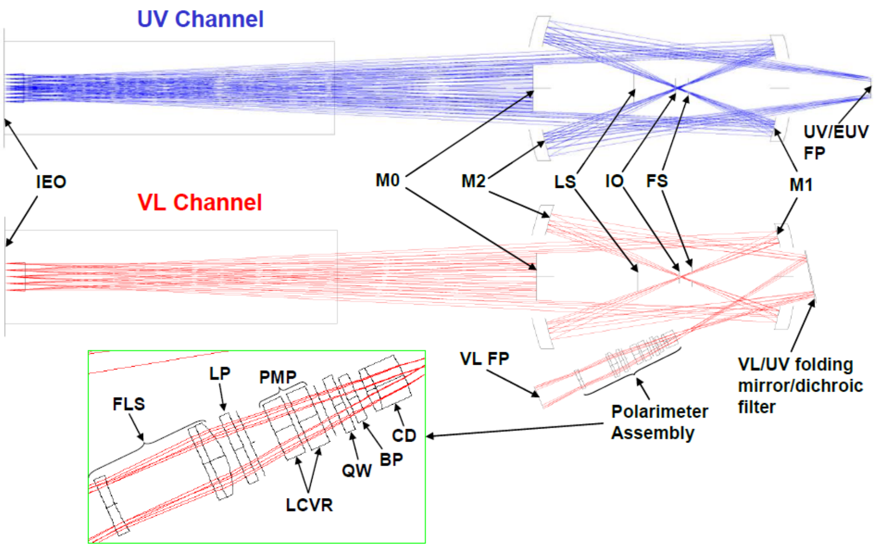

Figure 2.3: Elements of the Metis optical subsystem. Blue is the UV channel, red the channel of the visible (VL) of the coronagraph.

makes the mirror opaque to ultraviolet radiation, and increases reflectivity at the wavelength of interest.
The selection of the spectral band and of the optical path is carried out through a suitable interference filter, IF, which works as a beam splitter. It consists of a magnesium fluoride (MgF_2) window with flat and parallel faces, with an Al+MgF_2 coating that reflects the visible light in the polarimeter assembly. This filter acts as a bandpass filter at 121.6 nm ±10 nm.
Figure 2.3 shows the path of UV light (blue) and visible light (VL, red) downstream of the IEO. For the UV path, the radiation transmitted by the filter is collected directly by the UV detector (UVDA, Ultra Violet Detector Assembly, described further on in this chapter). For the VL path, the light is reflected by the IF and crosses the polarimetric group: an optical collimating system (CD collimating doublet); a bandpass filter (BP); a linear polarization analyzer that consists of a quarter-wave plate (QWP), liquid crystal (LCVR, liquid crystal variable retarder - Electro-optical Polarization Module Package, PMP), and a linear polarizer (LP) [7]; the light is then focused on the Visible Channel Detector Assembly (VLDA).
In order to reduce the reflection effects, all the lenses have a single-layer anti-reflection coating, the LP also has an MgF_2 coating, and the QWP a multi-layer AR coating. All the optical parameters of the telescope are summarized in Table 2.2.

As described before, the objective of Metis is to study simultaneously the solar

Table 2.2: Metis optical parameters [5].

Field of view	1.6° - 2.9° or 1.6 $R_\odot$ - 3.0 $R_\odot$at 0.28 au ; 6.0 $R_\odot$ - 11.0 $R_\odot$ at 1.0 au
Wavelength bandpass	UV: H I Ly-α (121.6 $\pm$ 10) nm VL: 580-640 nm
Telescope type	externally occulted, on-axis Gregorian
Effective focal length	UV: 300 mm , VL: 200 mm
$\mathrm{F-number}$ (without occultation)	UV: 7.5 - VL: 5
Spatial resolution	VL:10.7 arcsec UV: UV:20.0 arcsec
Distance IEO-M0	800.0 mm
Distance M0-M1	370.6 mm
Distance M1-M2	363.0 mm
Distance M1-LS	219 mm
Distance M1-IO	153.9 mm
Distance M2-focal plane UV	505.2 mm
External Inverted Occulter (IEO)	Truncated Cone Occulter outer $\varnothing = 40$ mm
Sun disk light rejection mirror M0	Spherical: $\varnothing = 71.0$ mm Curvature radius: 1600.0 mm
Primary mirror M1	Ellipsoid on axis: outer $\varnothing = 163.0$ mm, inner $\varnothing = 88.0$ mm Curvature Radius: 272.0 mm, conic: -0.662
Secondary mirror M2	Ellipsoid on axis: outer $\varnothing = 219.0$ mm, inner $\varnothing = 125.0$ mm Curvature Radius: 312.4 mm, conic: -0.216
Internal Occulter	$\varnothing = 5.0$ mm
LS	Circular darkening: $\varnothing = 47$ mm
Detectors	UV: Intensified APS, Image size: 30.7 mm (1024 × 1024 pixels), scale factor: 20 arcsec/pixel, pixel size: 30 μm VL: APS, Image size: 20.5 mm (2048 × 2048 pixels), scale factor: 10.126 arcsec/pixel for x-axis 10.139 arcsec/pixel for y-axis, pixel size: 10 μm

corona in both polarized light in the band broad visible (580-640 nm) and in narrowband UV Ly-α (121.6 nm) with an unprecedented temporal resolution (10 s). In figure 2.4 is shown the simulation of the Metis Field of View (FoV). The Fov depends on the distance of the Sun: it is 1.5° to 2.9° from the center of the Sun, which corresponds to 1.6 $R_\odot$ - 3.1 $R_\odot$ (3.6 $R_\odot$ at the corner) when the spacecraft (S/C) is at minimum perihelion (0.28 AU) and from 6.0 $R_\odot$ to 10.8 $R_\odot$(12.7 $R_\odot$ at the corner) at 1.0 AU.

In the next subsection, the detectors for both channels and the electronics are described.

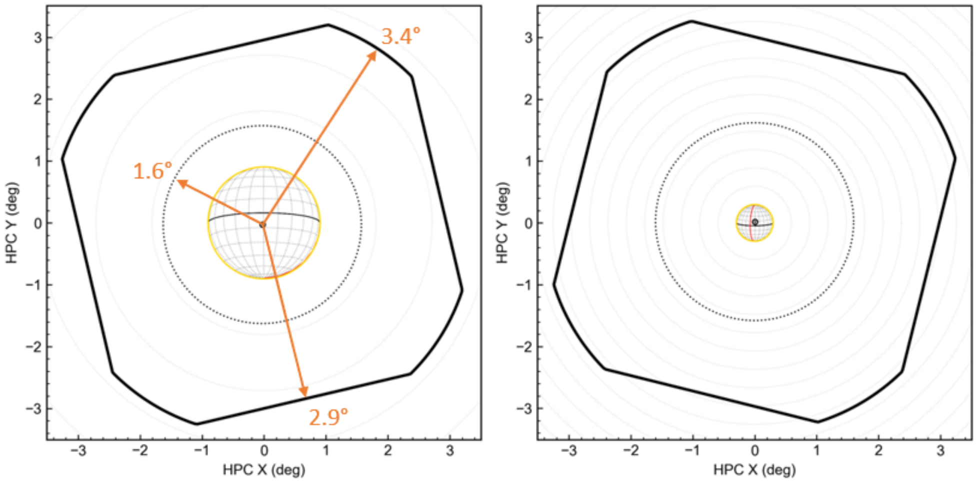

0.28 AU
1.7-3.1 (3.6) $R_\odot$

1.0 AU
6.0-10.8 (12.7) $R_\odot$

Figure 2.4: Simulation of the Metis FoV for two distances from the Sun: 0.28 AU (minimum perihelion) and 1.0 AU. The Sun is in the center, the square with rounded sides is the field of view of Metis. Courtesy of Roberto Susino.

2.1.3 Detectors and electronics

The UV detector (UVDA) and Visible Light detector (VLDA) were developed by MPS[2] specifically for the Solar Orbiter mission.

The UVDA is located at the focal plane of the UV channel, as shown in figure 2.3. It consists in a Micro Channel Plate (MCP), with a K-Br photocathode, and is optically coupled, via an optical fiber cone, to an Active Pixel Sensor (APS, 1024 x 1024 pixels). A scheme and a model are shown in figure 2.5. The cone resizes

---

[2] Max-Planck-Institut fur Sonnensystemforschung, Gottingen, Germany

the image of the focal plane on the detector so that it fits the sensor dimensions. Scaling is 2:1, so the 15 µm pixel size of the APS detector results in an effective 30 µm focal plane sampling element. The acquired data is then transferred to the MPPU for subsequent processing. The detector can either operate in analog mode or in photon counting mode (described in a following subsection) depending on the gain of the intensifier. In analog (or integration) mode, the UVDA collects the charge created by the incoming photons throughout the set integration time. In photon counting mode, the UVDA enhancer is operated at a given gain so that each single photon hitting the photocathode produces a signal on the APS. The APS will read at its maximum rate of 10 frames/s, which is sufficient to have no more than one photon hitting a single pixel per frame read. The position of the single photon is identified via the centroid of the light distribution and its coordinates are transmitted by telemetry. The supply voltages required by the MCP and the phosphor screen are supplied by an external HVU unit.

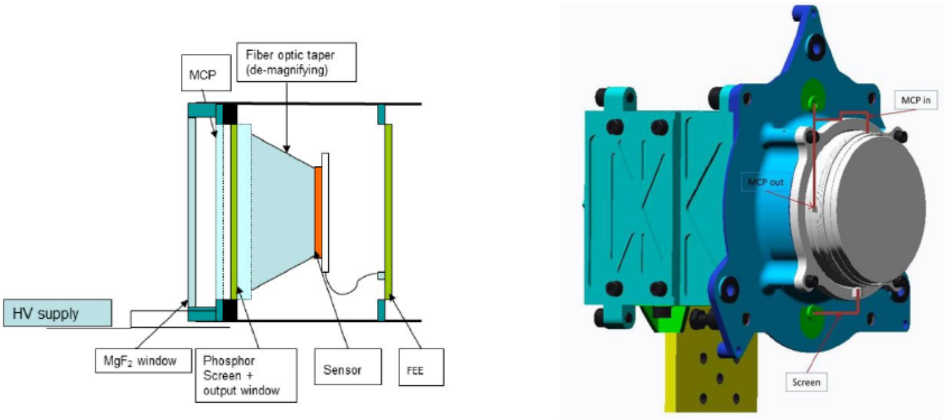

Figure 2.5: left: APS scheme. Right: 3D model of the UVDA. [3]

The VLDA is a CMOS camera sensitive to visible light. It has been built in a very similar manner to the one used for the PHI instrument (developed by MPS), another instrument aboard Solar Orbiter. The VLDA is based on a CMOS APS sensor developed by CMOSIS[3] with 2048 x 2048 pixels, which are 10 μm in size. Although the detector allows for a reading of 10 frames per second, it operates at a lower frequency, with a minimum integration time of 1 second. In the analog (or integration) mode, the VLDA collects the charge created by the incoming photons during all the set integration time. The data, as in the UVDA, are transferred via a connection interface to the MPPU unit.

---

[3] reference http://www.cmosis.com/

The MPPU acquires and processes VL and UV channel data, controls telescope mechanisms and thermal hardware embedded on the MOU. The MPPU provides all the control and management functions of the Metis hardware, implements the data processing and storage algorithms, and constitutes the communication interface with the spacecraft managing the exchange of remote controls and TM/TC telemetry (telemetry and telecommands) [3].

In the next section, the operation procedure to command the acquisition of Metis to reach the scientific objectives is described.

2.1.4 Operation

Solar Orbiter is a deep space mission, for this reason it is impossible to operate the various instruments in real time, and the observations to be carried out have to be planned in advance. In Metis, the specific observation methods have been defined in order to achieve the foreseen scientific objectives. There are two planning: the Long Term Planning (LTP) that covers a six-months period, which approximately corresponds to an orbit, and the Short Term Planning (STP) that covers more or less one week, and it is the unit that composes the LTP. In the LTP, all Solar Orbiter instruments are built according to a coordinated plan, to address the scientific objectives [8]. In the STP case, a detailed schedule of commands for the spacecraft and for the payload instruments has to be built.
To achieve the Metis specific target of interest, there are two types of observation modes: Standard and Special. The former includes the nominal observational modes of the instrument, in which observational campaigns are carried out for the various "case studies" identified at a scientific level, while the latter are observational modes that can be used in particular situations, such as the transit of a sun-grazing comet or in case of solar flares, or to exploit joint observations with other missions like the Parker Solar Probe (PSP). Both observation modes are described below. The nominal modes, the so-called standard modes, are the following:

WIND: measures the electron density and speed of the outward-expanding solar wind. Fast and slow solar wind fluxes are identified in the global maps based on the velocity values of the flow of hydrogen.

MAGTOP: measures wind flow speed and its relation to magnetic topology. It measures speed along streamer/coronal hole interfaces, past streamer cusps and into streamers.

GLOBAL: before, during, and after CME events, it performs global measurements of the corona evolution. These provide the geometry of neutral hydrogen and coronal electrons and its evolution over time, enabling to extract information on the timing, on the mass contained, and on the dynamics of coronal mass ejections. These observations are crucial for measuring the direction of the plasma erupted by the Sun, in order to infer their interaction with the Earth and to predict their impact on our planet.

LT (Long Term)-CONFIG: it follows the evolution of the coronal configuration. These measurements are used to monitor the evolution of the corona on a large scale and, during observation windows outside the ecliptic plane, to determine the longitudinal distribution and evolution of the electron density in the solar corona, as well as the flux of mass and energy carried away by the solar wind.

FLUCTS and TBF (Total Brightness Fluctuations): they provide spectra of brightness fluctuations (and optimized in perihelion).

The Special observation modes are:

CMEOBS: it is triggered by a CME event (flag). Such measurements can be used to identify the path of accelerated particles in the outer solar corona. Also, combined with radio observations from RPW, they can help distinguish flare-accelerated SEPs from those from CMEs. It tracks CME eruption and propagation, associated with shocks and filaments, and SEPs accelerated by the CME. It measures the electron density and the outward expansion velocity gradient.

COMET: it maps the emission of Sun-grazing comets. These measurements are used to monitor the evolution of comet emission along their trajectory near the Sun.

PROBE: there will be coordinated observations with Parker Solar Probe, and it will characterize the properties of the coronal regions encountered by the PSP, during its transit near the Sun.

Each observational mode is conceived as a continuous repetition of a basic acquisition, suitably configured, with a duration with a given repetition rate (cadence). The cadences for the Standard modalities range from 5 to 30 minutes, and are usually repeated to cover observational campaigns of several hours, if not even days during the various observation windows of the mission.
The Special modes are usually performed with reduced cadences: about one minute, with a total duration of a few hours.
In addition to these modes, Metis can also perform synoptic observations, simultaneously for both channels if the distance between the S/C and the sun is less

than 0.6 AU, just in VL in the when the distance is greater than 0.6 AU. Metis produces four VL images per cadence to obtain pB or tB data, and just one image per cadence for the UV.
Currently, the events that could modify the normal Metis observation plan are: the detection of a transient event such as a CME, identified by an internal Metis algorithm, or signaled by other Solar Orbiter instruments; and the overillumination due to the entry of the solar disk into the FOV of Metis, due to incorrect pointing by the S/C. The latter triggers a safety procedure intended to preserve the functionality of the detectors (in particular the UVDA intensifier), which leads the instrument to interrupt normal acquisition and to switch the detectors off.
The detection of a transient event arising in the Metis field of view is performed through the analysis of VL image sequences. Two consecutive images are acquired and the normalized relative difference is calculated. The average of the pixels belonging to predetermined sectors is then calculated, and the value, thus obtained, is compared with respect to a certain threshold. This check is carried out to detect significant changes from one image to the next; if several sectors exceed the preset threshold, the on-board SW track a CME event.

Other instruments on board Solar Orbiter implement similar functions, and, precisely in order to exploit this potential and coordinate a possible observation with more instruments, a dedicated channel is foreseen for the exchange of information between the various experiments.
The data obtained from the operations described just above have been used for the analysis described in Chapter 4 and in Chapter 5, the main topics of this work along with the Zemax simulations.
In the next section, the channel STC on board of BepiColombo will be described, starting with a brief description of the instrument it belongs to: SIMBIO-SYS.

2.2 SIMBIO-SYS

The instrument *Spectrometer and Imagers for MPO Bepicolombo Integrated Observatory SYStem* (SIMBIO-SYS) on board of BepiColombo mission was created to provide images and 3D map of the mercury surface. To do that SIMBIO-SYS is composed by three channels: Stereo Camera (STC), High Resolution Camera (HRIC) and the Spectrometer (VIHI) as shown in figure 2.6. To limit the mass of the instrument, the channels have a common main electronics and power supply. STC and VIHI also share the same structure, including detectors and Proximity Electronics (PE). In detail the SIMBIO-SYS instrument is able to perform:

- global mapping with stereo imaging, with a spatial resolution between 60 and 120 m, with an accuracy of 84 m at the periherm on the equator;

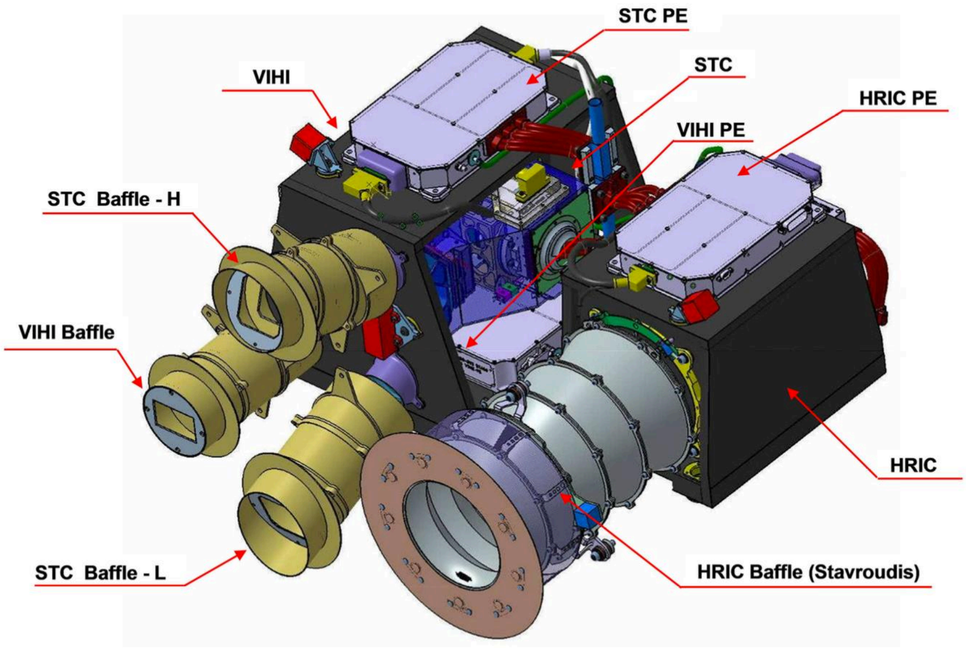

Figure 2.6: SIMBIO-SYS FM 3D configuration [9].

- colour mapping of selected regions in 4 broad band filters, in the range 410-930 nm;
- global mapping with spectroscopy in the spectral range 400 - 2000 nm, with a spatial resolution better than 500 m;
- high spatial resolution imaging, in the range 400-900 nm, of selected areas with a spatial resolution between 6 and 12 m in a panchromatic filter and in 3 different broad band filters;
- hyperspectral imaging of selected areas in the spectral range 400 nm - 2000 nm with a spatial sampling less than 120 m.

Before describing STC, the other two channels, HRIC and VIHI, will be described. As written above, they belong to the same instrument.
The scientific objective of HRIC is the characterization of special surface targets at high resolution, as the name of this channel suggests. Structurally, HRIC is a modified Ritchey-Chretien with the mirrors adapted to correct astigmatism and the FoV curvature aberrations. It provides a panchromatic filter, in the 400-900 nm range, and three band-pass filters with central wavelengths at 550, 750, and 880 nm. The FOV are: 0.46° x 1.47° for the panchromatic; and 0.25° x 1.47° for the coloured filter. The light is collected by the detector APS (developed by Raytheon

Vision Systems), a SiPIN CMOS of 2048×2048 square pixels of 10μm.
VIHI is a hyperspectral imager and has multiple scopes: mapping Mercury in order to provide the global mineralogical composition of the surface with a spatial resolution of 400m; identifying mineralogical species with a confidence level between 5 and 10%; correlating surface composition and surface characteristics at a scale of 400 m globally, and up to 100 m in selected places.
VIHI is a modified Schmidt telescope with a dioptric doublet to correct the aberration. After the entrance there are, in this order: a slit, a spectrometer, and a flat grating. The optical path continues towards the detector, which collects both visible and infrared light in the range 400-2000 nm. Its FoV is 3.67 x 0.01°. The detector is developed by the same industry of HRIC (same for STC), the Raytheon Vision Systems, and is a HgCdTe CMOS 256x256 square pixels, of 40μm.
In the next section, the channel STC is described in details.

2.3 STC

MDIS acquired many images from which extrapolating scientific information was more straightforward. However, since the coverage of the Mercury surface needs to be increased and improved, this is one of the scopes of STC. In this section, STC is presented from its scientific requirements to its operation, passing by its optical design, its detectors, and how the data acquired is processed.

2.3.1 STC Scientific Requirements

The STC scientific requirements are strictly correlated to those of SIMBIO-SYS, furthermore most goals can be achieved with the synergy of other instruments present on board of BepiColombo such as: MERTIS, PHEBUS, BELA, MIXS and MGNS.
The scientific goals and the SIMBIO-SYS contributions are described in details in the Cremonese article in [10]. The scientific objectives of STC are:

- mapping the entire surface of the planet and determine the location, size and height of the major structures;
- generating a global Digital Terrain Model (DTM), in order to map the global height distribution of the Mercury's surface;
- obtaining detailed stereo maps of selected targets of the surface of Mercury, in order to get DTM with a grid size of at least 2 pixels;
- obtaining colour mosaics, using all the colour filters, of selected regions of the surface of Mercury.

The objectives to achieve are strictly correlated to the optical design of the instruments. If the objective is to study the surface composition and the main geological units, the spectral bands have to be what was chosen for STC. If the resolution scale is 50 m per pixel at the equator and 110 m per pixel at the poles, the optical layout is that of STC, and it is described in the next subsection. A 3D layout is available in [11].

2.3.2 STC Telescope Optical Design

In order to cope with the scientific objectives, but also those regarding mass, volume, power and movable parts of the instruments, STC consists in two subchannels: High and Low with an inclination of -20° and $+20^\circ$ respect to the Nadir. Each channel is composed by a panchromatic, with central wavelength at 699.5 nm and 2 coloured filters: F920 and F550 for the Low channel, with respective central wavelengths at 923.8 nm and 550 nm; for the channel High F420 and F750 with central wavelengths, respectively, at 420.6 nm and 749.6 nm.
Therefore, the front unit of STC consists in two independent fore-optics modules, one for each subchannel; then there is the modified Schmidt telescope unit as shown in figure 2.7. The optical path for one subchannel is the following: looking at Mercury, the light, that respect to the nadir, has an inclination of $20^\circ \pm 2.38^\circ$

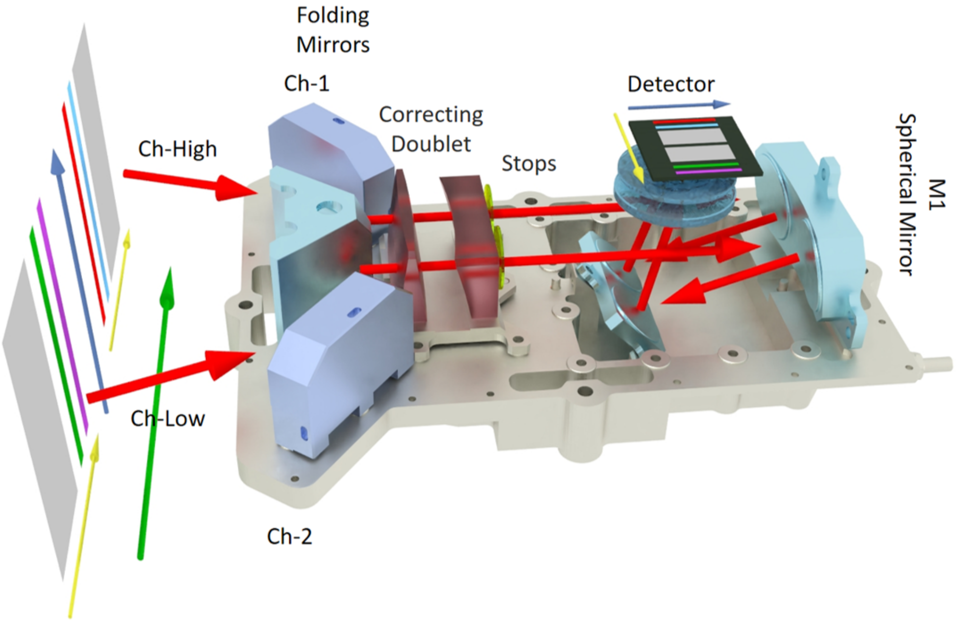

Figure 2.7: STC optical path [10].

enters in STC passing through the external baffles, is reflected inside folding mirrors, as shown in figure 2.7, passed through a correcting doublet, the aperture stop (AS) and arrives on the spherical mirror M_1. It then reflects on a telescope mirror, positioned off axis, which in turn reflects into a two-lens field corrector and arrives on the focal plane assembly (FPA). The FPA is composed of the filter that selects the wavelengths, and the detector, an APS-CMOS, which will be described in details later. The optical path for the other channel, with an incoming light inclination of -20°±2.38° must also be considered [12]. The selected elements present the following advantages:

- the prisms avoid the throughput losses thanks to the total internal reflection at the glass–air interface;
- as the name says, the correcting doublet corrects the residual aberrations of the primary mirror. The residual chromatic aberration is negligible in the whole spectral range of interest (410–930 nm);
- the AS position prevents wavelength shifts at the filter strip assembly (FSA), and balances the aberrations over the entire FoV;
- the off-axis configuration avoids central obstruction and supports structures allowing an optical Modulation Transfer Function (MTF) of about 0.65-0.69, and a Point Spread Function (PSF) of 1.36/1.45 px.

All the STC parameters are summarized in the table 2.3.

2.3.3 STC Detectors

The FSA is 1 mm from the detector, it is composed of 5 different pieces, one for each colour or panchromatic, for a total of 6 windows. The glass pieces were glued together in the white areas (gaps) shown in figure 2.8. This technique was the most reasonable solution to avoid mechanical elements needed to change the filter (the solution used for MDIS on board of MESSENGER, a mechanical wheel, was not applicable here). As shown in figure 2.8, outside the illuminated part, there is a Window X (or winX) that permits acquiring dark images: in fact, it will be used as a dark current monitor.

The corresponding Fov for both sub-channels is 5.3°×4.5° with gaps included, which corresponds to an area of about 40 km × 19 km on Mercury's surface. In the table 2.4 are described the starting and ending vertical and horizontal coordinates in degree and pixel. As is shown, the scientific areas are smaller because the GAP is not included in science. This configuration allows to acquire simultaneously for different wavelengths three quasi-contiguous areas of Mercury surface in different colors. The detector is a hybrid CMOS active pixel sensor (APS), using silicon

Table 2.3: STC optical parameters [10].

Optical Concept	off-axis modified Schmidt (unobstructed)
Strategy	Stereo-push frame
Maximum FoV (cross track)	5.38°
Panchromatic FoV (along track)	0.38°
Coloured filter FoV (along track)	2.31°
IFov	105 μrad
Mean Focal length	95.2 mm
Focal ratio	F/6.3
Optical distortion	<0.3%
Optical MTF	0.65-0.69
PSF (FWHM)	1.36/1.45 px
Pupil size	15 mm
Detector type	SiPIN CMOS
Full well	90300 electrons
Quantum efficiency 450/850 nm	91% / 83%
Pixel size	10 μm

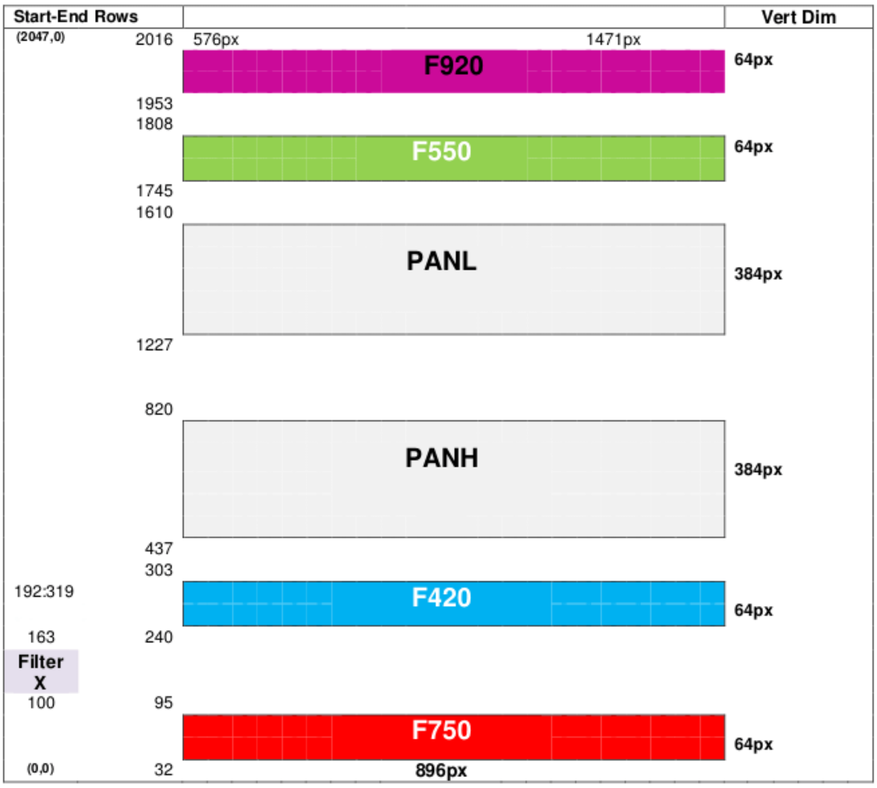

Figure 2.8: Focal Strip Assembly (FSA). Start-End-Row column identify the starting and ending rows for each filter (rows included). Horizontal coordinates are expressed in pixel [9].

PIN diodes (Si PIN) with Raytheon's anti-reflective coating, with an array of 2048 × 2048 square pixels of 10 μm. The choice of this particular detector has been done on the basis of its radiation hardness necessary to sustain the hostile Mercury environment, and is backside illuminated to achieve the 100% of fill factor.
The quantum efficiency (QE) for the wavelength range of interest, 400 - 950 nm, is very high, between the 83% and 91%. The modulation transfer function is in the 0.65-0.69 range [13].

The STC detector allows snapshot image acquisition with a minimum integration time of 400 ns. Mercury's images will be acquired in the push-frame mode, which is a mixed mode between frame and push-broom mode. In the frame mode, the frame camera collects an entire image at a single instant in time, while a push-broom camera collects one line of image data over a time range and builds a two-dimensional image through the spacecraft motion. The push-frame cameras collect a small multiple of lines in one integration, and build up a complete im-

Filter	Raw Definition		Columns Definition		Dimension		Bsight Dir	FOV	Angle def (vs Nadir)	
	Start	End	Start	End	Rows	Cols			Start	End
	[px]	[px]	[px]	[px]	[px]	[px]	°	°	°	°
F750	32	95	576	1471	64	896	17.95	0.38	17.76	18.14
GAP	96	239	576	1471	144	896	18.59	0.87	18.15	19.02
F420	240	303	576	1471	64	896	19.22	0.38	19.03	19.41
GAP	304	436	576	1471	134	896	20.30	0.81	19.89	20.70
PANH	437	820	576	1471	384	896	21.38	2.31	20.22	22.53
GAP	821	1226	576	1471	406	896				
PANL	1227	1610	576	1471	384	896	21.38	2.31	20.22	22.53
GAP	1611	1744	576	1471	134	896	20.30	0.81	19.89	20.70
F550	1745	1808	576	1471	64	896	19.22	0.38	19.03	19.41
GAP	1809	1952	576	1471	144	896	18.59	0.87	18.15	19.02
F920	1953	2016	576	1471	64	896	17.95	0.38	17.76	18.14
WinX	100	163	192	319	64	128				

Table 2.4: Definition of the starting and ending vertical and horizontal coordinate, dimensions and boresight of the filters on the FSA in terms of pixels and Fov. FoV is defined for each pixel row, both in the Nadiral reference system (angles on ground). All filters (WinX excluded) are considered horizontally from pixel 576 to 1472 with a FoV of 5.38°, centered in nadiral direction [9].

age through downtrack motion of the spacecraft [14]. The push-frame acquisition method allows for some overlap of the imaged regions in the along-track direction, increasing the image matching accuracy, and taking into account possible small drifts of satellite pointing.

The following subsection focuses on the concrete operation of STC.

2.3.4 OPERATION

Due to the independence of its two subchannels High and Low, and the configuration of its filters as presented in 2.3.2, STC offers exceptional flexibility in terms of operational possibilities. Depending on the mission phase and objectives, STC can operate with one or both subchannels, capturing stereo image pairs or color pictures, employing different combinations of filters, window sizes, and compression ratios for each subchannel independently. The ability to define various compression ratios and cross-track sizes of acquired frames allows STC to optimize data volume, while maintaining high scientific quality. This flexibility enables the instrument to meet scientific requirements while adapting to any kind of situation from over-favorable to critical.

Concretely, to achieve the STC objectives described in the section 2.3.1, STC can be operated in order to obtain: global stereo mapping; stereo mapping of selected regions, and colour mosaics of selected regions.

The global stereo mapping of Mercury's surface is planned to be completed within the first 6 months of the mission (which will start on December 5th 2025). Any remaining gaps in the mapping will be filled during the following 6 months. This mapping effort aims to generate a Digital Terrain Model (DTM) of the entire surface, enhancing the interpretation of morphological features, topographic relationships, and geological units. It will also facilitate the identification of large to middle-scale tectonic features, impact craters, and potential volcanic edifices and lava flows.

Stereo mapping of selected regions and colour mosaics are planned to be used in the second part of the mission. Indeed, STC will focus on predefined targets selected for their scientific interest, or on areas not covered in the initial mapping phase. For these specific targets, different operational modes will be employed, such as capturing color mosaics using specific filters or acquiring high-resolution DTM data with a grid size of at least two pixels.

Globally, as described in the section 2.3.3, an STC acquisition cycle results in one or more rectangular frames (a data frame), representing a subset or window on a filter of the detector. The size of the window is determined by the number of pixels cross-track (defined by the filter), and along-track (determined by the observation strategy, detector characteristics, and compression algorithm). The number of frames acquired concurrently in an acquisition cycle depends on the operating mode, including the number of filters and subchannels used.

The operational modes defined for STC are STAND-BY: after switch-on or while transitioning between modes; and SCIENCE, during which science data are acquired. The SCIENCE mode comprises various submodes organized into subgroups, each of them being characterized by different filters combinations, compression ratios, along-track window sizes, data rates, and repetition times:

- The *Stereo mapping* (SM) submodes are primarily employed for the global stereo mapping of Mercury's surface, using the two panchromatic filters. Different SM submodes account for the dependence of the cross-track window size on latitude. These submodes are therefore mainly used in the first part of the mission, and may be utilized during the second part to fill any remaining gaps.

- The *Color mapping* (CM) submodes focus on capturing color mosaics of large regions using only the four color filters with minimal frame overlapping. These submodes are employed during the second part of the mission, and similar to SM, they consider the dependence of the cross-track window size on latitude.
- *In-flight calibration* (IC) submode aims to observe stellar fields to map distortions across the Field of View (FoV) and facilitate geometric and radiometric calibration. This submode is conducted twice per Mercury year, at specific true anomalies along the planet's orbit, and will be described in detail in the next chapter.

Finally, the STC *Long-Term Science Plan* can be summarized as follows:

- In the first 6 months of the mission STC will work continuously, to cover with both panchromatic filters the whole surface of the planet. The operative submode that will be used is Stereo mapping. The submodes succession is defined on the basis of an orbit arc around the planet, from the South pole to the North pole; this arc is subdivided into segments on which the submodes are defined. For the first two segments there are two possible submodes, to be selected on the basis of the desired cross-track overlapping, which is very important for the accuracy of the stereo reconstruction. The data volume allocated for this phase is 130 Gbit, already compressed by a factor 7.
- Local mapping used as color mosaics to acquire color pictures on selected regions of Mercury, the Color mapping submode group will be used; there are 5 submodes, corresponding to a different number of cross-track pixels in the window. The color coverage will use 42.6 Gbit corresponding to the 15% of the Mercury surface.
- Local mapping used as detailed stereo mapping: the stereo mode could be used to obtain on selected targets a stereo reconstruction, and hence a DTM, with a higher accuracy than during the global mapping.

During the detailed stereo mapping phase, STC focus will be on small targets using a mode similar to Stereo mapping. However, in this phase, we will employ a more favorable compression ratio potentially utilizing lossless compression with an average compression ratio of around 2. Moreover, STC acquisition ensures maximum possible overlapping between consecutive tracks to enhance accuracy. Assuming these conditions, a data volume of 50 Gbit will be required to cover approximately

10% of the surface.

Another secondary objective involves achieving color coverage for an additional 35% of the surface, requiring a total data volume of 99.4 Gbit. This objective complements the detailed stereo mapping and represents a further enhancement of our understanding of the surface characteristics of Mercury. [9].

This chapter presented the instruments used during this PhD thesis: the Metis coronagraph on board of Solar Orbiter; and the stereo camera STC aboard BepiColombo. First acquisitions and data processing have already been done and are the core of the chapter 4 and 5. However, prior to operating any kind of interpretation, these instruments need to be calibrated in-flight for the reasons exposed in the chapter 3. This is why I present in the next chapter the calibration ”theory”.

References

[1] M. Romoli, G. Nicolini, and M. Romoli. *Instrument User Manual.*

[2] D. Müller et al. "Solar Orbiter . Exploring the Sun-Heliosphere Connection". In: 285.1-2 (July 2013), pp. 25–70. DOI: `10.1007/s11207-012-0085-7`.

[3] M. Pancrazzi et al. "Hardware and Software Architecture on Board Solar Orbiter/METIS: An Update". In: *SPIE Astronomical Telescopes + Instrumentation.* July 2014, 91443F. DOI: `10.1117/12.2055865`.

[4] E. Antonucci et al. "Metis: The Solar Orbiter Visible Light and Ultraviolet Coronal Imager". In: 642, A10 (Oct. 2020), A10. DOI: `10.1051/0004-6361/201935338`.

[5] S. Fineschi et al. "Optical Design of the Multi-Wavelength Imaging Coronagraph Metis for the Solar Orbiter Mission". In: *Experimental Astronomy* 49.3 (May 2020), pp. 239–263. DOI: `10.1007/s10686-020-09662-z`.

[6] F. Landini et al. "Stray Light Calibration for the Solar Orbiter/Metis Solar Coronagraph". In: *International Conference on Space Optics, ICSO 2018.* Vol. 11180. Society of Photo-Optical Instrumentation Engineers (SPIE) Conference Series. July 2019, 111802I, p. 111802I. DOI: `10.1117/12.2536009`.

[7] G. Capobianco et al. "Polarimetric Calibrations and Astronomical Polarimetry in the V-band with Solar Orbiter/METIS Instrument". In: *Space Telescopes and Instrumentation 2014: Optical, Infrared, and Millimeter Wave.* Vol. 9143. Society of Photo-Optical Instrumentation Engineers (SPIE) Conference Series. Aug. 2014, 91434V, p. 91434V. DOI: `10.1117/12.2057368`.

[8] F. Auchère et al. "Coordination within the Remote Sensing Payload on the Solar Orbiter Mission". In: 642, A6 (Oct. 2020), A6. DOI: `10.1051/0004-6361/201937032`.

[9] L. Tommasi. *SIMBIO-SYS FM User Manual.* Copyright Leonardo S.p.a. All Rights Reserved. 2018.

[10] G. Cremonese et al. "SIMBIO-SYS: Scientific Cameras and Spectrometer for the BepiColombo Mission". In: *Space Science Reviews* 216.5 (), p. 75. DOI: `10.1007/s11214-020-00704-8`.

[11] *STC interactive optical path.* URL: `https://www.dei.unipd.it/~dadeppo/STC.html`.

[12] V. Da Deppo et al. "Optical design of the single-detector planetary stereo camera for the BepiColombo European Space Agency mission to Mercury". In: *Applied Optics* 49.15 (May 20, 2010), p. 2910. DOI: `10.1364/AO.49.002910`.

[13] R. E. Mills, J. J. Drab, and A. Gin. “Advanced staring Si PIN visible sensor chip assembly for Bepi-Colombo mission to Mercury”. In: Aug. 20, 2009, 74390A. DOI: 10.1117/12.827036.

[14] *Challenges Utilizing Pushframe Camera Images*. URL: https://www.lpi.usra.edu/meetings/lpsc2009/pdf/1905.pdf.

3

Metis and STC calibration

This chapter serves to highlight the significance of calibration for space instruments and their embedded detectors applied to the Metis coronagraph and to STC. The calibration activities with their key parameters, importance, and impact on the overall mission are explained in the beginning. The two main calibration steps are then presented: on-ground calibration and simulations. The chapter concludes by describing the in-flight image acquisition process.

This chapter gives an insight into the available means to monitor the instrument performance over time; any deviations or degradation in the instrument's performance can be detected and quantified. This information is crucial to maintaining the accuracy and reliability of the instrument throughout the mission.

Due to the intrinsic problematic of the space environment: while the calibration sources can be freely chosen on-ground on the basis of the requirements to be verified, they are drastically limited for the in-flight calibration. Considering also the limited availability of the mass and volume for the payload, the consequence is the common practice to use just the stars as in-flight calibration sources. This justifies why simulation of star field has been considered and a simulator has been built. The key elements for the simulations are: Star Catalogues, SPICE kernels, Right Ascension (RA) and Declination (Dec) coordinates.

3.1 CALIBRATION

The calibration activities involve conducting measurements and tests throughout the mission to assess and refine the instrument's performance. This is worth for any instrument, but it is even more critical and decisive for Metis and STC. Indeed, they operate in a hostile environment, are subjected to high temperatures, and experience high-temperature variations: the coronagraph and the stereo camera will operate in proximity to the Sun and Mercury, respectively.

Calibrations activities typically include measurements of known calibration sources, calibration targets, and internal reference signals.
Several key parameters are monitored and calibrated during the calibration process. These parameters may include, but are not limited to:

- calibrating the instrument's gain: it ensures accurate conversion of raw measurements into physical units, and helps, with a well-known calibration incoming flux, in determining the instrument's sensitivity to incoming photons; and in optimizing its dynamic range, i.e. the range of incoming photons that can be detected by the instrument.
- characterizing the instrument's spectral response: it is essential for accurate spectral analysis that the instrument captures and records the desired spectral information without significant distortions or biases. This calibration is usually performed by observing a standard source with known spectral features.
- the Point Spread Function (PSF): it describes the spatial response of the instrument, including its resolution and spatial distortion, which is central for accurate image reconstruction and interpretation.

3.1.1 Detector calibration

Detectors are critical components of the instruments and are responsible for converting incoming optical signals into electrical signals for further processing. Calibration of detectors ensures their proper functioning, characterization of their response, and identification of any detector-specific issues or anomalies.
Detector calibration involves assessing and adjusting the detector performance throughout the lifetime of the instrument. This includes monitoring parameters, detailed hereafter, such as: quantum efficiency; dark current; noise characteristics; linearity; and pixel response uniformity. In this case, comparing in-flight measurements of these parameters with on-ground results allows to identify any changes or drifts in detector performance.

QUANTUM EFFICIENCY (QE) CALIBRATION

The QE calibration determines the detector's efficiency in converting incident photons into electrical signals. It is performed by observing calibration sources with known spectral properties and comparing the measured signal with the known flux.

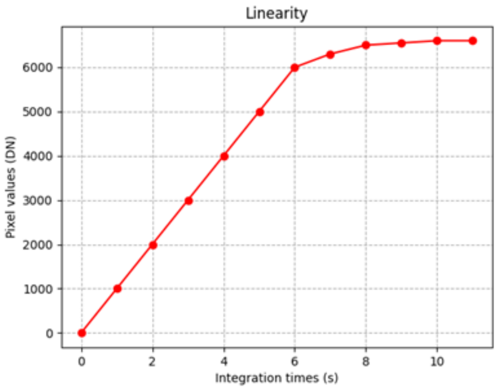

Figure 3.1: An example showing the light of a star captured by the STC detector at various integration times (IT).

The QE calibration allows for an accurate determination of the detected signal's intensity.

DARK CURRENT AND NOISE CHARACTERIZATION

Dark current refers to the signal generated by the detector in the absence of light. It is central to measure and subtract the dark current to obtain accurate measurements. Noise characterization involves quantifying the various sources of noise in the detector, such as readout noise and photon shot noise, to assess their contributions to the overall measurement uncertainty.

PIXEL RESPONSE UNIFORMITY

Pixel-to-pixel variations can lead to inconsistencies in the detector response across different regions. Calibrating and correcting for pixel-to-pixel variations are important to achieve uniform images. This calibration is typically performed by observing calibration sources with known spatial features and comparing the measured response across different pixels.
Uniformity across detector pixels is required to avoid systematic errors or biases in the acquired data. Calibrating the pixel response ensures consistent sensitivity and accuracy across the detector's field of view.

NON-LINEARITY CORRECTION

Detectors often exhibit nonlinear responses, where the output signal deviates from a linear relationship with the input signal. In this case, the electrical output signal is no longer directly proportional to the optical input signal. Linearity calibration can be performed in two ways: by observing, with at a fixed integration time, a source whose intensity can be varied, or by using a source at a fixed intensity and varying the integration time. In both cases, the expected response has a behavior as depicted in figure 3.1.

The comprehensive analysis, both on-ground and in-flight, was conducted by Dr. Michela Uslenghi[1] for Metis. The on-ground studies specifically focused on STC were carried out by Federico Manfredi in [1] and are briefly summarized below. However, a detailed presentation of the in-flight study can be found in Chapter 5.

3.2 On-ground Calibration

The on-ground calibration procedure for the Metis and STC instruments is presented in this section. The outcomes of the on-ground calibration form the basis for chapters 4 and 5, providing critical insights and establishing a solid framework for the analysis and investigation conducted. For the sake of clarity, on-ground calibration procedures and results related exclusively to one instrument between the Metis coronagraph (vignetting, PSF) and STC (Dark, detector anomaly, Field of View) are presented first. Common features such as signal-to-noise ratio and Stray Light are presented downstream.

For Metis, the parameters described in paragraph 3.1 were analyzed using images acquired with a uniform source, a flat field panel, as shown in Figure 3.2 a. These images, known as flat-field images, are used to correct for irregularities in the image sensor's response to incoming light, optical imperfections, dust particles, and vignetting that can cause non-uniform illumination across the image frame.

The next subsection provides a description of the vignetting, and the following one describes the calibration of the PSF.

3.2.1 Metis vignetting

Considering the flat image response for the scientific images calibration allows accurate measurements of the solar corona.

Prior to discussing the analysis of vignetting performed for Metis, it is significant to note that the flat-field panel used is called Spike-A flat fielder. This panel consists of a LED matrix with multiple layers of diffusing material. The panel was powered at 9 V to prove a quasi-uniform illumination (at 99%), since using a lower

---

[1] INAF-Istituto di Astrofisica Spaziale e Fisica Cosmica, Via Alfonso Corti 12, 20133, Milano, Italy. ORCID: 0000-0002-7585-8605

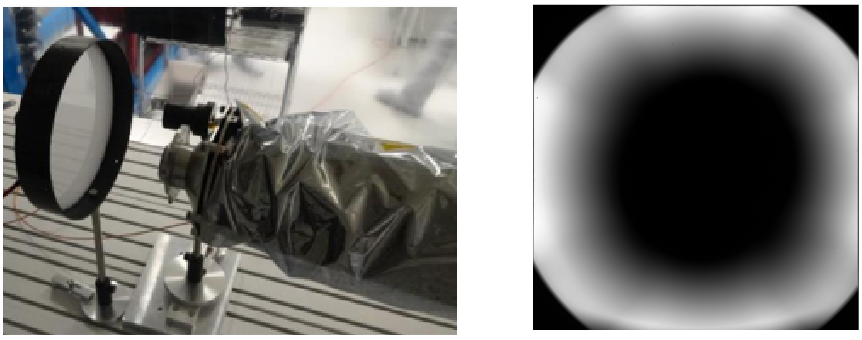
(a) **(b)**

Figure 3.2: (a) The laboratory radiometric calibration test set-up for Metis. (b) Flat-field image acquired with an IT=4s [2].

voltage could result in brightness variations. To ensure accurate results, the flat field panel should be positioned perpendicular to the telescope's optical axis.
The acquisitions made with this Spike-A flat fielder in the configuration shown in 3.2 a show the optical phenomenon known as vignetting. Vignetting refers to the reduction in brightness caused by the interaction of light with elements within the telescope. In Figure 3.2 b, several factors contribute to this reduction: the internal occulter, which blocks photospheric light (resulting in the black center); the spiders of the IO and LS; and the FS, responsible for the black corner.
One of the significant acquisitions made during the on-ground calibration, then used for comparison with in-flight data, involves an image of the flat field captured with an integration time (IT) of 4s. This image was studied along various radial profiles, as shown in Figure 3.3 a and b. Profiles were taken at specific angles: 0°-180° (blue), 45°-225° (red), 90°-270° (yellow), and 135°-315° (green). Theoretical vignetting functions were calculated using raytracing software (Zemax) and compared with the measured profiles. The measured profiles (different colors) were overlapped with the black Zemax profiles. All curves were normalized to the maximum measured value in the radial direction of 270°. These plots also demonstrate that the slope of the measured vignetting curve is in accordance with the theoretical one. More detailed information is available in the article [3].
The analysis of the flat-field images and the vignetting are replicated in-flight and are described in the chapter 5.

3.2.2 Metis PSF

To study the Point Spread Function (PSF) in Metis, a pinhole mask (with 5 pinholes of 200 µm diameter each) placed in the focal plane of a collimator was used. This mask was illuminated with an Adjustable Power LED (APL). The ratio of

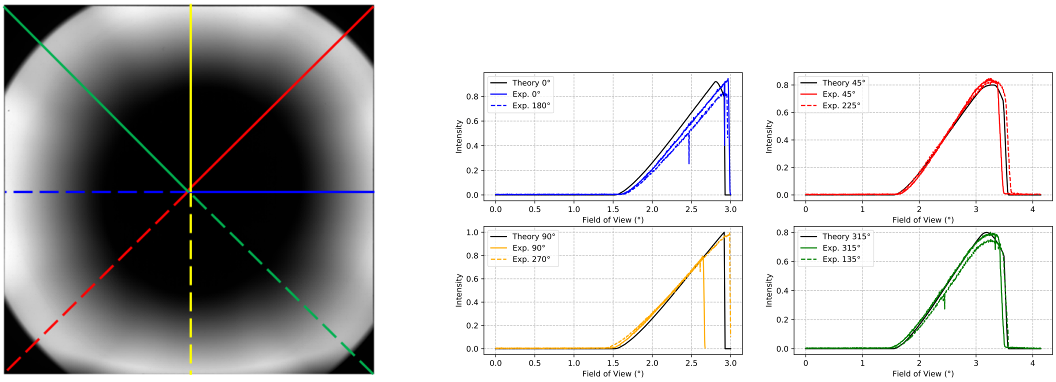

(a) **(b)**

Figure 3.3: Image acquired with an IT=4s with the lines in the corresponding radial profiles. (b) Radial profiles for angles: 0°- 180° (in blue); 45°- 225° (in red); 90°-270° (in yellow); 135°-315° (in green) [3].

the focal length of the SPOCC[2] collimator (2030 mm) to the focal length of the VL channel (204 mm) is equal to 10. In an ideal scenario, this configuration in Metis would result in the production of five 'point-like' images on the visible focal plane, each with a size of 20 microns.

To obtain the Point Spread Function (PSF), assuming that the pinhole image follows a normal distribution, we performed a Gaussian fit. Since the sources are not point-like, to obtain their corresponding PSFs, deconvolution is necessary using a rectangular function that is non-zero only for the pixels occupied by the theoretical kernel size. If we denote the Gaussian function obtained from the fit of the pinhole images as f(r) and the rectangular function as k(r), we can obtain the PSF, $\mathscr{P}$, of the system using the Fourier transform:

$$\mathscr{P}(r) = \mathscr{F}^{-1}\left(\frac{\mathscr{F}(f)}{\mathscr{F}(k)}\right) \tag{3.1}$$

where $\mathscr{F}$ stands for the Fourier transform operator.

Additionally, we assume the standard deviations σ_x and σ_y (along the x and y directions, respectively) of the obtained PSF as indicative values of the system's resolution.

To convert the obtained PSF in microns into arcseconds, we use the factor scale described in table 2.2. In Figure 3.4, an image with an inset (zoom-in) is shown, which was acquired with an off-pointing angle of 2.8°. The inset displays two boxes: a smaller magenta box and a larger yellow box. The yellow box represents 2.58

---

[2] Sun simulator described in details in [2]

times the standard deviation (99% of the signal assuming a Gaussian distribution of the pinhole light). As written at the beginning of this chapter, compliance with the requirements (reported in [4]) is essential; the PSF at 2.8° is then calculated considering how much light is inside the magenta box, 25x25 μm in size. The ratio between the two boxes gives the value of the Ensquared Energy (EE) which is 88%, surpassing the minimum requirement of 80%, and represents the focus of the VL channel.
I also conducted a similar analysis for the UV channel in a previous work ([2]). Indeed, my current PhD research does not involve UV analysis for in-flight calibration. Regarding the study of the UV channel, an upcoming article by De Leo et al. is in preparation [5].

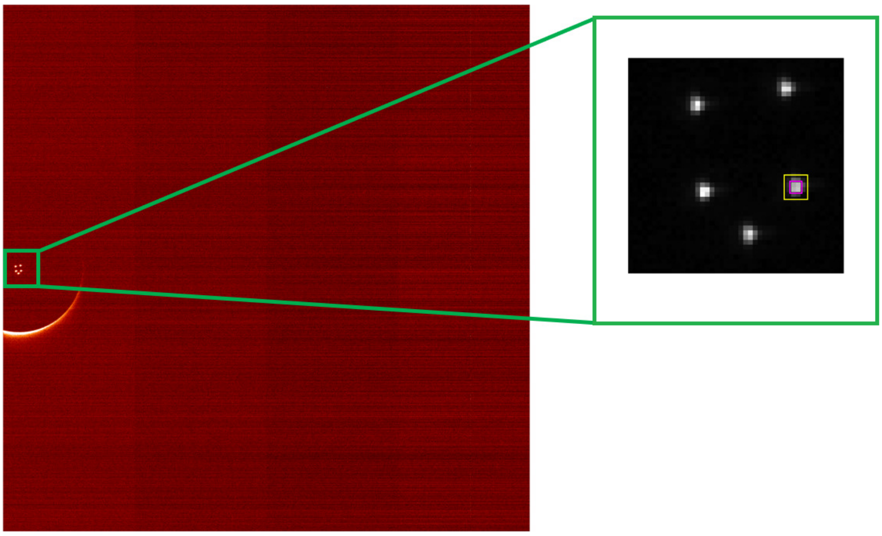

Figure 3.4: Image of the pinhole mask, with the 5 pinholes in inset, illuminated by the APL with an off-pointing of 2.8°. The ratio between the magenta and the yellow box give the information of the Ensquared Energy (EE) to compare with the requirements (in this case: 88%, required: 80%; the system is then focused) [2].

The in-flight study of the PSF has been expanded and replicated with in-flight calibrations and is described in the next chapter.

3.2.3 STC Dark

Dark current characterization serves as a foundation for image reduction. When an astronomical image is taken, the sensor of the camera or telescope introduces unwanted signal, commonly known as dark current, which can present fluctuations

from one pixel to the other. These fluctuations can manifest as pixel signal-level variations and appear as specks or streaks in the final image. To counteract this, a dark field image is captured with the same exposure settings as the astronomical image, but with the light source blocked. This image records only the dark current, allowing for its subsequent subtraction from the astronomical image, effectively reducing unwanted signal artifacts.
The dark analysis on STC revealed unexpected phenomena in the detector behavior that were not correlated with dark or light signals. These effects were identified by acquiring sequences of images. Figure 3.5 presents two examples where the measured mean value of the dark image (in units of digital number (DN)) is plotted against the sequential acquisition number or IT (upper abscissa).
The set of 15 images was taken under dark conditions at the nominal detector temperature of 268 K. Each set of 15 images has the same integration time (IT) and a constant readout time of 0.7 s. The IT increases from one set to the next. As these images were acquired without illumination, they should primarily be affected by Dark Current (DC) and Fixed Pattern Noise (FPN). Since the IT is limited to a few milliseconds, the contribution of DC should be negligible. However, a spurious signal of several thousand DN is evident, which stabilizes within each set of pictures (as seen in the higher IT).
From these graphs two distinct spurious effects are present: the Pedestal Effect (PE) and the Peak Offset (PO). The first manifests itself as a steep increase in the background signal, not related to DC. Unlike DC, which is linear with integration time due to thermal energy-induced electron transitions in the conduction band, background growth (PE) exhibits a steeper, saturation-like behavior. The second effect is observed as an offset in the DN values of the pixel in the first image of each set. However, it decreases with each subsequent image acquired within the same set (with the same integration time), eventually converging to the Pedestal level. The appearance of this effect seems to be related to a certain elapsed time between two images [6].

This phenomenon has also been observed during in-flight acquisition and will be discussed in detail in the chapter 5.

3.2.4 STC detector anomaly

During the analysis performed on the STC detector, an anomaly in the form of a bright dot was detected, as illustrated in Figure 3.6 (little white box). The details of this anomaly can be found in the Master thesis written by Federico Manfredi [1], which provides a comprehensive summary of the on-ground investigation.

The occurrence of the bright spot phenomenon extends beyond a small area near

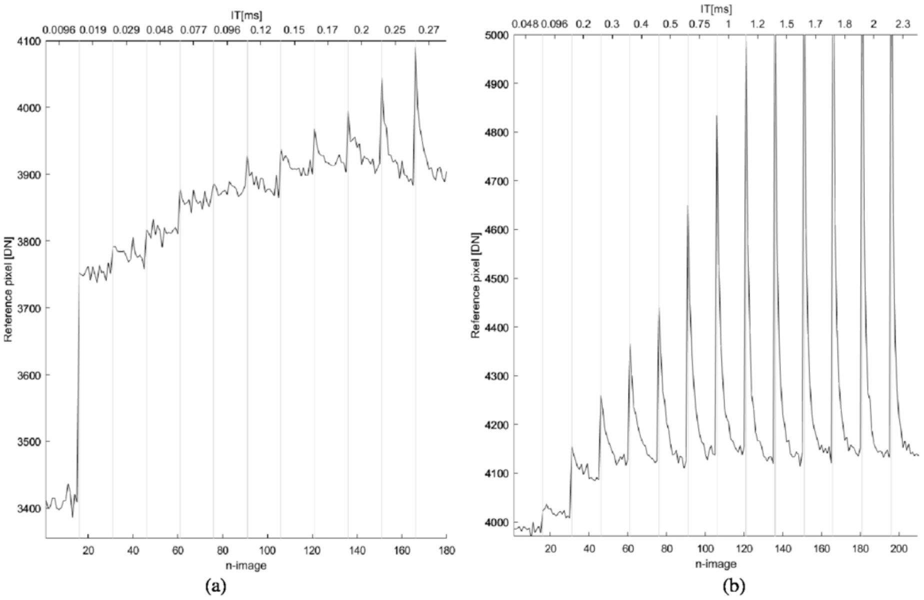

Figure 3.5: (a) The graph displays the signal captured on the reference pixel for a series of image sets acquired with gradually increasing IT. It shows the measured pixel values for 180 images divided into 12 sets, ranging from 0.0048 ms to 0.27 ms, indicated on the upper X-axis. (b) Pixel values for 210 images divided into 14 sets, acquired with longer integration times (up to 2.3 ms). These sequences were obtained at a detector temperature of 268 K. [6].

the hot pixel, affecting the entire surface of the sensor. However, the impact gradually diminishes as one moves away from the center of the spot. This observation suggests the existence of a relationship between the bright spot and the distance from the center of the spot.
Furthermore, the phenomenon appears to be more pronounced at shorter integration times (IT). However, as the integration time approaches 200ms, the phenomenon becomes less significant or even negligible.

3.2.5 STC Field of View (FoV)

The uniform source for the on-ground calibration for STC was an integrating sphere, which setup configuration picture and scheme are shown respectively in 3.7 a and b. The USS-2000-C integrating sphere features a quartz tungsten halogen lamp (QTH) as light source, and it is a product from Labsphere.
The difference with Metis is that STC has no foreseen vignetting elements along the optical path, so there is less vignetting. However, it must be checked that the vignetting introduced by the baffles vanes remains within the limits of the

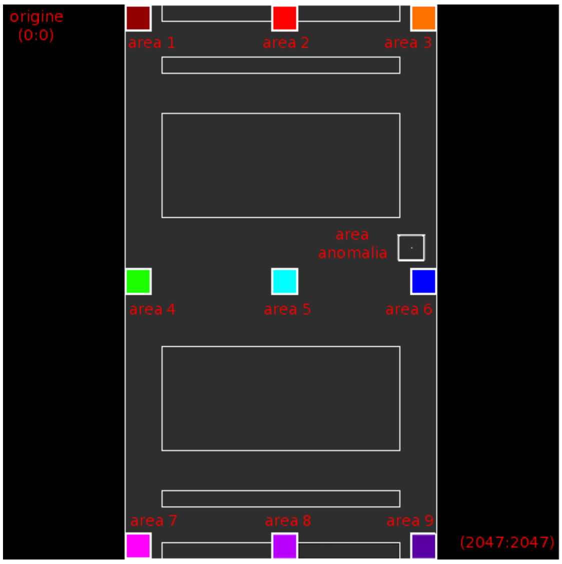

Figure 3.6: The STC detector exhibits a bright dot anomaly. The white rectangles indicate the positions of the panchromatic and filter elements, while the colored squares represent the areas where the analysis was conducted [1].

requirements. The integration sphere has been used for the study of the FoV, which is another task that must be replicated during in-flight calibration.

During the on-ground calibration, the lamp light was moved along the baffle edge to investigate the vignetting, a schematic representation is shown in figure 3.8, where the yellow line indicates the path taken by the lamp image. This specific location holds significance as it represents where the Field of View (FOV) of the instrument is ”limited” by the baffles.

The results of the vignetting analysis at the edges of the FOV, specifically for the filter f920, the pan L, pan H, and the f750, are displayed in Figure 3.1, respectively.

3.2.6 Stray Light

Another parameter determined on-ground is the Stray light, the parasite light that can contaminate the observed signals and lead to inaccuracies. Therefore, the Stray Light Calibration aims to identify and quantify the impact of unwanted light on the instrument’s measurements. Given their respective scientific purposes, this calibration is more important for the Metis coronagraph than it is for STC. Such an on-ground calibration is then completed with simulation and by a renewed in-flight calibration. The logic inherent to such calibration relies on observing dark

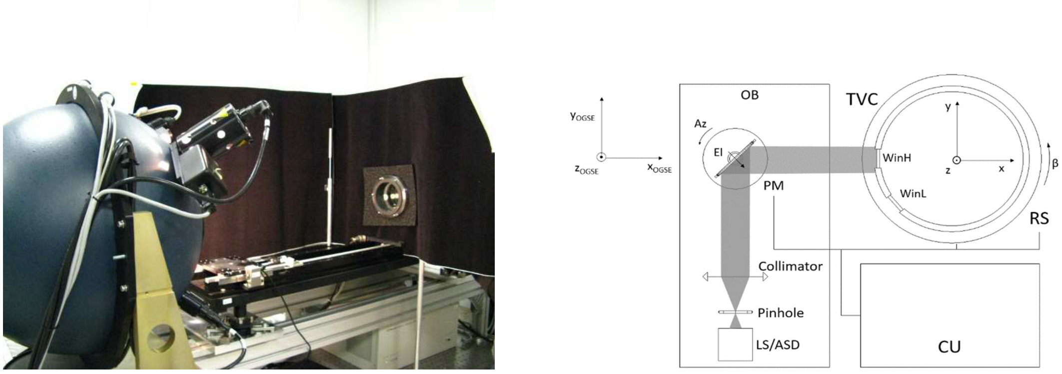

(a) **(b)**

Figure 3.7: (a) The laboratory calibration test setup showcases the optical layout of STC and the integrating sphere, courtesy of Leonardo SpA (Campi Bisenzio (FI) - Italy). (b) The OGSE (Optical Ground Support Equipment) is represented schematically. The exit port of the the integrating sphere (IS) is placed in the focal plane of a collimator. A Plane Mirror (PM) redirects the collimated light beam towards the Thermal Vacuum Chamber (TVC), which is situated on a Rotational Stage (RS). The RS can rotate vertically, and the rotational angle is denoted by β. In order to enter the TVC and reach the STC instrument housed inside, the light passes through a window (WinH/WinL). The orientations of the PM and RS are controlled by the Control Unit (CU) [7].

or low-intensity regions of the sky to assess the level of stray light contamination. In Metis this calibration has been performed by F. Landini and is described in the articles [8] and [9], for the on-ground with simulations, and in [10] for the in-flight. For STC the stray light has less impact, but it is significant that its amount is less than the requirements for the instrument.
These experimental results of the on-ground calibrations are recorded in order to be compared, during the mission, with the data acquired in-flight. On-ground calibration is also completed by simulations, which are presented in the next section.

3.3 Simulations

Simulations play a central role in the development and testing of space instruments for several reasons: performance evaluation, design optimization, cost and time efficiency, environmental and operational challenges, and calibration and data analysis. Focusing on the latter, the simulations are valuable for calibrating space instruments and understanding their data. Therefore, the simulations are the ”bridge” between the two main steps of the calibration process: on-ground and

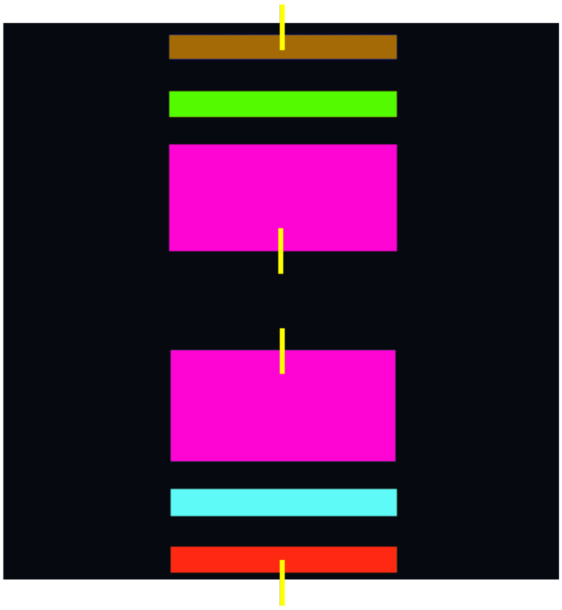

Figure 3.8: Schematic representation of the study of the FoV. The coloured rectangles represent F920, F550, PAN L, PANH, F420, F750, respectively. The yellow line indicates the path taken by the lamp. Courtesy of Vania Da Deppo.

in-flight calibration.

The software used for optical simulation, Zemax, facilitated the comparison of on-ground results (as described in section 3.2.1) and the subsequent in-flight calibration results.
The following subsection presents simulations conducted to analyze the signal-to-noise ratio (SNR) for Metis and STC, and the main parameters used for the simulations aiming to predict where the stars will be. These simulations are complementary to the on-ground calibration results that have been previously introduced. In upstream of in-flight calibration, simulation methods and tools related to the light sources of interest for Metis and STC are presented afterwards.

3.3.1 Metis and STC signal to noise ratio (SNR)

The simulations performed by De Leo, in [11] for Metis, and Slemer et al., in [7] for STC, aimed to identify the minimum signal-to-noise ratio (SNR) required for accurate detection of the stars and determination of the center of gravity.
Particular attention should be paid to the case of Metis, where the signal is a combination of the solar corona and the point source (star). As described in chapter 1, the corona is not static, so in the simulation the presence of streamers

Table 3.1: The vignetting results for the f920 (a), pan L (b), pan H (c), and f750 (d) at the edges of the Field of View (FoV). Courtesy of Vania da Deppo.

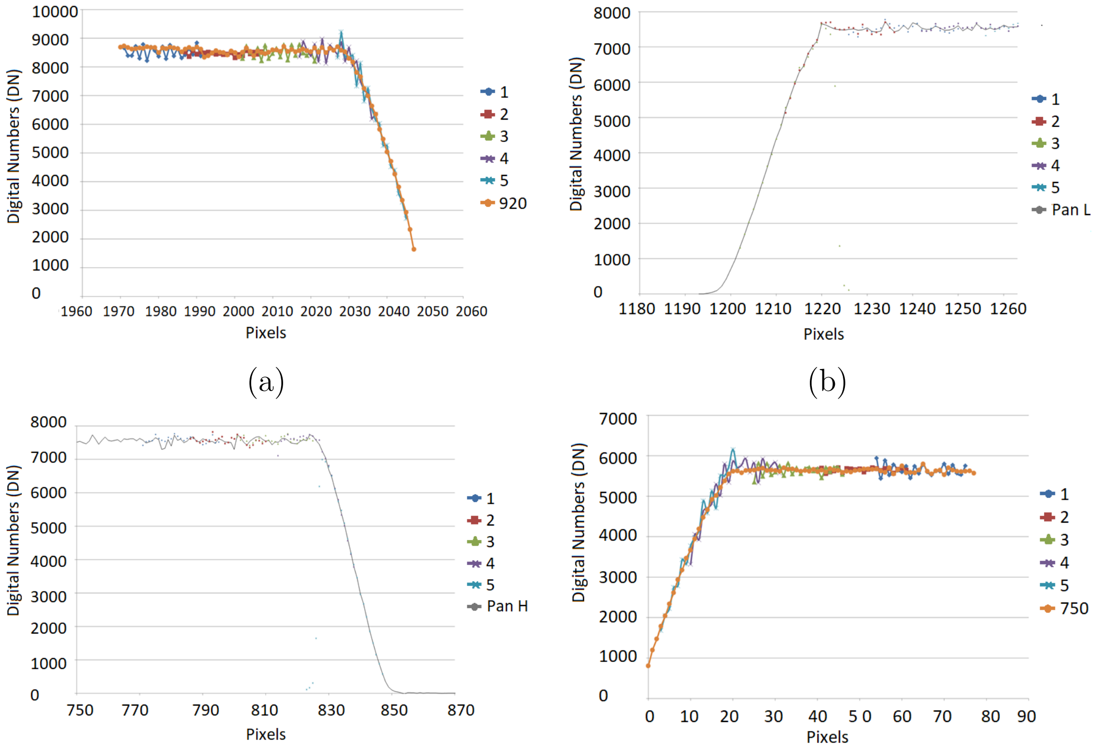

(a) (b)

(c) (d)

or coronal holes has also been included.

For STC there is not this problem, so the simulation was performed generating several images with varying SNR levels, using a single spot to represent a star. The retrieved centroid position is compared to the nominal value, while considering the optical transmittance properties of the STC instrument.
Their simulations indicated that the optimal SNR values lie within the apparent magnitude range [0, 7] for Metis and [0, 9] for STC. To illustrate this, they created the plots shown in Figure 3.9 a and 3.9 b. The plots help to explain the visual magnitude limit imposed.
The STC case is straightforward: once all the instrument elements have been included, the signal-to-noise ratio (SNR) is expressed as a function of the integration time (IT) for stars with different apparent magnitudes.
For Metis, the simulation represents the countrate of the stars with different mag-

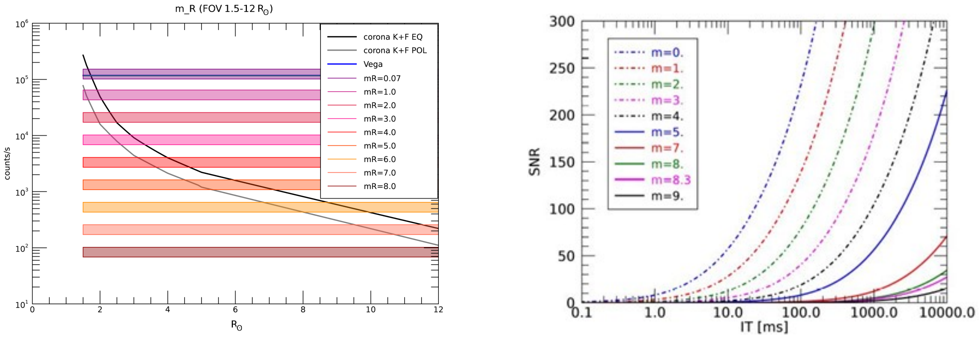

(a) **(b)**

Figure 3.9: (a) Countrate of Metis at different solar radii for different stars magnitude [11]. (b) The signal-to-noise ratio (SNR) for STC expressed as a function of the integration time (IT) for stars with different apparent magnitudes [7].

nitudes and the coronal light can come either from the equator or from the pole. The latter are respectively represented with the black and dark gray lines; the colored bands represent different light from stars with different magnitudes. The intersection between the coronal light and the band gives the lower limit from which a star can be detected by Metis.

In the next section, the upstream role of simulation for in-flight calibration is highlighted.

In the following, the key elements of the analysis and the main parameters used for the simulations are defined. To determine the stars that will enter the field of view of the instruments, the star catalogue and the SPICE kernels are used, and are described in detail.

3.3.2 Light sources of interest (stars of interest)

A bibliographic research has been conducted on star catalogues selection, celestial coordinates, and the SPICE kernels, which stands for Spacecraft, Planet, Instrument, Camera pointing, and Events. A summary of this work is presented below.

STAR CATALOGUE

Numerous stellar catalogues are available online with more than twenty options. To focus on the objective, two European catalogues have been selected: SIMBAD, managed by the *Centre de Données Astronomiques de Strasbourg*; and GAIA, which utilizes data from the Gaia space telescope of the European Space Agency (ESA).

SIMBAD provides basic data for each stellar object, including: object types; co-

ordinates; proper motion; and radial velocities. It also offers cross-identifications with more than 12,000 source catalogues and tables, as well as observational data and a general bibliography for each object. GAIA, like SIMBAD, utilizes a cross-match protocol with other catalogues such as Hipparcos-2 and Tycho-2.
Both catalogues provide consistent values for the position, proper motion, and flux errors.
The discriminating factors between these two catalogues are the inclusion of bright stars and the possibility to work offline. Indeed, such stars are included in SIMBAD, whereas they are not in GAIA. Besides, the information of the stars can be easily downloaded in SIMBAD, but not in GAIA. Therefore, we have chosen the SIMBAD catalogue.

RIGHT ASCENSION, DECLINATION

Stars in the catalogue are displayed based on their position on the celestial sphere defined by the coordinates Right Ascension (RA) and Declination (DEC). Declination is measured in degrees North and South of the celestial equator, similar to terrestrial latitude. The celestial equator is at 0° DEC, while the poles are at +90° and -90°.
Right ascension, similar to terrestrial longitude, is measured east from the equinox. RA can be expressed in degrees, but is commonly specified in hours, minutes, and seconds. One hour of RA corresponds to 15° of sky rotation. SIMBAD catalogue uses RA in degrees.

SPICE KERNELS

The SPICE kernels are datasets that contain precise navigation information and various additional details. They offer accurate observational geometric data used by both the planetary science and engineering communities. [12].
In SPICE kernels, time is given in ephemerid, and the UTC (Universal Coordinated Time) can be converted to ephemerid using the command spice.utc2et. Each spacecraft typically has multiple instruments, and each instrument can have multiple channels. Specific word codes are used to determine the reference vector (boresight) of a particular detector. For example, the code $'MPO\_SIMBIO-SYS\_STC-H\_P700'$ represents the boresight of the panchromatic, in the sub-channel H, of the channel STC of SIMBIO-SYS inside the spacecraft MPO.

3.4 In-flight Calibration

This section explains the importance of in-flight calibration and how images for in-flight calibration are acquired.

In-flight calibration is of paramount importance as it validates the calibration performed on the ground and accounts for the actual operational conditions encountered during space missions. By comparing the in-flight calibration results with the on-ground calibration and simulations, several significant aspects can be addressed as: environmental effect; instrument degradation; refinement of calibration models, and validation of science results. Indeed, consistency between the two sets of results boosts confidence in the scientific data and enhances the credibility of the mission's scientific findings. We recall that accurate calibration enables precise measurements of physical properties, enhances the interpretation of scientific results, and supports scientific investigations, such as identifying solar or geological features, measures the speed of the particle after a solar eruption, studying surface morphology, and detecting variations (during the solar activity or of the composition of Mercury).
While on-ground, the acquisitions have been made acquiring images at different IT of a well-known source, in-flight calibration activities involve, mainly, the acquisition of the light coming from stars. Some stars are well known and have the name of calibration stars.
The stars can be used for characterizing and correcting for nonlinearities to ensure accurate measurements across the detector's dynamic range, and also to the transit, referring to the movement of a star across the detector, which occurs over a span of several minutes. It is crucial to perform repeated observations of stars at various times during the instrument lifetime to monitor changes in instrument sensitivity caused by factors such as changes in optical elements, detector degradation, and other sources. In the case of Metis and STC, which operate in extreme environments near the Sun and Mercury, systematic observations of multiple stars allow tracking of sensitivity variations. Comparing the in-flight and on-ground results provides valuable insights into the instrument status and performance, and represents the core of the next chapter.
In the following, it is reported how the images for the calibration for Metis and STC are acquired.
For Metis the images important for the in-flight calibration, the dark UV and the bias (VL and UV), are acquired at the beginning of the STP, in particular the image of the VL bias. They are acquired close to the opening or closing of the door. The bias UV can be acquired instead when the door is open. For convenience, both bias images are acquired with the door closed because there is no scientific acquisition.

As far as acquisitions of the image with the stars are concerned, the stages are the following:

- at the beginning the ephemerid of the start is studied; then they are compared with the FoV of Metis (the stars to be seen), usually this happens 6 months before the acquisition.
- A new check is made around 15-20 days before the acquisition to see
  - if these stars are effectively in the FoV.
  - if the solar irradiance is still equivalent as expected. In that case, the integration time (IT) needs to be changed. So far, on three years of missions, this had to be done just twice.

As far as STC is concerned, only the dark acquisitions are taken because the MPO is embedded with the MMO so it is possible to just take dark acquisitions. After the separation, STC will acquire the stars to study the mapping optical distortions. It requires stellar fields with well-distributed objects across STC field of view (FoV), particularly in the panchromatic. To prepare for this operation, the stellar field database using the SIMBAD star catalog, introduced in 3.3.2, is made and presented in the next chapter. The observations of stellar fields serve the following purposes: PSF verification; optical path verification angle; optical axis pointing direction; and image distortion verification. Detector parameters like FPN, readout noise, linearity, and dark current will also be verified. Radiometric calibration entails observing a bright spectrophotometric standard star. These in-flight calibrations are to be repeated twice during each orbit of the planet around the Sun [13].

This chapter has outlined various essential elements that play a pivotal role in elucidating the results obtained and their corresponding descriptions in subsequent chapters 4 and 5.

After providing information on the importance of the parameters for the calibration, the analysis performed for the on-ground, the considerations necessary for simulating stars within the Metis and STC channels, this chapter presented the procedure for in-flight calibration. In the next chapters 4 and 5 the results of the simulations, of the in-flight calibration and its comparison with the on-ground calibration, and of the image analysis performed for Metis and STC are presented.

References

[1] F. Manfredi. *Analisi delle prestazioni del sensore di STC, stereo camera progettata in ambito della missione BepiColombo.*

[2] C. Casini. *Calibrazione del coronografo spaziale Metis della missione Solar Orbiter.* 2018. URL: https://www.researchgate.net/publication/328998046_Calibration_of_the_spatial_coronagraph_Metis_on_board_Solar_Orbiter.

[3] C. Casini et al. "On-ground flat-field calibration of the Metis coronagraph onboard the Solar Orbiter ESA mission". In: *International Conference on Space Optics — ICSO 2020.* June 11, 2021, p. 190. DOI: 10.1117/12.2599945.

[4] G. Nicolini. *METIS Technical Specification.* Tech. rep. OATO.

[5] Y. De Leo et al. "In-flight radiometric calibration of the Metis UV H I Ly-α channel and comparison with UVCS." In preparation. 2024.

[6] E. Simioni et al. "CMOS detectors: lessons learned during the STC stereo channel preflight calibration". In: *International Conference on Space Optics — ICSO 2016.* Sept. 25, 2017, p. 148. DOI: 10.1117/12.2296147.

[7] A. Slemer et al. "Radiometric calibration of the SIMBIO-SYS STereo imaging Channel". In: *CEAS Space Journal* 11.4 (Dec. 2019), pp. 485–496. DOI: 10.1007/s12567-019-00277-5.

[8] F. Landini et al. "Stray light calibration for the Solar Orbiter/Metis solar coronagraph". In: *International Conference on Space Optics — ICSO 2018.* July 12, 2019, p. 89. DOI: 10.1117/12.2536009.

[9] P. Sandri et al. "Stray-light analyses of the multielement telescope for imaging and spectroscopy coronagraph on Solar Orbiter". In: *Optical Engineering* 57.1 (Jan. 25, 2018), p. 1. DOI: 10.1117/1.OE.57.1.015108.

[10] F. Landini et al. "In flight stray light reduction for the Solar Orbiter/Metis coronagraph". In: (). DOI: 10.1117/12.2536009.

[11] Y. De Leo. *Sviluppo di strumenti per la calibrazione, la pianificazione delle operazioni e l'analisi dati del coronografo Metis su Solar Orbiter.* 2019. URL: https://www.researchgate.net/publication/373947346_Master_Thesis_Yara_De_Leo.

[12] C. H. Acton. "Ancillary data services of NASA's Navigation and Ancillary Information Facility". In: *Planetary and Space Science* 44.1 (Jan. 1996), pp. 65–70. DOI: 10.1016/0032-0633(95)00107-7.

[13] L. Tommasi. *SIMBIO-SYS FM User Manual.* Copyright Leonardo S.p.a. All Rights Reserved. 2018.

4

Optical performance validation and radiometric models

In this chapter, the presented topics will follow a chronological sequence, focused on the methodology employed for star analysis, regardless of its application on Metis or STC. This chapter begins with the outcomes derived from simulations involving stars visible to STC. Subsequently, the discussion will shift towards the PSF analysis of stars within the Metis observational range.

4.1 Stars simulation

Aiming for the validation of the optical performance, in this section all the elements described in the previous chapter in the sections 3.3.1 are summarized and 3.3.2: the star catalogue, the definition of the right ascension and declination, the spice kernels, and the SNR. These elements enable to know first where the stars do locate in the celestial sphere, and then how and when some of them are in the FoV of some instrument.

4.1.1 Stars in the celestial sphere

As mentioned in chapter 3, since a uniform light source is not accessible in space, we rely on the illumination provided by the stars.
Therefore, we extract a list of stars with the desired magnitude (0-9 for STC and 0-7 for Metis) from the SIMBAD catalogue. We also obtain the angular dimensions, in RA and DEC, of the panchromatic filters. Using Python, we have developed a code that accounts for the rectangular shape of the panchromatic on the celestial sphere. The outcome is illustrated in Figure 4.1, which represents the number

of stars visible in various sections of the celestial sphere using false colors. The colorbar indicates the star count within STC's field of view, ranging from no stars (dark blue) to the maximum number of detected stars (dark red).
As expected, STC observes a greater concentration of stars along the galactic plane and significantly fewer stars near the poles. When representing these results, it is crucial to acknowledge that we are projecting a sphere onto a rectangular plane, akin to how the Earth is depicted on a map (planisphere). Therefore, additional calculations are required to account for this transformation. This discrepancy in representation explains the larger rectangular shapes of the detector while observing towards the poles.

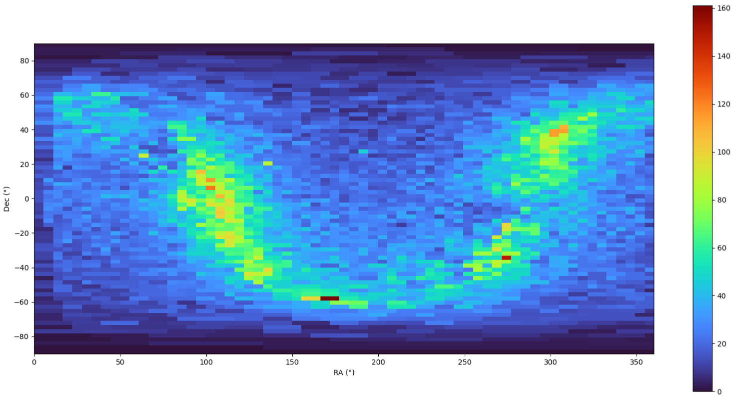

Figure 4.1: The celestial sphere reveals stars captured within the field of view (FoV) of STC's panchromatic view. The colorbar in the visualization indicates the star count within the FoV, ranging from no stars (dark blue) to the maximum number of detected stars (dark red).

Since the two panchromatic channels have a spatial separation of 42.75°, we have developed a program to ascertain the count of stars visible in both the panchromatic H and L channels simultaneously. To accomplish this, we have devised a similar program that identifies simultaneously where the pan H channel detects more than 60 stars [1, 2]. The results are presented in Figure 4.2, where the circles' sizes correspond to the number of stars present within the panchromatic view.
This study allows us to plan the acquisition of the stars in order to optimize the time dedicated to the acquisition of images for calibration.

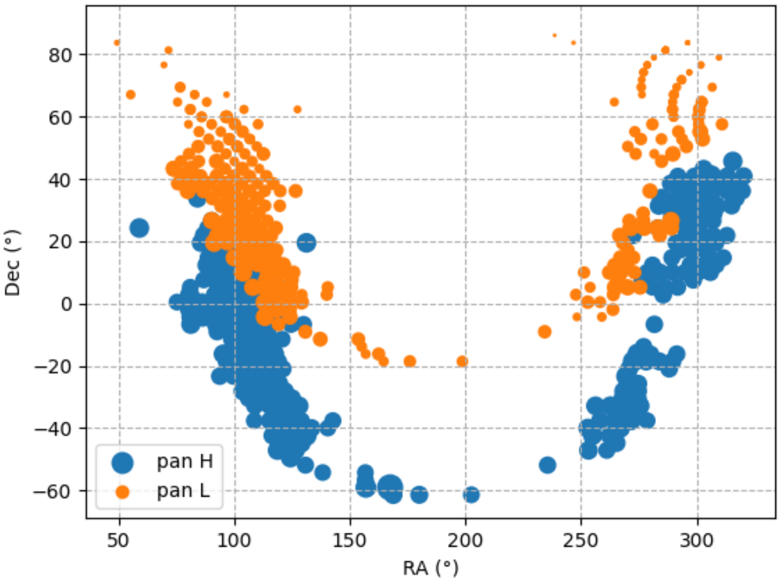

Figure 4.2: Simultaneous detection of the stars where the pan H channel identifies over 60 stars, blue circle, and the corresponding stars visible in the Pan L channel, orange circle. The size of the circle represents the number of stars inside the FoV

4.1.2 Stars in the FoV

We have developed a ”boresight” program that utilizes the SPICE kernels to determine the location of the detector uploading the files ”solo_ANC_soc-pred-mk_v110_20230620_001.tm” for Metis and ”bc_ops_v410_20230626_002.tm” for STC. This program allows us to select the FoV of interest. By utilizing the SPICE kernels, we obtain the boresight of the selected channel, corrected for stellar aberration. The program then converts the time from UTC to ephemerid time, enabling us to determine the spacecraft's position in terms of right ascension, declination, and roll. To highlight the distinct observational fields of both instruments, the simulations were executed on March 10, 2026, at 8:58:05. This intentional synchronization underscores the divergence in the stars observed by each individual channel, resulting in varying outcomes.

In Figure 4.3 (a) and (b), the stars captured within the FoV of the two panchromatic channels of STC on March 10, 2026, at 8:58:05 are presented: Pan L detects 24 stars, while Pan H detects 29 stars. As written before, this discrepancy arises because they are observing two regions with a separation of 42.75°.

Figure 4.4 presents the stars observed by the Metis coronagraph, specifically the visible channel (VL) in (a) and the ultraviolet channel (UV) in (b). Within the

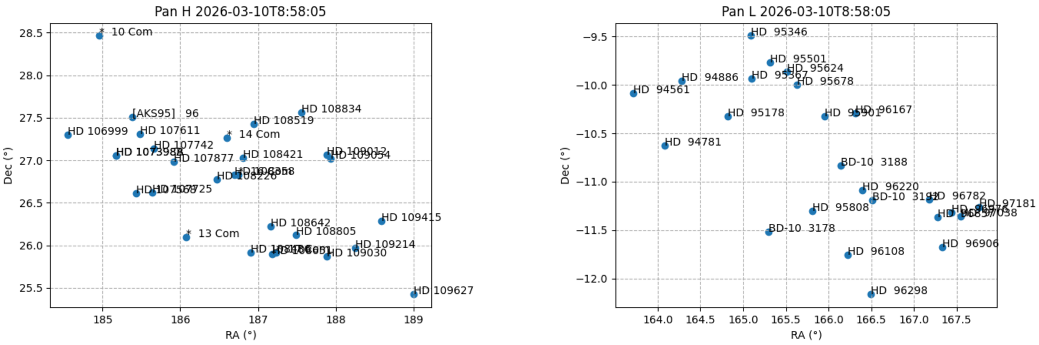

(a) **(b)**

Figure 4.3: Stars visible in the STC Fov on March 10, 2026 at 8:58:05 (a) PanH. (b) PanL.

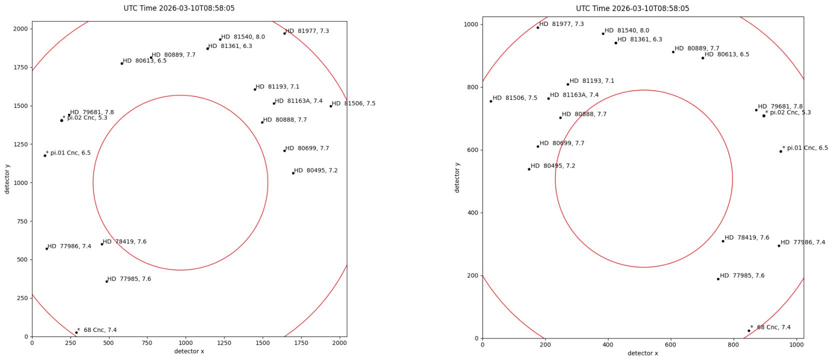

(a) **(b)**

Figure 4.4: Stars visible in the Metis Fov on March 10, 2026 at 8:58:05 (a) Visible. (b) Ultraviolet.

Field of View, a total of 18 stars are visible. Despite Metis captures data in two channels, the optical path inputs coming from the same celestial objects are parallel. The resulting images appear to be mirrored due to the internal reflections within the elements of the coronagraph.

The subsequent section presents the analyses conducted using the stars acquired by Metis.

4.2 Metis PSF

The analysis of the Point Spread Function (PSF) of the Metis instrument was carried out on-ground, and presented in 3.2.2, to ensure compliance with requirements reported in [3]. However, it is critical to assess the PSF performance after the instrument is launched.

The first step consists of finding the visible stars in the FoV of Metis. The images considered for the present analysis were captured during the passage of the comet Leonard in the Metis FoV on December 15th and 16th, 2021 when several calibration stars were within the FoV of Metis.

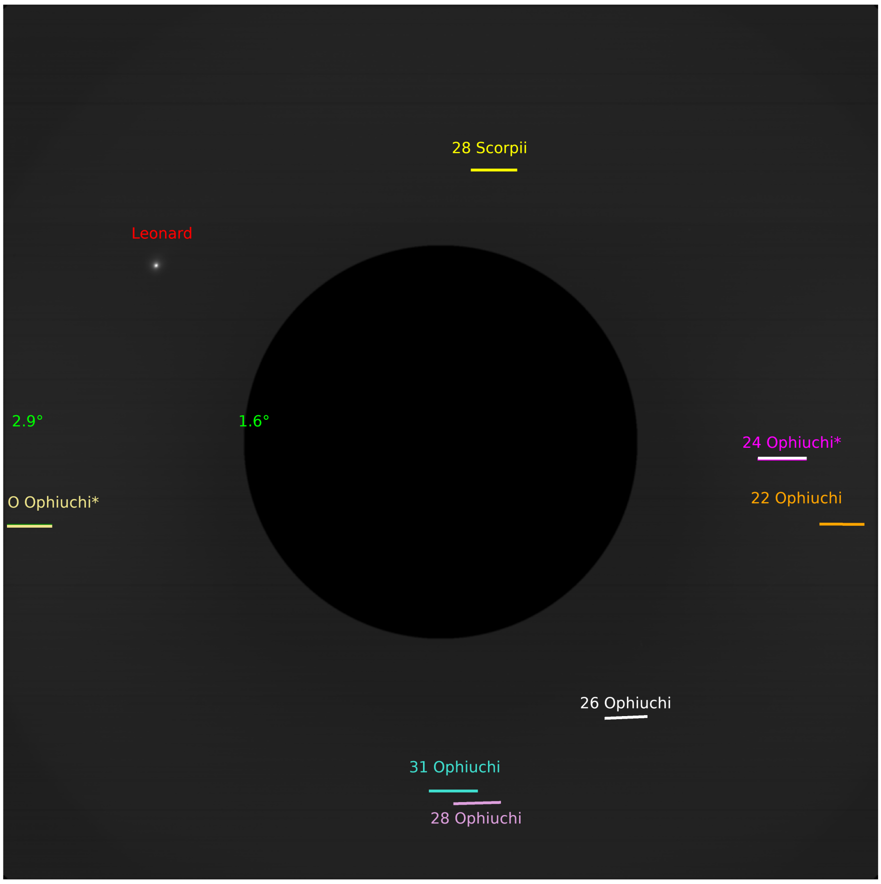

Figure 4.5: The comet Leonard, the calibration stars and the location of the stars on the detector. In green is presented the FoV of Metis.

The images taken into account were acquired with an integration time of 15 s each. In the Figures 4.5: the colored lines represent the trajectory of the stars during these 12 hours of observation; the comet Leonard is represented (named in red); and the FoV of Metis, which is between 1.6° and 2.9°, is written in green. These values are extremely important because, on the basis of the angle in the FoV, the characteristics in terms of collected signal differ. In order to identify stars in the images, our approach involves setting an upper limit by calculating the mean value plus three times the standard deviation. Any pixel value above this threshold is considered a star candidate. This candidate is confronted to the SIMBAD database to establish whether it is a star or not. Subsequently, we define a square region around the pixel with the maximum value, typically with dimensions of 10 pixels by 10 pixels. Within this region, we perform a two-dimensional Gaussian fit.

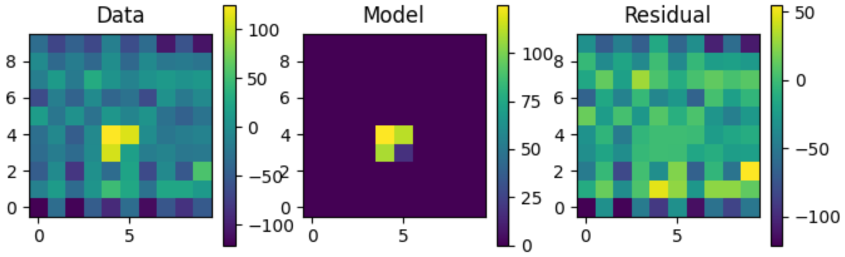

Figure 4.6: 2D Gaussian profile: the Data represents Omicron Ophiuchi* A, the Model represents a simulated 2D Gaussian profile, and the Residual depicts the difference between the measured and simulated profiles helping evaluate the accuracy of the program.

To evaluate the PSF, we determined the standard deviation values σ_x and σ_y extrapolated from the two-dimensional Gaussian fit for each star.

Figure 4.6 presents an example of a two-dimensional Gaussian profile compared to a real acquisition: the ”Data” represents the observed stars in the image; the ”Model” represents a simulated two-dimensional Gaussian profile based on the extracted parameters, performed with Python; and the ”Residual” illustrates the difference between the measured and simulated profiles. Examining the residual helps assess the accuracy of the program in reproducing the observed data.
As part of our analysis, in order to properly express σ, we first converted the requirements from micrometers (μm) to arcseconds: by first converting μm to pixels, using the conversion factors provided in Table 2.2; these pixels are further converted to arcseconds using a platescale of 10.126 on the x-axis and 10.139 on the y-axis. Since our results were initially in pixels, we changed the units in arcsec after the conversion process.

Pol	**1**		**2**		**3**		**4**	
(arcsec)	σ_x	σ_y	σ_x	σ_y	σ_x	σ_y	σ_x	σ_y
26 Ophiuchi	33.6	3.36	54.2	5.3	**58.5**	**5.8**	42.8	4.2
24 Ophiuchi*	6.7	**67.5**	**6.2**	62.5	6.3	64.4	5.7	58.1
28 Ophiuchi	5.7	6.3	**5.7**	**7.2**	5.7	6.1	7.7	4.8
O Ophiuchi*	9.9	10.0	11.3	8.7	10.5	10.2	**12.1**	**8.6**
31 Ophiuchi	4.8	4.8	6.9	4.0	6.1	5.9	5.8	5.0
28 Scorpii	10.3	3.5	**9.4**	**5.9**	7.3	2.1	4.7	2.5
22 Ophiuchi	5.3	9.5	6.2	3.9	5.5	10.6	7.4	6.4

Table 4.1: Values of standard deviation of the stars on the basis of the polarization orientation: 35°, 65°, 105° and 145°.

The findings are summarized in Table 4.1 with polarization: 0°, 35°, 65°, 105° and 145°. We calculated the standard deviation values based on the polarization angle, as described in Section 2.1.1. This work holds significance as it marks the deployment of the first liquid-crystal polarizer in space.

In Table 4.1 is reported the mean value of the acquisition is calculated on the basis of the polarization. In the results, there are noticeable variations in the standard deviations among different polarizations. We have observed that these discrepancies cannot be attributed to the integration time but are instead caused by background noise and the presence of double stars, resulting in a less significant agreement of the data with a Gaussian fit. Yet, the precision of the Gaussian fit is reliable enough to determine whether the requirements are fulfilled, which will be demonstrated further on. Besides, we are working on the subtraction and creation of a double Gaussian model for double stars to obtain even better precision.

We ensured a rigorous evaluation of compliance with the requirements, focusing on worst-case scenarios where the channel has a high value for x and y, except for 31 Ophiuchi, where we evaluated the couple with the maximum value along x. Accordingly, we considered the most unfavorable results obtained during the assessment.

The requirements, indicated in green in Table 4.2, are divided into three parts based on the FoV ranges: 1.6° $<$ FoV $<$ 1.8°, which represents the area near the IO; 1.8° $<$ FoV $<$ 2.1°, covering the central part; and FoV $>$ 2.1°, representing the outermost limits.

For each FoV range, specific criteria are defined. In the first range, the requirement is that within a box measuring 60 × 60 arcsec, the ensquared energy must exceed 60%. In the second requirement, both the box size and the ensquared en-

Angles	**1.6°<FoV<1.8°**		**1.8°<FoV<2.1°**		**FoV>2.1°**	
	x (arcsec)	y (arcsec)	x (arcsec)	y (arcsec)	x (arcsec)	y (arcsec)
Requirements	60×60> 60%		40×40>80%		25×25 >80%	
On-ground	19.0	10.5	10.0	10.0	10.3	11.0
26 Scorpii					58.5	5.8
24 Ophiuchi*			6.6	67.5		
28 Ophiuchi					5.7	7.2
O Ophiuchi*					12.1	2.3
31 Ophiuchi					13.9	4.2
28 Scorpii	9.4	5.9				
22 Ophiuchi					5.8	10.6

Table 4.2: In green the requirements defined during the project, the sigma of the pinhole measured on-ground [4], after the deconvolution, and the standard deviation measured with the stars.

ergy threshold change. The box measures 40×40 arcsec, and the required energy within it must be more than 80%. The third and final requirement involves a box size of 25×25 arcsec, with the ensquared energy inside exceeding 80%.
During the analysis performed on the on-ground data (details available in [4]), a pinhole was used for point sources. Before the calculations, a deconvolution process was performed, and the resulting σ values are presented in Table 4.2

The analysis conducted both on-ground and in-flight is as follows: we compared the calculated σ values for the first set of requirements, as σ represents 68.3% of the signal under the assumption of Gaussian distribution. For the second and third requirements, 1.3σ corresponds to 80% of the Gaussian distribution, and therefore this value has been chosen.
Based on the values obtained, we then measured the energy contained within the respective box for each requirement: 2σ and 2.6σ.
Upon analysis, we found that out of the 7 stars analyzed, 5 were in focus, while 2 showed defocus either in the x-axis or the y-axis. The stars that did not meet the requirements are highlighted in orange and include 26 Scorpii and 24 Ophiuchi*[1].

---

[1] The asterisk (*) notation denotes that the star is part of a binary system, indicating the presence of a companion star in close proximity. In a binary star system, two stars orbit around a common center of mass, and their gravitational interaction influences their behavior and characteristics. The presence of a companion star can have significant implications for the stellar dynamics,

To investigate the reasons behind the defocusing of these stars, we conducted simulations analyzing all the calibration stars that passed in front of Metis since the beginning of the mission.
Details of this investigation are presented in the subsequent section.

4.3 Metis stars acquired and simulation

Before explaining how the analysis is performed, it is essential to understand the image acquisition process and the simulation methodology using Zemax. This section will first describe how the images are acquired from Metis and processed to obtain the necessary data. Subsequently, we will outline the simulation approach in Zemax, which allows us to model the optical behavior of the system under different conditions. This comprehensive understanding of the data acquisition and simulation process will pave the way for a detailed exploration of the analysis conducted on the calibration stars.

4.3.1 Acquisitions

The acquisition of images requires careful planning, as described in section 2.1.4, including the selection of the target and the appropriate integration time. Once the spacecraft is accurately pointed, the acquisition begins.
For images regarding the in-flight calibration, the solar corona is in the background, while calibration stars are the primary targets.
The images are in the FITS format (Flexible Image Transport System), including a header. The header contains all the metadata, i.e. the information about how the image is acquired. From all of this we can extrapolate information for the PSF study, and an example of a FITS image is presented in figure 4.7, where:

- Pol ID represents the polarization which image is acquired, in this case is 0° (more information for the polarization are in the 2.1.1.)
- D30 is the DIT (Digital Integration Time) of the acquired image in seconds.
- ND1 is the NDIT that is to say how many images have been averaged before being sent to the Earth, in this case is 1.
- OBT 30 is the Observation time span, in seconds.
- Dp0.1 is the motion blur in pixels during the OBT.
- the numbers before deg are the PSF coordinates wrt LoS (Line of Sight).

---

evolution, and observational properties of the binary system. The asterisk notation is commonly used to distinguish binary stars from single stars in astronomical catalogs and observations.

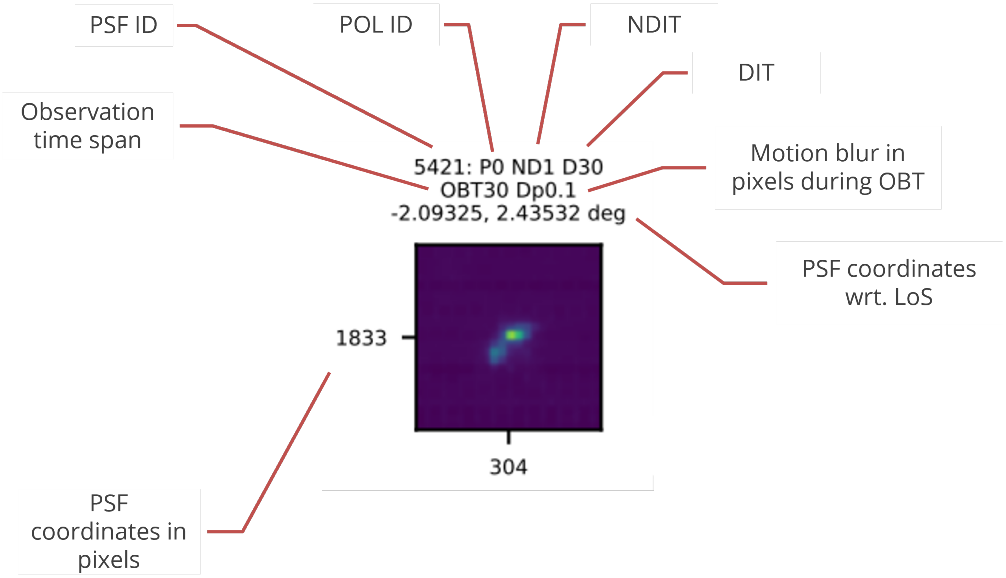

Figure 4.7: Stars information retrieved by the header of the image. Courtesy of Paolo Chioetto.

- the location of the PSF in pixels (see abscissa and ordinates).
- PSF ID, it is the only parameter not extracted from fits, it is the number automatically assigned when we search the star in a set of images with the 3 sigma algorithm described above.

In the specific case of Comet Leonard, the objective was to acquire images with NDIT=1, meaning no averaging with other images, in order to preserve all the information. The images were taken in visible light and polarization, ranging from 0 to 4.

4.3.2 SIMULATIONS

The simulations conducted using Zemax were aimed at analyzing the PSF. In this simulation, we generated nine point sources placed on the aperture, represented by the circular image on the left side of the figure 4.8. The central image, in the same figure, illustrates how the source points appear on the visible detector.
The simulation was performed with the IF tilted by x: -0.369° and y: 0.77°. Indeed, at the beginning, we constructed a ”perfect” reference version of the Metis coronagraph in which no movements or changes were made to the internal optics. By comparing the simulated images on the detector using the ”perfect” version with

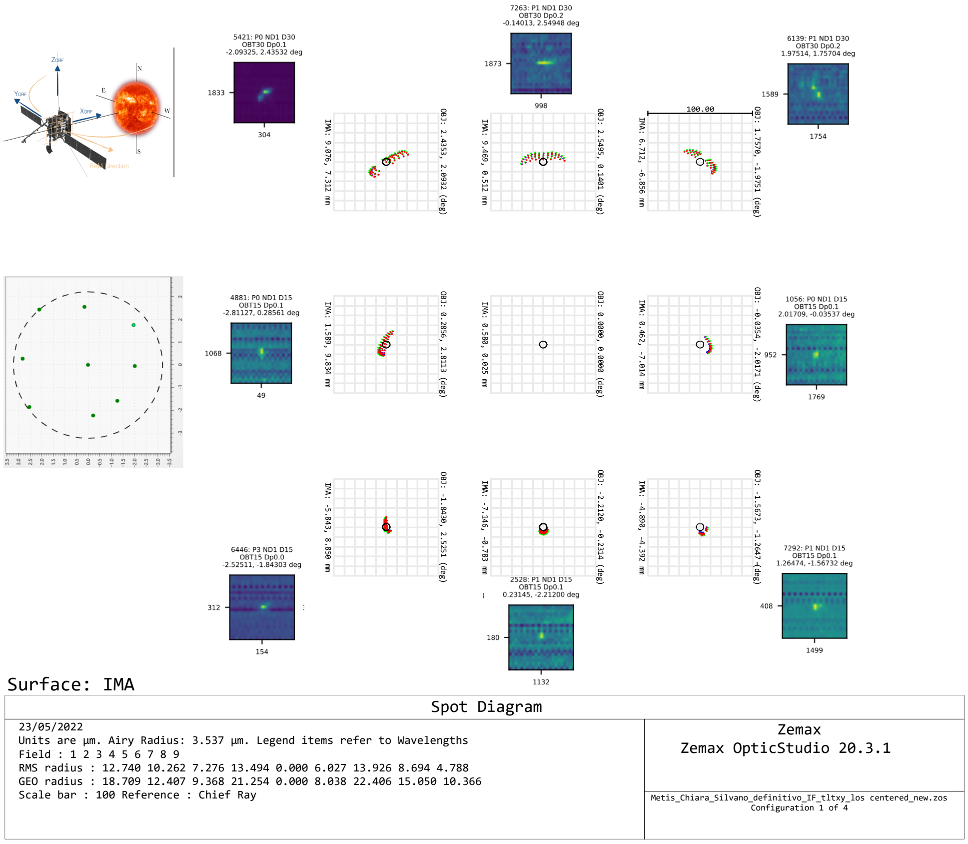

```
23/05/2022
Units are µm. Airy Radius: 3.537 µm. Legend items refer to Wavelengths
Field : 1 2 3 4 5 6 7 8 9
RMS radius : 12.740 10.262 7.276 13.494 0.000 6.027 13.926 8.694 4.788
GEO radius : 18.709 12.407 9.368 21.254 0.000 8.038 22.406 15.050 10.366
Scale bar : 100 Reference : Chief Ray
```

```
Metis_Chiara_Silvano_definitivo_IF_tltxy_los centered_new.zos
Configuration 1 of 4
```

Figure 4.8: Simulation of stars performed with Zemax and in the blue boxes the real images acquired by Metis. Courtesy of Paolo Chioetto.

the real images (stars, flat field) we constantly observed discrepancies. It is important to note that during the integration phase, adjustments were made to both IF and IO, the first to minimize the defocus on the VL channel, and the second to minimize the impact of stray light. Furthermore, other movements were performed in-flight for the IO. Unfortunately, since no documentation on the specific changes made to the IF is available, replicating both movements in our simulations proved to be impossible. Therefore, we solely focused on simulating the movement of the IF. We observed that the discrepancies disappeared while using the tilted version of the IF presented above, justifying its use for the simulation.

In figure 4.8, the black circle represents the simulated Airy Disk radius, while the colored dots correspond to different wavelengths considered within the visible range. The bottom of the image provides information about the RMS (Root Mean Square) radius, which represents the spot size, and the GEO radius, which denotes the distance from the centroid to the furthest ray intersection with the imaging surface. The IMA descriptor indicates the location of the centroid on the imaging surface, while the OBJ describes the field points location in terms of field angles. The results of this simulation are compared with the in-flight acquisitions in order to identify why we had a poor percentage of the signal collected for the 26 Scorpii and 24 Ophiuchi stars.

4.3.3 Comparison

Based on the findings presented in Table 4.2, it is evident that certain stars suffer from defocus issues in both the in-flight and simulation data. Notably, the upper part of the detector housing 26 Scorpii, and the central region featuring 24 Ophiuchi, exhibit significant defocus problems. These observations are visually represented in Figure 4.8. As a result, it is evident that there are portions of the detector that are in focus, while others, including the aforementioned areas, suffer from defocus.

The qualitative comparison of the PSFs indicated a defocus of -0.1mm, which is evident in the similarity between the stars (indicated by the blue squares) and the simulation.

The radiometric model that is built out of this remains an ongoing work, due to one interesting particular case, which is not invalidating our study. Indeed, during the analysis of the Point Spread Function (PSF), an interesting observation was made regarding the presence of a spider structure. The stars located along the spider structure appeared to split, as illustrated in figure 4.9. Consequently, stars in proximity to the spider structure were observed as two distinct sources. This represents a challenge when attempting to extract accurate information about the PSF for stars at such specific positions. To address this issue, further investigation is currently underway. An area of focus involves developing a metric to compare simulated PSFs with real PSFs. By establishing an appropriate metric, it may be possible to refine the simulation and bring it closer to the measured PSFs.

Note that real PSFs obtained from stars are often characterized by noise, which makes it challenging to perform a straightforward 2D Gaussian fit. Efforts are being made to overcome this difficulty and develop a suitable deconvolution function for image adjustment.

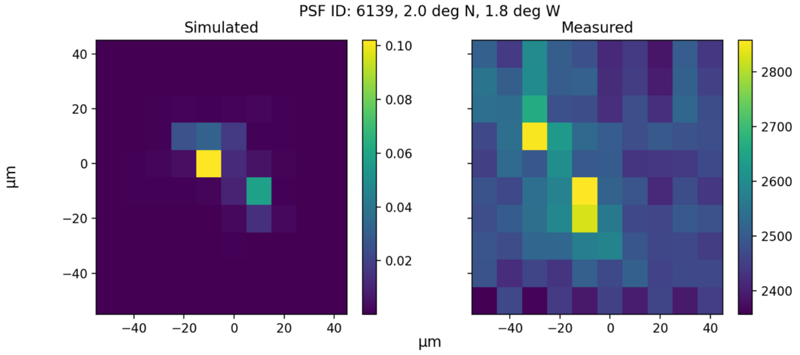

Figure 4.9: Stars located along the spider structure, particularly on the top right portion of the image. On the left side of the image, the stars are simulated, while on the right side, they are real observations.

References

[1] D. Claus and A. W. Fitzgibbon. "A Rational Function Lens Distortion Model for General Cameras". In: *2005 IEEE Computer Society Conference on Computer Vision and Pattern Recognition (CVPR 2005), 20-26 June 2005, San Diego, CA, USA*. 2005, pp. 213–219. DOI: `10.1109/CVPR.2005.43`.

[2] E. Simioni et al. "SIMBIO-SYS/STC stereo camera calibration: Geometrical distortion". In: *Review of Scientific Instruments* 90.4 (Apr. 1, 2019), p. 043106. DOI: `10.1063/1.5085710`.

[3] G. Nicolini. *METIS Technical Specification*. Tech. rep. OATO.

[4] C. Casini. *Calibrazione del coronografo spaziale Metis della missione Solar Orbiter*. 2018. URL: `https://www.researchgate.net/publication/328998046_Calibration_of_the_spatial_coronagraph_Metis_on_board_Solar_Orbiter`.

5

Data analysis and results for Metis and STC

In astronomical images, the calibration of captured images is crucial to obtain correct scientific information. Two key components of this calibration process are flat-field correction and dark subtraction. The scope of this chapter is to describe: the flat field analysis on the images acquired by Metis, and the dark analysis performed on the STC images.
An internal calibration source system, using three LED sources to simulate a uniform illumination, was foreseen to perform in-flight flat-field verification. However, these LED sources did not work, and thus an alternative approach has to be devised; the idea of utilizing the light retro-reflected from the door in front of the Metis instrument was proposed and is described in this chapter. Besides, inspired by the practices of numerous astronomical instruments, the second idea centered around harnessing the inherent light of stars for flat field correction.
In the last two sections, the work performed with the dark images in order to verify the STC detector integrity is presented. Depending on the integration time chosen, special care should be given to some regions of the CCD matrix array.

5.1 Analysis of the retro-reflection from the Metis closed door

On the spacecraft, Metis is located behind the heat shield on the front face of Solar Orbiter. The shield reflects solar light, as shown in Figure 5.1, allowing a portion of it to enter the Metis aperture through reflection on the shield and the titanium door. Between the door, in closed position, and the heat shield there is a gap that allows the passage of a fraction of the reflected sunlight. The acquired images, taken at various exposure times and distances from the Sun with the door closed,

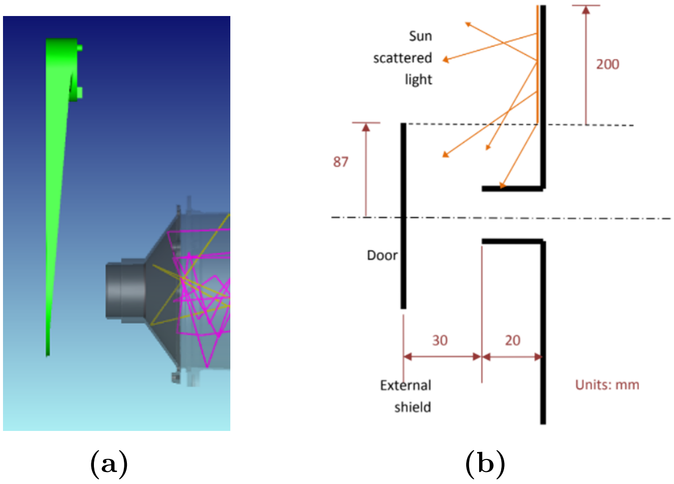

Figure 5.1: (a) CAD lateral view of Metis in front of the door (green). Scheme of the sunlight interacting with the shield, it scatters in the direction of the door. Subsequently, the door scatters the light once again, causing a portion of it to enter the Metis aperture, which is located approximately 30 mm away from the door [1].

were analyzed. The Short-Term Planning (STP) sessions considered, as described in 2.1.4, are: STP-122, STP-130, STP-136, STP-139, STP-140, STP-144, STP-162, and STP-175, with corresponding dates, exposure times, and distances from the Sun provided in Table 5.1. With these images, we performed the studies presented in the following subsection.

5.1.1 Flat field in-flight

In the chapter 3, we described the importance of having a uniform light source for the calibration process. We explore here the feasibility of utilizing the retro-reflection of the door as a potential light source. The approach involved comparing the on-ground measurements of the field of view, as illustrated in Figure 3.3 a and b, with the in-flight measurements taken using the retro-reflection of the door, as shown in Figure 5.2 a and b.

After conducting a thorough examination of the radial profiles acquired in-flight, namely 0°, 180° (blue); 90°, 270° (purple); 45° and 225° (light blue); and 135° and 315° (garnet), all profiles were normalized to the maximum value of the image. Regrettably, the in-flight profiles did not consistently align with the anticipated results. As a consequence of these discrepancies, we have concluded that relying on the retro-reflection of the door as a consistent and reliable flat field panel for

STP	t=1 s	t=1.2 s	t=1.4 s	t=1.5 s
122 (0.94 AU) 16/11/2020	✓	✓	✓	
130 (0.61 AU) 13/01/2021	✓	✓		✓
136 (0.53 AU) 22/02/2021	✓	✓		✓
139 (0.65 AU) 15/03/2021	✓	✓		✓
140 (0.72 AU) 25/03/2021	✓	✓		✓
144 (0.86 AU) 20/04/2021	✓	✓		✓
162 (0.67 AU) 17/08/2021	✓	✓		✓
175 (0.95 AU) 15/11/2021	✓	✓		✓

Table 5.1: Session names, distances from the Sun, acquisition dates and the exposure times for each STP considered.

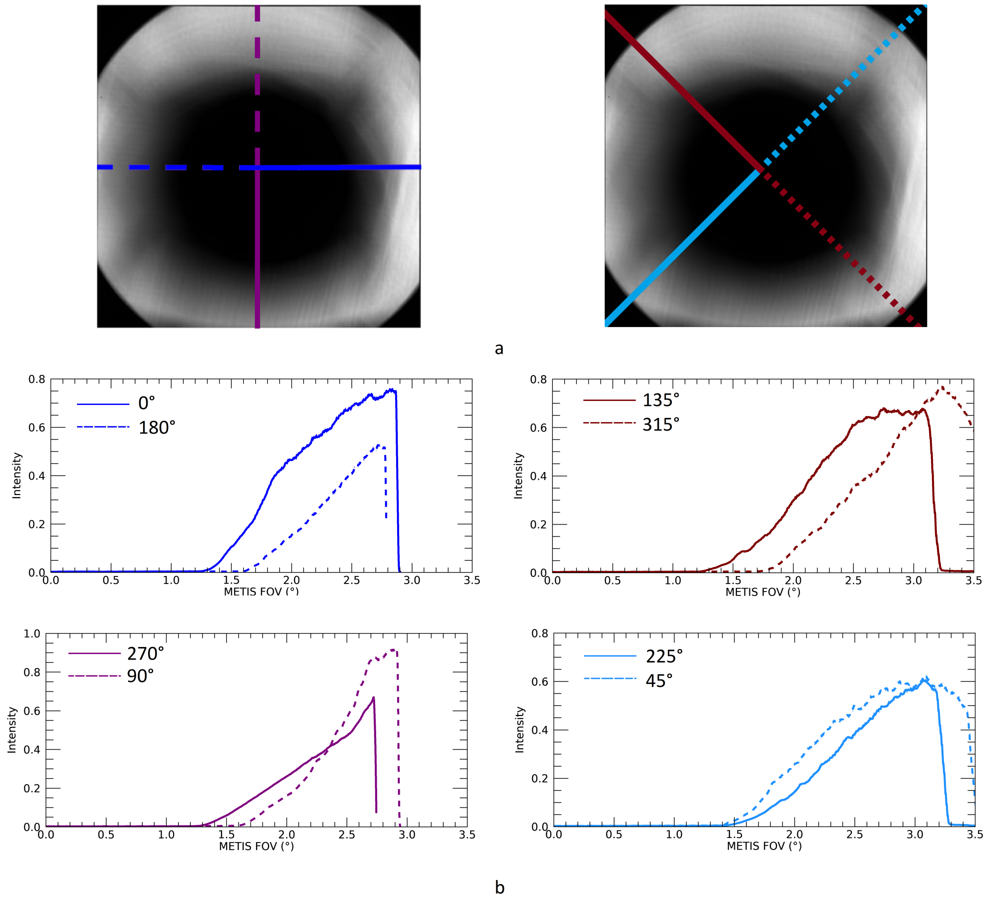

Figure 5.2: Radial profiles of the retro-reflection of the door acquired in-flight: 0°,180° (blue); and 90°,270° (purple); 45°, and 225° (light blue); 135° and 315° (garnet).

the calibration process is not viable.
Despite this outcome, it is important to highlight that this analysis provides valuable insights. Specifically, it facilitates the monitoring of the relative instrument response throughout the mission's duration and enables the prediction of potential variations using ray-tracing simulations. This is the reason why we pursued this study and verified its accordance with the $1/r^2$ law.

5.1.2 $1/\text{R}^2$ LAW

To assess the conformity of the door illumination with the $1/r^2$ law, we use the images with exposure time of 1 s, we subtracted the dark and bias, then we selected

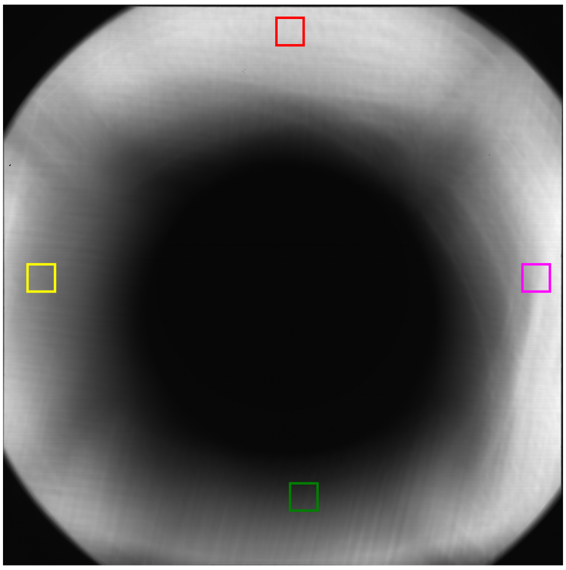

Figure 5.3: Image of the session STP 175 at exposure time texp=1 s, after the subtraction of the dark and bias, the boxes are positioned with dimensions of 100 pixels by 100 pixels

four 100-pixel x 100-pixel boxes, as shown in Figure 5.3 for the example of the STP 175. Mean intensity values for each box were plotted against the distance from the Sun. The resulting trends exhibited agreement with the 1/r^2 law as shown in Figure 5.4. The red line in 5.4 represents the trend of the mean value of the red box in Figure 5.3, while the green and magenta box trends were similar, resulting in overlapping lines. The yellow line represents the low mean trend.

With the exception of STP 136, all values are taken into account. The discrepancy in STP 136 is attributed to an inefficiency in the algorithm used for bias subtraction for the 1 s integration time.

The consistent matching of experimental values with the 1/r^2 fitting curves, as shown in Figure 5.4, indicates that there is no significant damage to the door or the subsequent optics: indeed in case of damage occurring to either the door or the optics, it could result in one of the boxes exhibiting higher or lower intensity, thereby causing a deviation in the observed trend. To determine which "part" has incurred damage, it would be necessary to conduct a study of the flux detected from calibration stars. If the flux corresponds to predetermined values, it can be confidently inferred that the damage is primarily due to the door. Conversely, if the star flux does not match the values documented in the literature, it indicates damage in the optics.

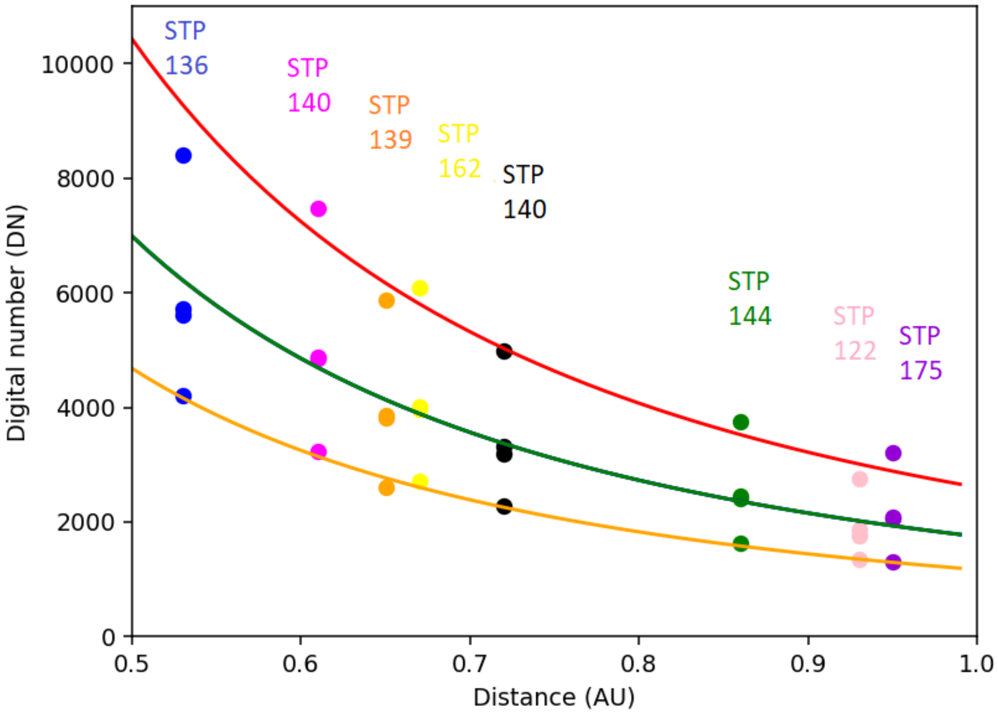

Figure 5.4: The Digital Number (DN) values inside the boxes vary at different distances from the Sun, following the $1/r^2$ law, where 'r' represents the distance. The red line on the graph illustrates this relationship. The black dashed line corresponds to the error margins associated with both the red and dark yellow lines.

Therefore, if retro-reflected light from the door cannot be used as in-flight calibration source, it is very valuable for instrumental monitoring throughout the mission. As far as uniform in-flight calibration source is concerned, we use (as introduced in the previous chapter) the stars that pass in the Metis FoV.

5.2 Stars inside Metis FoV and vignetting

Determining the crossing of stars in the Metis FoV requires first describing the instrument vignetting. During integration and calibration, the IO and IF were adjusted to reduce stray light and improve the focus of light on the visible focal plane. Figure 5.5 (a) shows the vignetting function measured on-ground after these adjustments. To generate the simulated vignetting image, we used Zemax and constructed a theoretical model of the Metis telescope with perfectly aligned optical elements. The image of the simulated vignetting function displayed in 5.5 (c) was computed using Zemax's "geometric image simulation" feature.

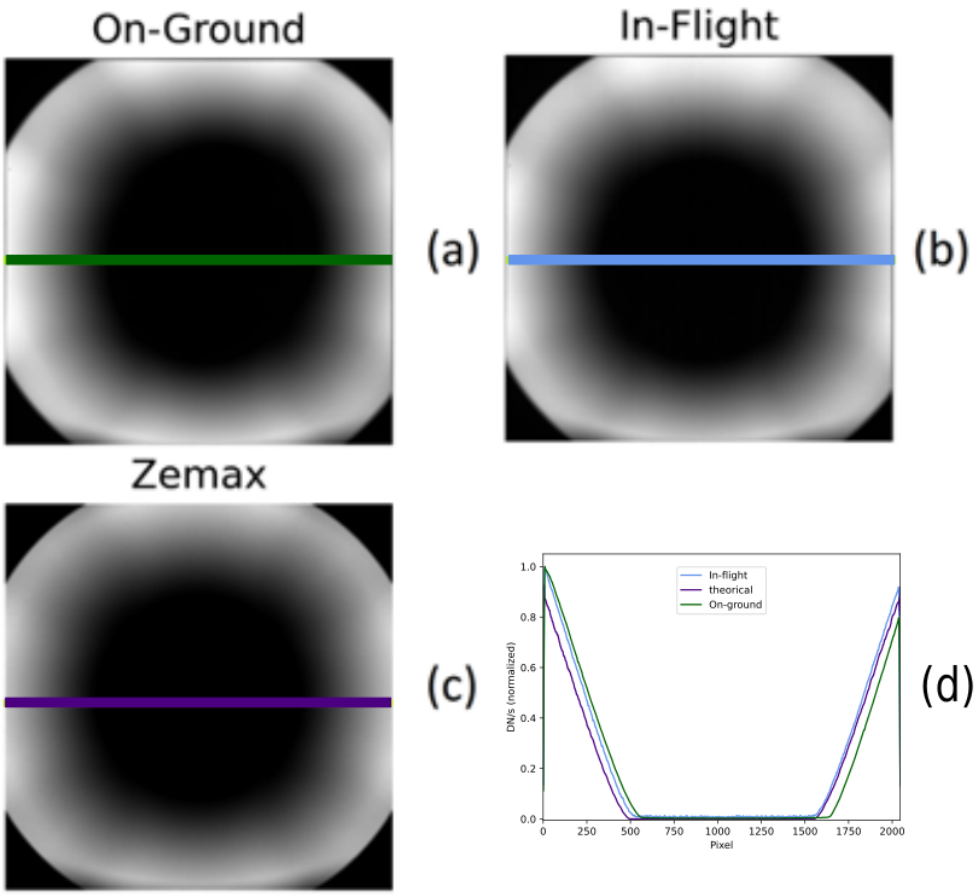

Figure 5.5: The images of the vignetting function are presented as follows: (a) acquired on-ground, (b) adjusted in-flight and (c) simulated by Zemax. In each image, the direction of the vignetting is indicated by the colored lines, plotted in (d).

After launch, during in-flight commissioning, the IO was repositioned to address the increased stray light measured level. Consequently, a new vignetting image, 5.5 (b), was created. To obtain the in-flight vignetting function, the on-ground image was recentered using an isophote-based method described in [2]. All images are oriented with solar North up. The colored lines indicate the position of the vignetting plot.
Figure 5.6 presents an image captured by the Metis coronagraph in March 2021 with a 20 second exposure time. The green box indicates the region where the Theta Ophiuchi star is located, and a 10 x 10-pixel zoomed-in view of this region

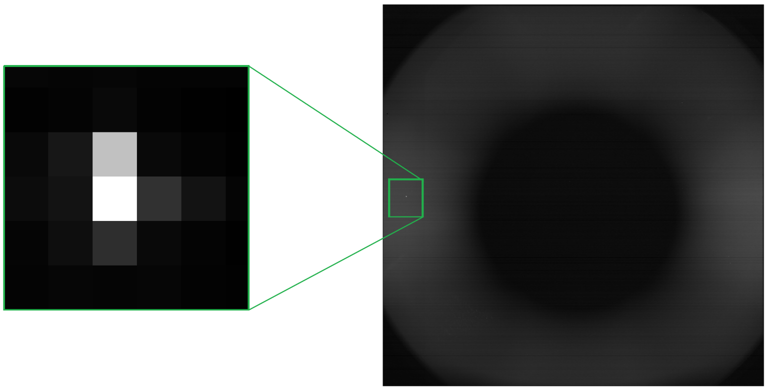

Figure 5.6: The image was captured in March 2021 with polarization angle=105°, and within the frame, Theta Ophiuchi is enclosed within the green box. On the left side, there is a zoomed-in view of the star, presented in a box measuring 10 x 10 pixels.

is shown on the left side of the same figure.

In figure 5.5, the colored lines represent the direction along which the vignetting was plotted for the first star passage. Images were acquired at different exposure times (20 and 30 s) and different distances from the Sun. Theta Ophiuchi passed twice in front of Metis, and the Short-Term Planning (STP) sessions considered were STP-140 and STP-182. The first case involved image acquisition on 25/03/2021 at a distance of 0.72 AU from the Sun. In the second case, STP-182 was conducted on 20/12/2021 at a distance of 1.01 AU from the Sun. We report the analysis made for the first passage.
During the star passage, Theta Ophiuchi traversed rows 1017 ± 2 pixels. To analyze the vignetting function, a 10-pixel x 10-pixel box surrounding the star was selected. The mean values were evaluated for four adjacent boxes of the same size, located to the right, left, top, and bottom of the star bounding box. These mean values included background information such as the solar corona or zodiacal light. The mean background values were subtracted from those measured in the star bounding boxes. Once this background subtraction has been performed, intensities of the stars are acquired, allowing an experimental in-flight vignetting curve to be built.

Figure 5.7 presents intensity plots for different vignetting functions: in-flight, on-ground, simulated with Zemax, and derived from the first (see figure (5.7)) passages of Theta Ophiuchi. All plots are normalized to their maximum intensity.
The star traversed the entire detector, and the vignetting function profiles derived

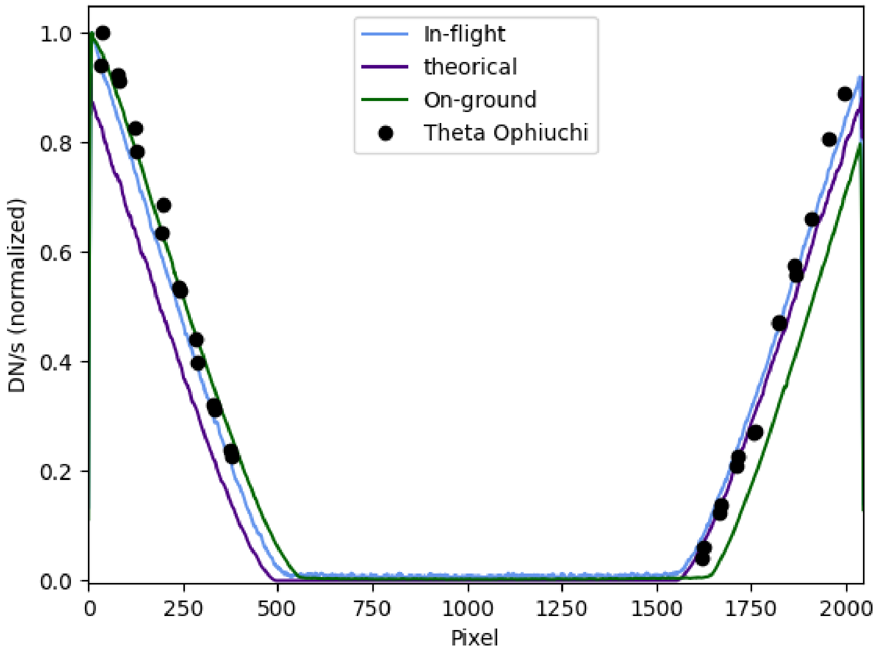

Figure 5.7: Plot of vignetting function measured on-ground, in-flight, with Zemax and the theta Ophiuchi, during the passage in March (row 1017).

from the star transit agree with the in-flight vignetting function (light blue line) with an average difference of around 10%. As expected, there is a shift between the in-flight and on-ground vignetting functions due to the recentering process employed to obtain the in-flight vignetting function, which will be explained in this chapter. The simulated Zemax vignetting curve (purple) agrees well with the in-flight vignetting in the left part of the frame but not in the right part because it does not account for the IO and IF movements performed during the on-ground instrument alignment.
This work can be updated annually to study the evolution of vignetting, and any changes and developments must be carefully studied. Indeed, it is important to remind here that Solar Orbiter is the first mission operating this close to the Sun.

Vignetting simulations with Zemax

After our work on the star, we decided to focus our efforts on finding the best vignetting calculated by Zemax. To achieve this, we conducted a comparison between the Zemax-produced vignetting and the in-flight adjusted vignetting.

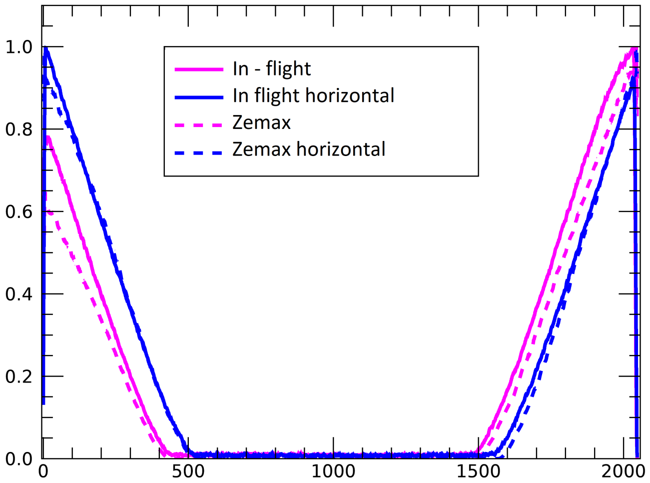

Figure 5.8: Comparison from the vignetting adjusted in-flight (straight line) and that performed by Zemax (dotted) along the central horizontal (blue) and the central vertical (magenta) profile.

After months of diligent work, we managed to identify the best agreement so far, as shown in Figure 5.8: a comparison was made between the in-flight adjusted vignetting (represented by straight lines) and the Zemax calculated vignetting (represented by dotted lines) along the central horizontal (blue) and central vertical (magenta) profiles. From the figure, the horizontal lines exhibit differences of less than 10%, while the vertical lines have differences exceeding 20%. We are continuing our efforts to improve the calibration to achieve more satisfactory results. Yet, we can already claim that our study permitted to define a successful strategy concerning in-flight vignetting calibration, which will lead to results in accordance with our expectations over time.

5.3 STC Dark images

As written at the beginning of this chapter, the characterization of the detector dark current is extremely important for obtaining reliable scientific images. In the framework of this PhD thesis, analysis of the dark current has been performed for STC.

5.3.1 STC Dark images acquisitions

Dark current acquisitions were performed during various Instrument Check-Out (ICO): 1 (September 7^{th} 2019), 2 (November 11^{th} 2019), 3 (June 6^{th} 2020), 4 (December 14^{th} 2020) and 7 (May 26^{th} 2022). Each telecommand instructed the acquisition of a specific sequence of dark current images, with a designated Integration Time (IT) and Repetition Time (RT).
The dataset was organized into two groups:

- panchromatic filters (WINX, PANH, and PANL) - 3 windows;
- color filters (WINX, F750, F420, F550, and F920) - 5 windows.

We recall that the Panchromatic filters have dimensions of 896 $\times$ 384 pixels, the colored filters 896 $\times$ 64 pixels, and the WINX has dimensions of 64$\times$ 128 pixels.
Commonly for each session series 10 images are acquired, except for: ICO 3 where, for the colored filter, the series is formed by 5 images; and in ICO 7 where the series is formed by 12 images.
In general, the integration times for the panchromatic filters increased from 0.45 seconds to 7 seconds, and the repetition time was 7 seconds for all images except the last one, which had a repetition time of 9.9 seconds. For the color group, the integration times increased from 0.25 seconds to 5 seconds, and the repetition time was 5 seconds.
The integration and repetition times were selected based on the planned operations for STC at Mercury. Wait times between acquisitions were also included in the dataset. Each acquired image consisted of 5 windows for the color filter sequence and 3 windows for the panchromatic sequence.

5.3.2 STC Dark images analysis

For each image, the mean dark current values were calculated to analyze their evolution with the number of acquisitions and integration times. As shown in 5.9 the analysis revealed that the dark current mean value varied within each series of 10 images with the same integration time. The first image in each series usually had the highest value (peak value), and the mean value decreased throughout the series.

Further analysis has shown that the peak effect was less prominent in the second part of the test, where the repetition times were longer. The images acquired with shorter repetition times (5 s for color filters and 7 s for panchromatic filters) exhibited more pronounced peaks compared to the images acquired with longer repetition times (5 s for color filters and 7 s for panchromatic filters). The difference in dark values between the first and last images in a series depended on the elapsed

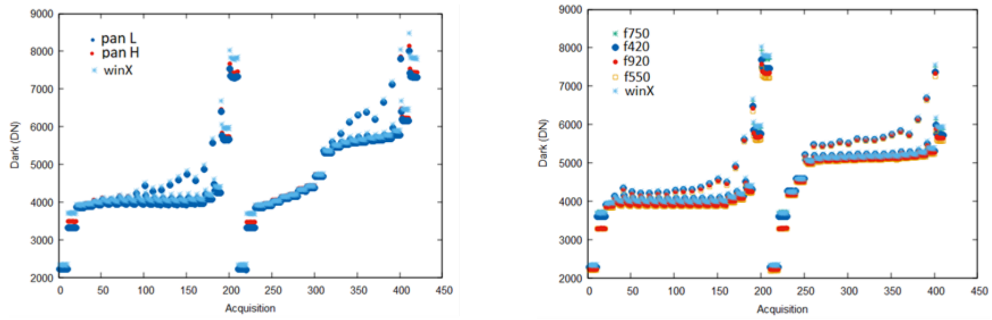

(a) **(b)**

Figure 5.9: Mean values of the dark current for the filters and WINX during the acquisitions of the ICO1 campaign, plotted against the image number of the series. (a) the data for Pan H (red dots), Pan L (blue dots), and WINX (light blue dots). (b) the mean values for F750 (green symbol), F420 (blue dots), F920 (red dots) dots, and F550 (orange symbol). The data for WINX is also included, represented by light blue symbols.

time between the series and the commanded repetition time.

The non-constant dark current behavior was attributed to an inefficient ”reset” of each detector pixel. To mitigate the peak issue, the small window named WINX was used for calibration. The WINX window was located in the unilluminated part of the detector. The Offset Dark Subtraction (ODS) strategy was applied to each pixel within the WINX window by subtracting the mean value of WINX from the measured value.

Analysis of mean dark values with integration times revealed different trends for different filters and repetition times. In general, the mean dark value increased initially, reached a stable phase, and then increased again for longer integration times. The behavior varied depending on the specific filter and the repetition time.

Once the scientific images are acquired, the dark frames will be subtracted. This approach including the WINX window is very important, since the dark frames for background subtraction can only be acquired as long as the MPO module remains stacked in the flight configuration with MMO in front; after the separation, it will no longer be possible.

In order to exploit at best the acquired dark frames, we have decided to use them to study bad pixels.

5.4 STC Bad pixel analysis

Alongside the importance of background subtraction for image acquisition, it is important to consider also that a pixel’s reliability may be compromised due to defects in the electronics used for reading and accessing data from sensors, or due to the pixel's own response behavior. However, for this work's application, we focus on grouping anomalous pixels based on their behavior in the resulting image, specifically in terms of their grayscale values. Usually, the bad pixels are classified as follows:

- **Linear pixels with false bias (more problematic in a CCD)**: These pixels exhibit linear behavior with respect to illumination intensity or exposure time. However, due to either a low or high bias compared to neighboring pixels, under homogeneous illumination, the displayed values significantly differ from those around them.
- **Nonlinear pixels**: These pixels do not display output signals on the image in a linear manner concerning illumination intensity or exposure time.
- **Dead pixels**: These pixels have very low sensitivity to illumination intensity variations and consistently present low grayscale values.
- **Hot pixels**: In this category, pixels are highly sensitive to illumination intensity variations or exposure time, displaying persistently high grayscale values.

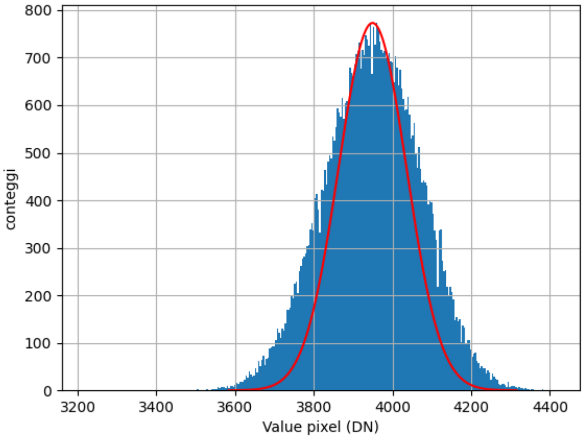

Figure 5.10: Histogram and Gaussian profile for the F550 filter for the 5th image of the series acquired at 384 us.

To identify the "bad" pixels, for each image, we plot the histogram of grayscale values, shown in blue in Figure 5.10, alongside a Gaussian fit curve with a width

of σ, corresponding to the standard deviation of the grayscale values distribution. Any pixel whose DN value lies outside the mean $\pm 3\sigma$ range is considered as a bad pixel.
The pixel value distribution was calculated for each image in the series, considering each window individually. We constructed a lookup table (a matrix) of the same size as the original acquired window. For each pixel, which grayscale lies outside the Gaussian profile (i.e. bad pixel), we assign the number 1. We then summed all the lookup tables and normalized the result to the maximum value. An example of this process is presented in Figure 5.11. White represents a pixel always detected as a bad pixel; black represents a pixel that has never been detected as a bad pixel; colors represent pixels that have sometimes been detected as bad pixels.

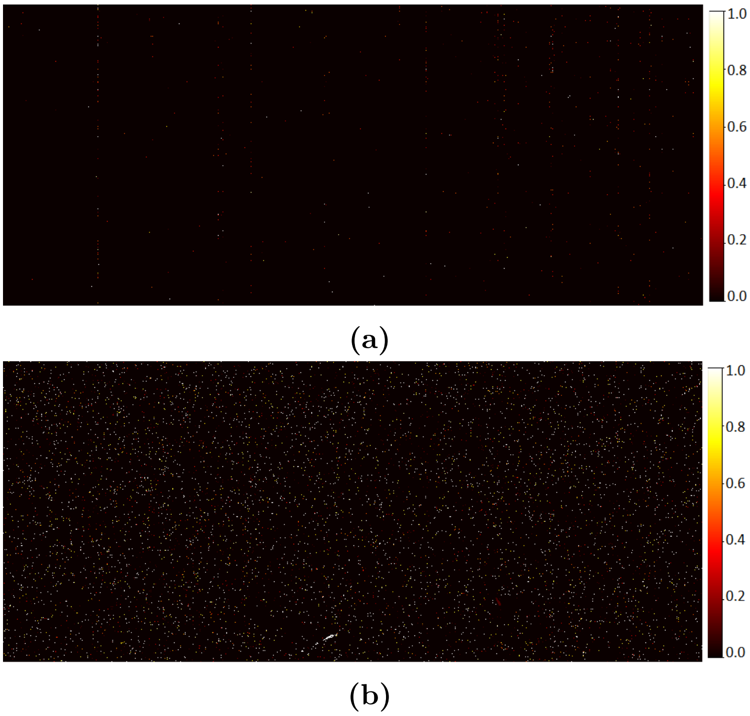

Figure 5.11: Sum of the lookup tables normalized for images acquired with IT 57.6 μs (a) and 9.6 s (b) for the Pan L. The white pixel, value 1.0 on the color bar, is the defective pixel present in all the images of the same IT, while the black point, with value 0.0, is where there is no defective pixel.

For normally (Gaussian) distributed data, only 0.3% of the values lies outside the $\pm 3\sigma$ range. For our data, the percentage of bad pixels is around 0.13% for all color filters and 0.3% for the Panchromatic filter, as shown in Table 5.2. The bad pixels in the table include all the bad pixels identified in images with IT less than

Table 5.2: Amount and percentage of bad pixel detected for each panchromatic and colored filter.

Filter name	Total number of pixels	Number of bad pixels	Bad pixels percentage
	[#]	[#]	[%]
Pan H	344064	1174	0.34
Pan L	344064	1332	0.39
F750	57344	84	0.15
F420	57344	88	0.15
F550	57344	68	0.12
F920	57344	64	0.11

1 second, to exclude artifacts arising from thermal noise as shown in the lookup table in figure 5.11. In general, for ITs ranging from 400 ns to 0.24 s, the ”same” image is observed. When studying images up to this value, we encounter a ”popcorn” effect that is clearly visible in Figure 5.11 b. This effect, present in all filters and panchromatic, arises from thermal noise becoming more dominant. The effect becomes noticeable in the images at IT = 0.48 s. It is worth noting that this impact is not significant when acquiring images of the Mercury surface, since the integration time (IT) is on the order of milliseconds. However, it becomes highly relevant and crucial when capturing images of stars where the integration time typically exceeds 1 second.
After identifying the bad pixels, we also studied their behavior. Figure 5.12 illustrates the behavior of the bad pixels represented by triangles. The numbers within the triangles indicate the locations of these bad pixels. Despite having higher values compared to the mean value of the images, the trend for these bad pixels remains consistent.

During this analysis, we found that some bad pixels have a grayscale value higher than 12000 DN, and they are located in certain regions of the detector, as shown in 5.11 b. We investigated the distribution of these pixels and the results are presented in the following subsections.

5.4.1 Position of the bad pixel over 12000 DN

For each panchromatic and colored filter, we conducted a study to examine the positions of bad pixels with grayscale values exceeding 12000 DN. Using a code

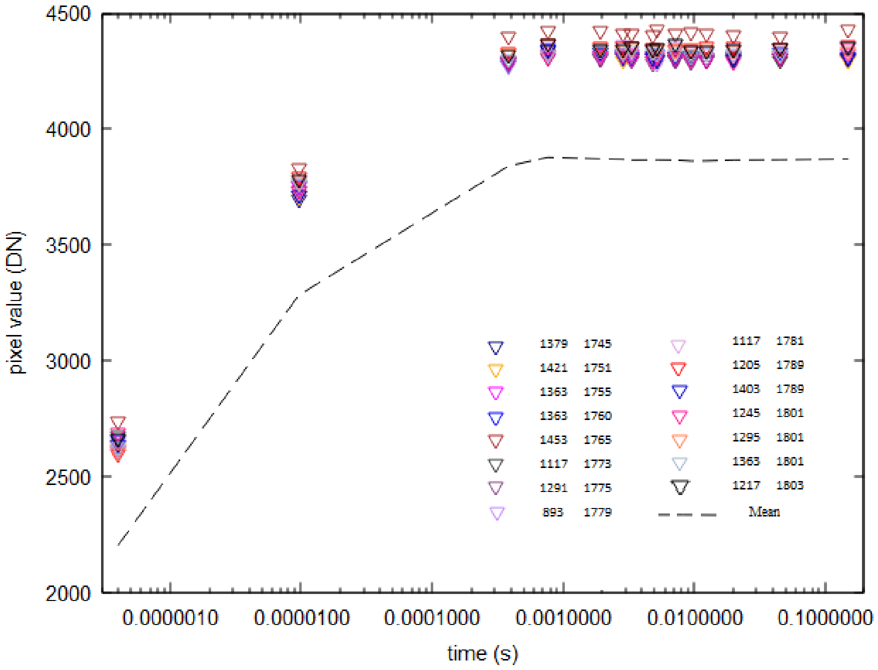

Figure 5.12: Bad pixel values (triangle) at different exposure times for the f550.

similar to the previous one, we created an empty matrix. Each time a bad pixel was found with a grayscale value of 12 000 DN or higher, we assigned a value of 1 to that pixel. After analyzing the images, we normalized them and identified the common positions of bad pixels present in all images.
We found that for the panchromatic filter these bad pixels, with a value higher than 12000 DN, are located in specific regions and from their appearance we have called them: scratches and ”volcanoes”.

In the following section, we investigate in detail these anomalous pixels, which are visible in all the image ICOs acquired.

5.4.2 STC detector anomalies with dark images PanH

In the PanH we observe an intriguing phenomenon, an increase in the appearance of spots in the images, forming three distinct ”volcanoes” with increasing IT, as shown in the black boxes and indicated with the letter a, c and d in Figure 5.13. Instead, in the yellow box, there is a dead pixel (letter b). This will help the reader to orient herself/himself for the next images.
There is a phenomenon present in the PanL, that seems unrelated to that pre-

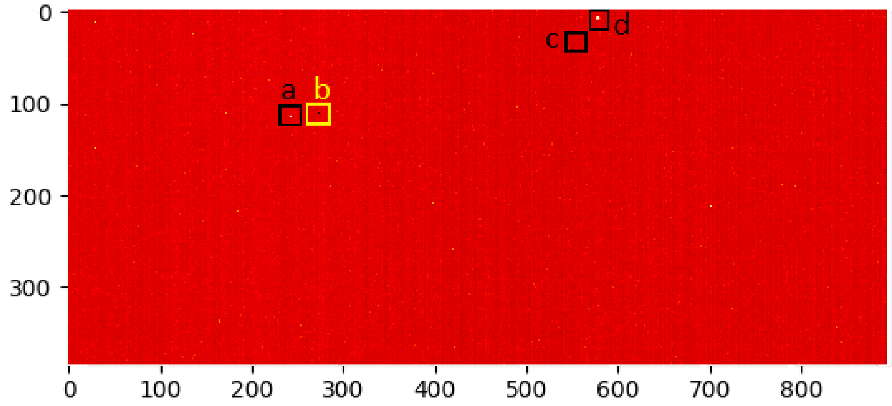

Figure 5.13: PanH at IT=4.8 s, in the black boxes there are the 3 ”volcanoes” (a, c and d), in the yellow box a dead pixel (b).

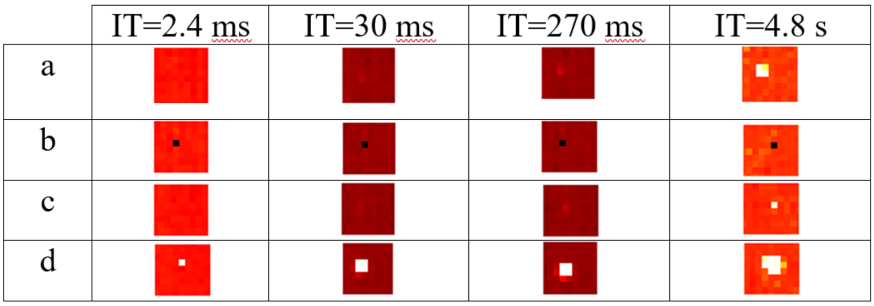

Figure 5.14: Boxes of the dark image of the Pan H. Each box represents a step of the evolution of the ”volcanoes”, the images are acquired with an IT=24 ms s, IT=30 ms, IT=270 ms and IT=4.8 s.

sented in PanH: different evolution over dimensions and time, with respect to the anomaly found in the other panchromatic.

As shown in Figure 5.13, the ”volcanoes” are distributed along the x-axis in the range [250,580], and for the y-axis in the range [10-120].
Referring to Figure 5.14, we can observe the evolution in time of the ”volcanoes” as follows:

(i) The first volcano (d) becomes apparent at IT=2.4 ms.

(ii) The image of the volcano (a) and (c) emerges at IT=30 ms.

(iii) At IT=270 ms the three ”volcanoes” becames easily distinguishable.

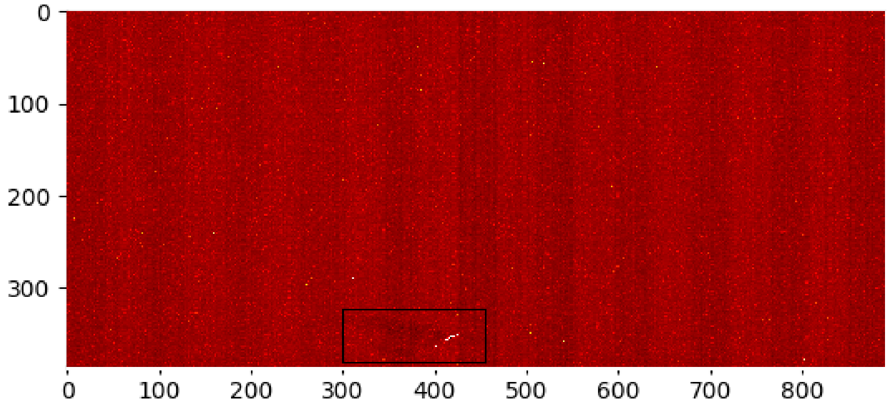

Figure 5.15: PanL at IT=9.6 s, in the black box there is the scratch.

(iv) The three ”volcanoes” reaches their maximum values, as shown in Figure 5.14. We chose to include this particular image instead of the one at 9.6 s since, in the latter case, the presence of thermal noise starts to hinder the visibility of the ”volcanoes”.

The phenomena are currently under further investigation, particularly concerning a problem detected on-ground and briefly described in 3.2.4. They should also be considered for acquisitions with the PanH panchromatic filter.

5.4.3 STC detector anomalies with dark images PanL

In this particular panchromatic, we observe other distinct features, notably a ”scratch” accompanied by its ”shadow,” as illustrated in Figure 5.15. The ”scratch” is enclosed within the box defined by $380 < x < 440$ pixel, and $340 < y < 380$ pixel.

To better comprehend the ”scratch”, we conducted an in-depth analysis of the images at all IT.

The zoomed-in view of Figure 5.3 reveals the growth of the ”scratch”:

(a) at IT = 57.6 μs several bright dots can be observed.

(b) At IT = 2.4 ms, the bright dots increase and expand.

(c) At IT = 9.6 s, the subsequent growth of the scratch is not linear: two more dots emerge at the edges of the previous region, leading to an increase in dimensions.

Table 5.3: Some steps of the evolution of the dots, the (cropped) images are acquired with an IT=57.6 s (a), IT=2.4 ms (b), IT=9.6 ms (c), IT=4.8 s (d).

IT = 57.6μs

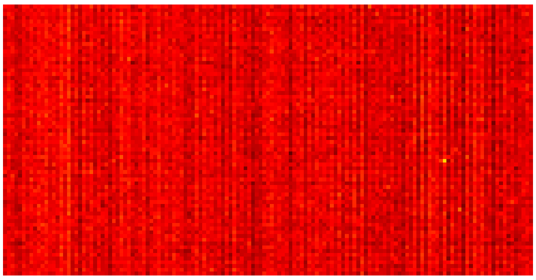

(a)

IT=2.4 ms

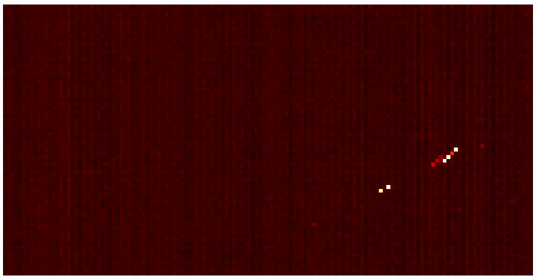

(b)

IT=9.6 ms

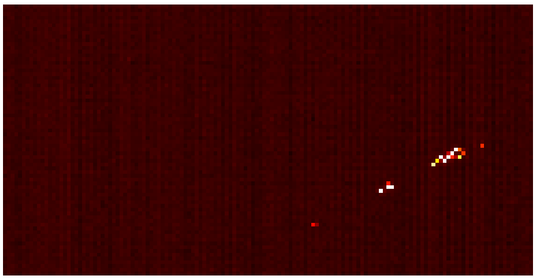

(c)

IT=4.8 s

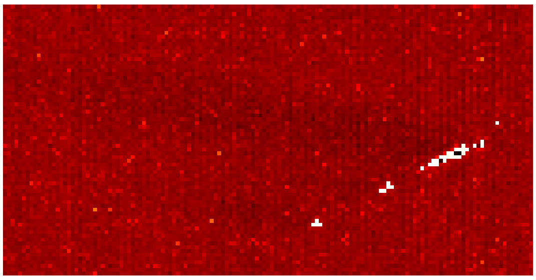

(d)

(d) The top dots merge, forming a distinctive feature, thus earning the name "scratch".

Moreover, within the "scratch", in 5.3 d, we also observe a few dark points, identifiable by their values lower than the mean-3σ, indicating considerable bad pixels.

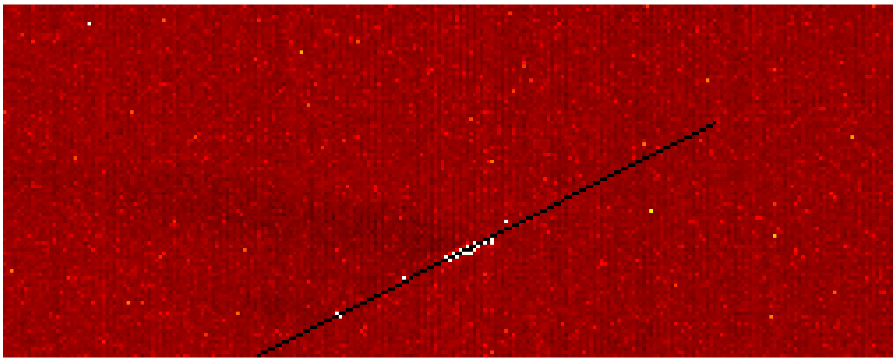

Figure 5.16: Box of the dark image with the scratched, it is aligned following a straight line (black).

Figure 5.16 showcases the "scratch" displayed along a straight line, resembling a cosmic ray, but it is, in fact, not a cosmic ray. Further analyses are underway to delve deeper into this phenomenon.

SHADOW

In Figure 5.16 we can see that perpendicular to the "scratch" there is a shadow. Initially, we examined whether this issue was caused by bad pixels. However, we found that the pixel values were lower than others, but not low enough to classify them as bad pixels. Their values were still larger than the mean-3σ threshold.

To further investigate, we determined whether this shadow was present in all images of the ICO campaigns or only visible in specific images (IT $\geq$ 4.8 s). We focused on analyzing the row 344. We present the plot analysis for the images we studied.
Figure 5.17 depicts the plot of the row 344 in blue, while the orange lines represent a smoothed signal to observe better the pixel value trend. An observable decreasing effect is present around column 400, where a detector anomaly is located.
By analyzing the trend, we observed that for short IT, the shadow's value is approximately 50/100 DN lower than the other neighboring pixels, corresponding to a percentage difference of about 1.5%. As the IT increases, the intensity of the detector anomaly decreases. At IT = 9.6 s, the shadow reaches approximately 400

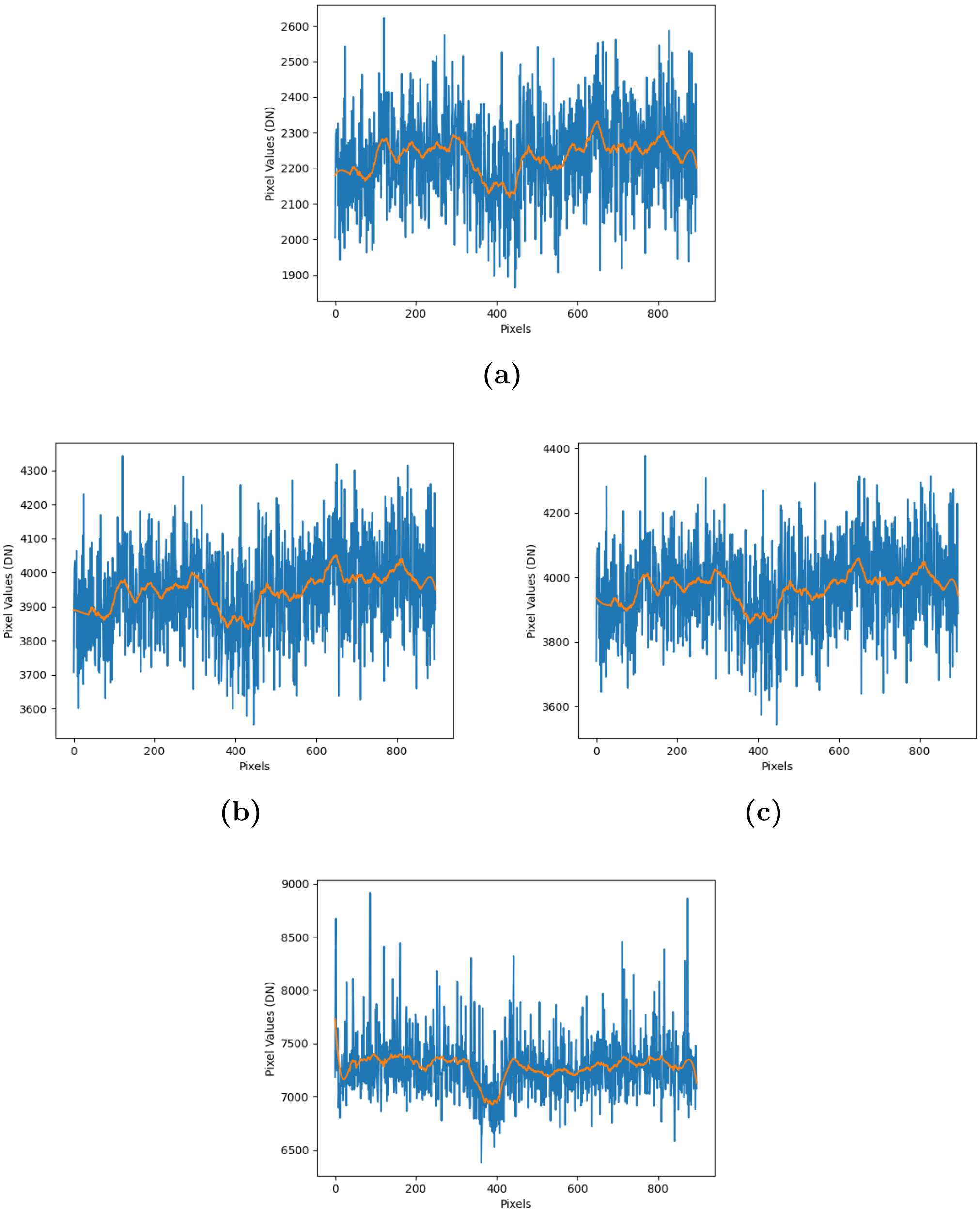

(a)

(b) **(c)**

(d)

Figure 5.17: Plot of the row 344 of the acquired at 400 ns (a), 3.32 ms (b), 0.15 s (c) and 9.6 s image (d) of the first session of the ICO 1.

DN less than the surrounding pixels, resulting in a percentage difference of around 3%. Consequently, the detector anomaly creates a ”shadow” effect in the images, similar to that shown in Figure 5.16.

In conclusion, the anomalies detected for PanL and PanH are not correlated, both spatially and over time. Furthermore, they do not correlate with the anomaly found on-ground and reported in [3].

These identified anomalies will be carefully considered when the acquisition of stars starts, ensuring that the stars' paths avoid these specific regions. However, intentional imaging could be performed in these regions to gain insights into how the detector responds locally.

Summarizing, the results presented in this chapter are of significant importance for in-flight activities and have implications for determining the future acquisitions of both instruments. Despite the remaining work that lies ahead, these findings provide crucial insight into the behavior and performance of the instruments.

Rebuilding the vignetting image from the stars, for Metis, and understanding the anomalies encountered during the analysis, for STC, is paramount for ensuring the accuracy and reliability of data collected during the missions. We can optimize the performance of the instruments and enhance the quality of the data.

References

[1] F. Frassetto, S. Fineschi, and L. Poletto. *Influence on the visible detector of the light scattered by the external shield*. Other. CNR.

[2] A. Liberatore et al. “In-flight calibration of Metis coronagraph on board of Solar Orbiter”. In: *International Conference on Space Optics — ICSO 2020*. June 11, 2021, p. 151. DOI: `10.1117/12.2599646`.

[3] F. Manfredi. *Analisi delle prestazioni del sensore di STC, stereo camera progettata in ambito della missione BepiColombo*.

6
Conclusion

This chapter summarizes and reviews the main scientific results of both research projects, presents the updated status of the mission, and traces the next steps of the author's work.
The dissertation began with an introductory section that outlines the scope and objectives of the Solar Orbiter and BepiColombo missions. More specifically, it provided an overview of the working environment for Metis, the coronagraph on board Solar Orbiter, and STC, the stereo camera on board BepiColombo.

The second chapter delved into the design of both instruments, which operate in an extremely harsh and challenging environment, and therefore have been designed in an innovative manner. It is valuable to understand how these instruments have been built and it is precious to understand how they have been calibrated, and, as well, know which are their optical performance.

In the third chapter, we investigated the significance of calibration and its properties and detailed it separately for Metis and STC. For Metis, we focused on the on-ground calibration setup, presented the results obtained for the vignetting function, and the study of the Point Spread Function (PSF).
For STC, we explored an anomaly in the behavior of the detector. This investigation shed light on the peculiarities and behavior of the detector during the mission. We then presented the elements required to perform simulations: the choice of the SIMBAD catalogue; the definition of right ascension and declination for displaying our results; and the importance of SPICE kernels and their application to our research objectives. We also established, based on previous work in the team, the magnitudes of stars used in our programs.

In Chapter 4, we conducted simulations using these elements to observe the stars in the sky and explored their significance for both instruments. One of the most crucial findings from these simulations was to determine at any desired epoch the number of stars visible by Metis and STC.

Furthermore, we associated these simulations with the on-ground and in-flight data, leading to the presentation of the Point Spread Function (PSF) in-flight calibration results. These results were obtained from images of stars passing in the Field of View (FoV) of Metis during the comet Leonard's passage. Notably, we observed that two stars appeared defocused in some regions of the detector. To understand the reasons behind this behavior, we conducted additional simulations using Zemax, which validated the fact that those two stars experimentally appeared defocused.

Additionally, we addressed the challenges associated with stellar in-flight calibration and emphasized the crucial role of stars as calibration light sources during the mission. To achieve accurate results, we stressed the importance of comparing on-ground and in-flight calibration data, ensuring a robust calibration process that aligns with the mission's scientific objectives. This comprehensive approach improved the reliability and precision of the data obtained from both instruments, with the aim of maximizing the scientific value of the mission.

Chapter 5 focused on the study of flat field (Metis) and dark (STC) for both instruments separately.

For Metis, the study consisted firstly in facing the failure of the foreseen calibration sources (LED lights), investigating an alternative, i.e. the sunlight reflected by the door in front of the aperture. Although we concluded that the retro-reflection of the door could not serve as a substitute for a homogeneous illumination light source, we confirmed that the signal intensity is proportional to the expected signal change with the instrument distance from the Sun, adhering to the $1/\mathrm{r}^2$ law for door illumination. The image acquired with the retro-reflection of the door provided insights into the potential degradation of optical elements and allowed us to perform ray tracing simulations to predict the impact on door images.

Besides, the study of the passage of the star theta Ophiuchi in the FoV of Metis had a dual purpose. Firstly, it helped assess the evolution of the vignetting function during the lifetime of the in-flight mission. Secondly, it evaluated the potential use of this passage as a detector for identifying any degradation of optical elements. We compared the results obtained on-ground with the in-flight and simulated vignetting functions, and the acquired star intensity showed good agreement, as expected for a recent mission (2 years).

For STC, we focused on analyzing dark images acquired for various ICO: 1, 2, 3, 4, and 7. Examination of the distribution of bad pixels led to the construction of a look-up table matrix. Such lookup tables enabled us to extrapolate the behavior of each filter, including both broadband and panchromatic filters. The analysis revealed that the images acquired at the first integration time showed a different number of bad pixels compared to subsequent acquisitions. The number of bad pixels remained constant or decreased until it reached a minimum for an integration time of 0.27 seconds. Beyond this point, thermal noise became more prominent, especially for integration times that exceeding 4.8 seconds.

During the analysis, we made intriguing observations regarding peculiar patterns in the Pan L and Pan H filters, such as a ”scratch” and some ”volcanoes”. These features exhibited different evolutions in shape and appearance across various integration times, prompting further research to understand their origin and potential persistence. We emphasized the importance of comparing these results with on-ground data and studying the behavior using flat field images to gain additional insights.

Furthermore, we identified bad pixels with values over 12000 DN using the look-up table method, finding them only in the panchromatic filter, corresponding to the ”scratch” and large ”volcanoes”. Finally, we highlighted the presence of a shadow near the ”scratch”, visible in all images acquired at different Integration Times.

Our work performed on in-flight calibration is then interesting for comprehending the behavior of the instruments, recognizing potential obstacles, and ensuring the optimal functionality of both Metis and STC throughout their respective missions, and is useful for missions operating in the challenging vicinity of the Sun in general. On the basis of what has been presented, there are also ongoing tasks for Metis and STC. For Metis, we can consider the continuous study of the stars, improving the vignetting image reconstruction, and the investigation of the Point Spread Function (PSF) of stars on a yearly basis. Indeed, it has been recently (and internally) observed that other instruments onboard the Solar Orbiter have already experienced a 10% decrease in performance [1].

Continuing to acquire dark images with STC allows us to monitor the detector performance over time and assess whether the identified anomalies persist. In fact, one potential solution to address these anomalies involves exploring post-acquisition processing techniques, such as masking defective pixel areas or applying a rolling mean approach to assign values to each pixel, provided the behavior remains constant over time.

In the realm of future Metis research, an essential work consists of estimating the intensity of the light detected from any star that crosses any instrument field of view. This task is the first being explored and is under development at this time, by taking into account not only stellar information, but also instrumental features. Another compelling prospect is the refinement of the study of the $1/r^2$ trend of retroreflected light, with increasing data collected each year, and within the broader context of advancing to next-generation instruments. The insights gleaned from this study could play a pivotal role in choosing optical elements for future missions venturing in proximity to the Sun.

As far as STC is concerned, future work involves comparing its results with those of other instruments. Specifically, examining parallelism with the CaSSIS (Colour and Stereo Surface Imaging System) camera on Mars, which shares the same detector as STC, and has been the topic of recent calibration publications. Additionally, drawing comparisons with instruments that employ similar imaging approaches, such as LROC (Lunar Reconnaissance Orbiter Camera, on board of the Lunar Reconnaissance Orbiter) and THEMIS camera (Thermal Emission Imaging System, on board of the Mars Odyssey orbiter), could provide valuable insights to enhance our understanding of detector behavior and calibration methodologies.

References

[1] *Solar Orbiter Science Working groups*. URL: https://drive.google.com/drive/folders/1qdlDWOVMjB77T_jQ4twcNL5Xpfv6Ymkr.

Chiara Casini Publication List

[1] C. Casini et al. “Simulations for in-flight stellar calibration aimed at monitoring space instruments optical performance”. Submitted AIDAA. 2024.

[2] Y. De Leo et al. “In-flight radiometric calibration of the Metis UV H I Ly-α channel and comparison with UVCS.” In preparation. 2024.

[3] C. Casini et al. *Stars Calibration*. Tech. rep. IFN-CNR, 2023.

[4] C. Casini et al. *STC bad pixels analysis: instrument check-out 1 images*. Tech. rep. IFN-CNR, 2023.

[5] C. Casini et al. “Theoretical, on-ground, and in-flight study of the Metis coronagraph vignetting”. In: *International Conference on Space Optics — ICSO 2022*. 2023, p. 4. DOI: 10.1117/12.2688589.

[6] V. Da Deppo et al. “Out-of-focus point sources image simulation for the Metis solar coronagraph onboard the Solar Orbiter mission”. In: *International Conference on Space Optics — ICSO 2022*. 2023, p. 220. DOI: 10.1117/12.2691114.

[7] Y. De Leo et al. “In-flight radiometric calibration of the Metis Visible Light channel using stars and comparison with STEREO-A/COR2 data”. In: *Astronomy & Astrophysics* 676 (2023), A45. DOI: 10.1051/0004-6361/202345979.

[8] F. Landini et al. “In flight stray light estimate for the Solar Orbiter/Metis coronagraph”. In: *International Conference on Space Optics — ICSO 2022*. 2023, p. 3. DOI: 10.1117/12.2688578.

[9] D. Telloni et al. “Coronal Heating Rate in the Slow Solar Wind”. In: *The Astrophysical Journal Letters* (2023). DOI: 10.3847/2041-8213/ace112.

[10] C. Casini et al. “In-flight Metis radiometric performance verification using the light retro-reflected from its door”. In: *Space Telescopes and Instrumentation 2022: Optical, Infrared, and Millimeter Wave*. 2022, p. 170. DOI: 10.1117/12.2631515.

[11] E. Martellato et al. *NASA MESSENGER mission: a tool to study Mercury beyond its operative life*. other. oral, 2022. DOI: 10.5194/epsc2022-1261.

[12] D. Telloni. “Linking Small-scale Solar Wind Properties with Large-scale Coronal Source Regions through Joint Parker Solar Probe–Metis/Solar Orbiter Observations”. In: *The Astrophysical Journal* (2022). DOI: 10.3847/1538-4357/ac8103.

[13] D. Telloni et al. "Observation of a Magnetic Switchback in the Solar Corona". In: *The Astrophysical Journal Letters* (2022). DOI: 10.3847/2041-8213/ac8104.

[14] V. Andretta et al. "The first coronal mass ejection observed in both visible-light and UV H I Ly- channels of the Metis coronagraph on board Solar Orbiter". In: *Astronomy & Astrophysics* 656 (2021), p. L14. DOI: 10.1051/0004-6361/202142407.

[15] C. Casini et al. "The use of the flat field panel for the on ground calibration of Metis coronagraph on board of Solar Orbiter". In: 15 (2021). URL: https://publications.waset.org/10011895/the-use-of-the-flat-field-panel-for-the-on-ground-calibration-of-metis-coronagraph-on-board-of-solar-orbiter.

[16] C. Casini et al. "On-ground flat-field calibration of the Metis coronagraph onboard the Solar Orbiter ESA mission". In: *International Conference on Space Optics — ICSO 2020*. 2021, p. 190. DOI: 10.1117/12.2599945.

[17] V. Da Deppo et al. "In-flight optical performance assessment for the Metis solar coronagraph". In: *International Conference on Space Optics — ICSO 2020*. 2021, p. 36. DOI: 10.1117/12.2599220.

[18] D. Telloni et al. "Exploring the Solar Wind from Its Source on the Corona into the Inner Heliosphere during the First Solar Orbiter–Parker Solar Probe Quadrature". In: *The Astrophysical Journal Letters* (2021). DOI: 10.3847/2041-8213/ac282f.

[19] P. Zuppella et al. "Optical Coatings: Applications and Metrology". In: *The 2nd International Electronic Conference on Applied Sciences*. 2021, p. 50. DOI: 10.3390/ASEC2021-11137.

[20] A. Volpicelli et al. "The MDOR/PDOR on-line module for MISO, the planning software of Solar Orbiter instruments". In: *Software and Cyberinfrastructure for Astronomy VI*. 2020, p. 29. DOI: 10.1117/12.2562514.

[21] V. Da Deppo et al. "Alignment procedure for the Gregorian telescope of the Metis coronagraph for the Solar Orbiter ESA mission". In: *International Conference on Space Optics — ICSO 2018*. 2019, p. 257. DOI: 10.1117/12.2536177.

[22] Y. De Leo et al. "F-corona model adapted to Solar Orbiter orbit". In: (2019). URL: https://www.researchgate.net/publication/375662129_F-corona_model_adapted_to_Solar_Orbiter_orbit.

[23] F. Landini et al. "Stray light calibration for the Solar Orbiter/Metis solar coronagraph". In: *International Conference on Space Optics — ICSO 2018*. July 12, 2019, p. 89. DOI: 10.1117/12.2536009.

[24] *Updates on the PeNCIL project*. Il Nuovo Cimento C, 2019. DOI: `10.1393/ncc/i2019-19025-x`.

[25] C. Casini. *Calibrazione del coronografo spaziale Metis della missione Solar Orbiter*. 2018. URL: `https://www.researchgate.net/publication/328998046_Calibration_of_the_spatial_coronagraph_Metis_on_board_Solar_Orbiter`.

Acknowledgments

I express my gratitude to Dr. Paola Zuppella and Dr. Vania Da Deppo for their invaluable guidance and unwavering support: for always trusting me and making me improve during this journey.

Thanks to all my colleagues, in particular: Lorenzo for giving me the light on-ground and ~~in-flight~~ under water; Paolo for the constant support; Riccardo, Fabio and Daniele for their practicality and sense of humor; Fabio and Gabriele for being sources of knowledge; Carmen for her positivity. But most importantly, for the beers we shared, and I look forward to many more years of such treasured moments together.

I also want to thank Federico for his heart of gold.

Thanks also to my friends: your presence, encouragement and understanding have been a constant source of comfort and motivation, making this journey even more enjoyable and meaningful. I am beyond grateful for your friendship. I extend my special gratitude to Lara and Massimiliano for their encouragement throughout my bachelor, master and PhD cursus.

Last but not least, I also express my thanks to my family for everything they have done. I am deeply and passionately grateful to my wonderful husband, whose boundless love, unwavering encouragement and support, have been the pillars of strength that carried me through this journey.

The activities has been carried out within the framework of the ASI-INAF Contracts Agreement N. 2018-30-HH.0 and 2017-47-H.0.

This document was typeset in the EB Garamond typeface with $\LaTeX\,2_\varepsilon$, using a modified version of the Dissertate document syle[1]. Most figures were created with the Python graphing package Matplotlib [2], IDL, the open source graphic software Inkscape[3] and GIMP[4].

---

[1] https://github.com/suchow/Dissertate

[2] 10.1109/MCSE.2007.55

[3] Inkscape: Open Source Scalable Vector Graphics Editor, https://inkscape.org/

[4] GNU Image Manipulation Program, https://www.gimp.org/